Fabrication, Structure and Properties of a Single Carbon Nanotube-Based Nano-Electromechanical System

Letian Lin

A dissertation submitted to the faculty of the University of North Carolina at Chapel Hill in partial fulfillment of the requirements for the degree of Doctor of Philosophy in the Curriculum of Applied Sciences and Engineering.

Chapel Hill
2011

Approved by
Lu-Chang Qin
Sean Washburn
Michael R. Falvo
Jie Liu
Jian Ping Lu
Scott Paulson

ABSTRACT

Letian Lin: Fabrication, Structure and Properties of a Single Carbon Nanotube-Based Nano-Electromechanical System

(Under the direction of Dr. Lu-Chang Qin and Dr. Sean Washburn)

The research work evolved in this dissertation presents (i) a foundational study on the atomic structure, transport property, electromechanical actuation, and inter-shell friction of carbon nanotubes using a nano-electromechanical system based on a single carbon nanotube and (ii) a fabrication technique of the nano-electromechanical system which provides a versatile platform for studies on one-dimensional nano-materials such as nanowires or other types of nanotubes. The geometry of having a free suspended carbon nanotube makes the device capable of *in situ* electromechanical manipulation and electrical resistance measurement on a single nanotube in a transmission electron microscope.

The fabrication and the operation of the device are first described in detail. Experimental results are then presented to report the electrical and mechanical properties of single nanotubes and corresponding device characterization. First, chiral indices of a nanotube and its corresponding electrical resistance at room temperature are measured. A physical model based on the band gap theory is established to correlate the electrical resistivity with the atomic structure of the carbon nanotube. Second, I present a direct

measurement of the torsional motion of both shells of a double wall carbon nanotube under an external torque on the outer shell. The measurement is performed by actuating a metal paddle attached to the outer shell of the nanotube while the stains of the nanotube are derived from its electron diffraction patterns. The inner shell is found to twist along with the outer shell with no stiction. The inter-shell friction, both static and kinetic, is inferred from direct measurements of each shell's deformation, van der Waals interactions between the two shells, and a tested model of lattice strain. Finally, the handedness of carbon nanotubes is determined using the same device. The implications are also discussed for potential applications and as directions of future research.

ACKNOWLEDGEMENTS

The contents of this dissertation do not represent the effort of the author alone, but the contributions and the work from many people who have helped me a lot on this challenging research work. I owe a debt of gratitude to them for my final survival in the five years of PhD study.

First, I would like to express my deepest gratitude to my principal advisor, Prof. Lu-Chang Qin who led me into the world of transmission electron microscopy and carbon nanotubes. As my advisor, Dr. Qin not only taught me the scientific knowledge for my PhD research, but also instilled my intense interests in exploring the unknown world in physics and materials science. More importantly, he is a good listener and advisor when I felt disappointed, lost confidence and suffered from the frustrations in research and life.

Second, I would like to express my appreciation to my co-advisor, Prof. Sean Washburn who gaves me a lot of useful ideas and suggestions on my research study. Your mentorship is the one I had not been experienced and expected before: sink or swim. I hope I swam.

Third, I want to thank all my colleagues including Dr. Qi Zhang, Dr. Hakan Deniz, Dr. David Bordelon, Dr. Liang He, Dr. Kwan Skinner, Lamar Mair and Dimitry Spivak, Taoran Cui and Zheng Ren. I would like to express my special thanks to Dr. Hakan Deniz

who have taught me how to use the electron microscope efficiently and Dr. Qi Zhang who always patiently answers me all kinds of tedious questions about electron microscopies. I also owe a debt of gratitude to Dr. David Bordelon for showing me how to do silicon wet etching and dry etching and to Dr. Liang He for spending a large amount of time on solving vacuum leakage problems for me. My skills on photolithography and electron beam lithography are attributed to the guidance from Dr. Kwan Skinner, Lamar Mair and Dimitry Spivak. Taoran Cui and Zheng Ren as my labmates, we spent so many days and nights together doing experiments in the lab. You have felt and shared all my happiness and upset in the past five years. To you guys, my appreciation is beyond any word.

Fourth, I would like to thank the following research groups for all kinds of support on my research. To Dr. Jie Liu's group of Duke University and Dr. Scott Paulson's group of James Mason University, thank you for the advice and guidance on carbon nanotube synthesis. To Dr. Otto Zhou's group of UNC-CH, thank you for the generosity to let me use your RIE system. To CHANL in UNC-CH, thank you for your guidance on the FIB system and the PECVD system.

To Dr. Guang Yang and Dr. Zhongqiao Ren, who treat me like their brother, I am eternally grateful. Without you, I would lose a lot of happiness in my life in Chapel Hill.

Finally, to my Mom and Dad, I owe you everything. Thank you for all the endeavor to raise me. Your unerring support and confidence in me are more than what I deserve sometimes. I wish I could have explored the world while staying closer to you. I love you all.

TABLE OF CONTENTS

LIST OF ABBREVIATIONS

AFM	atomic force microscope
BHF	buffered hydrofluoric acid
CPD	critical point drying
CNT	carbon nanotube
CVD	chemical vapor deposition
EBL	electron beam lithography
FE	finite element
FIB	focus ion beam
MEMS	microelectromechanical systems
MWNT	multiwall carbon nanotube
NBD	nano-beam electron diffraction
NEMS	nanoelectromechanical systems
OAS	optical absorption spectroscopy
PMMA	polymethyl methacrylate
RBS	radial breath mode
RIE	reactive ion etching
RRS	resonant Raman spectroscopy
SEM	scanning electron microscope
SPS	scanning tunneling spectroscopy
STM	scanning tunneling microscope
SWNT	single wall carbon nanotube
TEM	transmission electron microscope

Chapter 1

Introduction

1.1 Motivation

Computer science and technology have experienced tremendous development in the past 65 years since the construction of the first computer. Without question, the integration and the miniaturization of electronic devices are one of the most basic and core achievements on computer development. It greatly affects the size, weight, power consumption, storage volume and computation power. The first decimal arithmetic computer based on vacuum tube, ENIAC, was built in 1945. It had a weight of 30,000 kg, a volume of 84 cubic meters, power consumption of 140 kilowatts and computation power of 5000 times per second. On the contrary, today's laptop only has a weight of a couple of pounds, a volume less than 0.005 cubic meters, a power consumption less than 100 watts and a computation power of 2.4 billion times per second. The realization of this miniaturization is based on the advent of ultra large scale integrated circuit technology and the silicon technology. By using micron- and sub-micron lithography, electronic devices such as diodes and transistors are fabricated within an area of 0.03

square microns or even smaller on a silicon chip. For example, an Intel microprocessor chip has about 200 million devices per square centimeters.

But, we are also coming to the limit of today's silicon technology after achieving fast progress on computer chips. The size of a device is limited by the following factors: (i) the wavelength of photons and refraction index in the immersion photolithography; (ii) the depletion of silicon, *i.e.* suppression of the free charge carrier concentration; (iii) the oxide thickness. Power consumption is another concern. Although the power consumption for any single device is small, the total amount goes up quickly when that is multiplied over an extremely large number. Furthermore, heating of electronic devices is a big problem. In the high ambient temperature ranges, devices often fail to work properly. All these factors will negatively affect the miniaturization of computer technology.

In order to push the limit to a smaller dimension, people are seeking new materials with smaller size, less defective structure, lower power consumption and larger surface to volume ratio to dissipate heat. This comes to the length scale that is being studied by the present nanotechnology. Nano-materials, the dimension on the order of nanometers, are usually composed of one to tens of molecular layers in one dimension. On this level, the quantum effects are less masked by bulk effects and materials start to show different properties. Carbon nanotubes with diameters on order of nanometers and lengths from nanometers to millimeters, show unique electrically properties, which make them potential material for future computer technology. The subject of this thesis is fabrication of nanometer-scale electromechanical devices based on a suspended carbon

nanotube and exploration of the mechanical and electrical transport properties of the nanotubes.

1.2 Structure of Carbon Nanotubes

Carbon nanotubes have attracted tremendous amount of research interests from fundamental science and technological perspectives since they were first discovered by Iijima in 1991[1-3]. Due to their low dimensionality, carbon nanotubes possess a variety of intriguing properties which make them promising candidates for future technological applications [4-9]. They have already been used to build prototypes of next generation technology, including nano-transistors, metallic wires, electromechanical devices and displays [10-14]. People have suggested their use in everything from nano-electrical devices to space elevators. Although these promising applications of carbon nanotubes may be somehow overestimated, the motivation and effort for the research on carbon nanotubes' wide spread applications are worthwhile.

To understand the atomic structure of a CNT, one can start from the structure of a graphene lattice [7], where the basis vectors $\vec{a}_1$ and $\vec{a}_2$ ($\vec{a}_1 = \vec{a}_2 = 0.246$ nm) are separated with an angle of 60^0, as shown in Fig. 1.2a. A single wall carbon nanotube can be obtained by rolling up a graphene about an axis perpendicular to the chiral vector $\vec{A}$ to make the seamless hollow cylinder, illustrated in Fig. 1.2b. The chiral vector is defined by:

$$\vec{A} = u\vec{a}_1 + v\vec{a}_2,\tag{1.2.1}$$

where u and v are integers and are called chiral indices. The perimeter of a CNT is the magnitude of the chiral vector $A = a_0(u^2 + v^2 + uv)^{1/2}$, and the diameter of the nanotube is $R_d = A/2\pi$. The translational vector $\vec{c}$ of the nanotube perpendicular to the chiral vector is defined as:

$$\vec{c} = m\vec{a_1} + n\vec{a_2} ,$$ (1.2.2)

where m and n are integers. By applying the orthogonality relationship between the chiral and translational vectors ($\vec{A} \cdot \vec{c} = 0$), m and n can be calculated as

$$m = -\frac{u + 2v}{M}, n = \frac{2u + v}{M},$$ (1.2.3)

where M is the greatest common divisor of $(2u+v)$ and $(u+2v)$. Thus the periodicity of the nanotube is given in the form of:

$$|\vec{c}| = \frac{\sqrt{3}a_0\sqrt{u^2 + v^2 + uv}}{M} = \frac{\sqrt{3}A}{M} .$$ (1.2.4)

The angle between the lattice vector $\vec{a_1}$ and chiral vector $\vec{A}$ is called helical angle (helical angle) and is given by

$$\alpha = \arctan\left(\frac{\sqrt{3}v}{v + 2u}\right).$$ (1.2.5)

The helical angle of a carbon nanotube lies in the range of [0°, 30°] if the handedness of the tube is ignored ($u \geq v \geq 0$). Within this range, carbon nanotubes come in two different groups of symmetry: non-helical and helical nanotubes. For helical nanotubes, the helical angle lies in the range of (0°, 30°). For the non-helical nanotubes, they are two

4

special cases. When $u > 0, v = 0$, *i.e.* $\alpha=0\,^\circ$, the nanotube is called zigzag. The other is called armchair nanotube when $u=v$, *i.e.* $\alpha=30\,^\circ$.

A multiwall carbon nanotube consists of multiple rolled-up graphene sheets. All the graphene sheets form concentric cylinders in a MWNT with an interlayer distance close to 0.34 nm. People can use the same parameters, *i.e.* chiral indices and helical angle, to describe the structure of each layer in a MWNT.

(a)

(b)
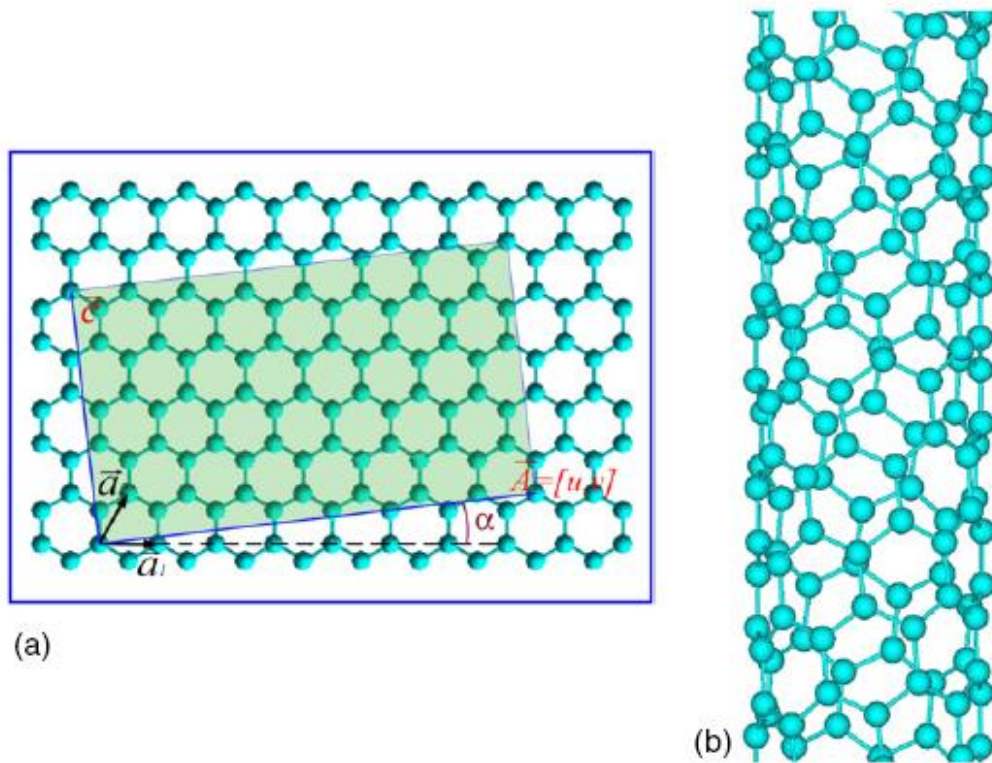
Figure 1.2 (a) Schematic of a graphene lattice structure with basis lattice vectors $\vec{a}_1$ and $\vec{a}_2$. The shadowed rectanglar area is the radial projection of a carbon nanotube (7, 1) on the graphene sheet. $\vec{A}$, α and $\vec{c}$ are the chiral vector, helical angle and translational vector of the nanotube. (b) Schematic structure of carbon nanotube (7, 1) when it is rolled up perpendicular to the chiral vector $\vec{A}$ to form a hollow cylinder. Adapted from [7].

1.3 Mechanical Properties of Carbon Nanotube

Carbon nanotubes are one of the strongest materials. This property is attributed to the sp^2 bonds shared by carbon atoms in the nanotube. Each atom is covalently bonded to the three nearest neighbors and this results in a robust structure. A SWNT is predicted to have a Young's modulus of ~1 TPa and a shear modulus of ~0.5 TPa by theory [5, 15]. The values of a MWNT may be different from each other, dependent on the number of layers, but theoretical work has suggested that a MWNT should have a Young's modulus above 1.1 TPa and a shear modulus above 0.55 TPa [5].

Many experimental work reports on the measurement of these values in the past decade [15-31]. Scanning tunnel microscope, atomic force microscopy, transmission electron microscopy and scanning electron microscopy have been extensively used in these experiments and the results are roughly same magnitude of the theoretical values. It remains a challenge in experiment to measure accurately the chiral indices *(u,v)* of a carbon nanotube and the mechanical properties of the same carbon nanotube. A technique to measure shear modulus and chiral structure of a free standing nanotube simultaneously will be described in Chapter 3 and the experimental results will be discussed in great detail in Chapter 5.

Furthermore, the weak van der Waals interactions between the neighboring layers in a MWNT make it easy to trigger a relative motion between different layers [32-39]. Experiments demonstrated that nanotubes exhibit little or no signs of wear or fatigue despite the large amount of the repetition of this motion due to the robustness of each carbon layer [10, 30, 40]. This unique property has stimulated a lot research work on

theoretical interlayer interaction models, experimental measurement on interlayer interaction and fabrication of carbon naotube based nano-electromechanical devices like nano-scale motors, springs or switches [14, 28, 30, 41-43]. Previous experimental work has been unable to directly measure the interlayer correlation in a MWNT under a torsional stress. In Chapter 5, direct measurements on the interlayer friction and inner-shell torsional response to the shear stresses applied to the outer-shell will be discussed in detail.

1.4 Electronic Properties of Carbon Nanotube

Because carbon nanotube is formed by rolling up a two-dimensional graphene sheet into a seamless cylinder, the electronic band structure of a CNT is closely related to that of a graphene sheet. Each carbon atom in a graphene structure has six electrons: two *1s* electrons, three *2sp²* electrons and one *2p* electron. The three *2sp²* electrons form three covalent bonds to bond the carbon atom to the 3 nearest neighbors in the graphene plane. The one *2p* electron forms an unsaturated π orbital which perpendicular to the graphene plane. Combining the tight-binding model and Bloch wave function, the energy dispersion relationship of a graphene sheet can be obtained in the following form [11]:

$$E = \pm V_{pp\pi} \sqrt{1 + 4\cos(\frac{\sqrt{3}}{2}k_ya)\cos(\frac{\sqrt{3}}{2}k_ya) + 4\cos^2(\frac{\sqrt{3}}{2}k_xa)} \ , \qquad (1.4.1)$$

where $V_{pp\pi}$ is tight binding parameter for π orbital (2.9 eV for graphene) and *a* is the lattice constant (*a*=0.246 nm). The covalent and conduction bands meet at six points $(\pm\frac{4\pi}{3\sqrt{3}a},0)$, $(\pm\frac{2\pi}{3\sqrt{3}a},\pm\frac{2\pi}{3a})$ at the corners of the first Brillouin zone. This energy band

structure has a non-zero density of states at the Fermi level, but the Fermi surface only

consists of points, as shown in Fig. 1.4.1. Thus, graphene is called a semi-metal.
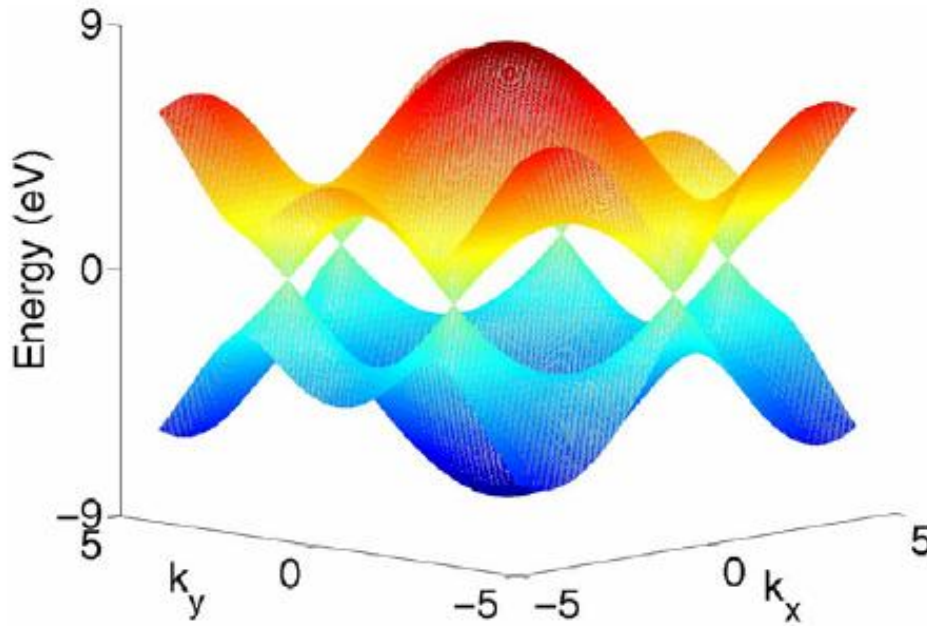
Figure 1.4.1 Electronic structure of graphene calculated basing on the tight-binding model with only π orbitals concerned. Adapted from [11].

When the graphene sheet is rolled up to form a CNT, this π orbital is still

perpendicular to the nanotube surface and forms a delocalized π network across the

nanotube, which is responsible for the nanotube electronic properties. But the wave

vector now is quantized in the circumferential direction [44]:

$$\vec{k} \cdot \vec{A} = k_x A_x + k_y A_y = 2\pi x \ , \tag{1.4.2}$$

where $\vec{k}$ is the waver vector, $\vec{A}$ is the chiral vector and x is an integer. As a result, CNT can be either metallic or semiconducting, depending on whether or not the allowed wave vectors by Eqn. 1.4.2 pass through any pair of the 6 graphene Fermi points, as illustrated in Fig. 1.4.2. Fig. 1.4.3 illustrates the examples of band structures for a semiconducting and a metallic zigzag CNTs. This leads to an equivalent condition for metallic CNT: $|u-v| = 3g$, g is an integer. The theoretical linear conductance of a metallic CNT in low bias transport is given by [11]

$$G = \frac{4e^2}{h} = \frac{1}{6.5 k\Omega},$$ (1.4.3)

when the condition $|u-v| = 3g$ is not satisfied, the CNT is semiconducting and the energy gap is given by [45]

$$E_g = (1 - \frac{0.4}{R_d^2}) \frac{V_{pp\pi}}{R_d} [1 + (-1)^p \gamma \frac{\cos(3\alpha)}{R_d}],$$ (1.4.4)

Where $V_{pp\pi}$ is the tight-binding parameter for the π orbital, R_d is the CNT radius divided by 0.142 nm, p is the reminder of $\dfrac{|u-v|}{3}$, α is the helical angle of CNT, and $\gamma = 0.4$ is a constant dependent on ratio of the tight-binding parameter π orbital to that of the σ orbital. As we can see from the Eqn. 1.4.4, the radius of CNT plays a dominant role in the energy gap when the radius is large. But the chiral structure of CNT starts to affect the energy gap if the nanotube radius is small and thus affects the electric resistance of the CNT. This subject will be discussed in great detail in Chapter 4.

9

Nanotubes are seldom in their perfect structures when measured in experiments. Interactions with metal contacts or substrate causes structural deformation and induce significant $\sigma - \pi$ coupling, stretching and compression of bonds, all of which affect CNT's electronic properties. Theoretically, the response of the change of band gap to a torsional stain is given in the following form [46]:

$$\frac{dE_g}{d\sigma} = sgn(2p+1)3tsin(\alpha) \; , \tag{1.4.5}$$

where σ is the strain and t is the tight-binding overlap integral 2.77 eV. Clearly in Eqn. 1.4.5, the response is sensitive to the chiral structure of nanotubes.
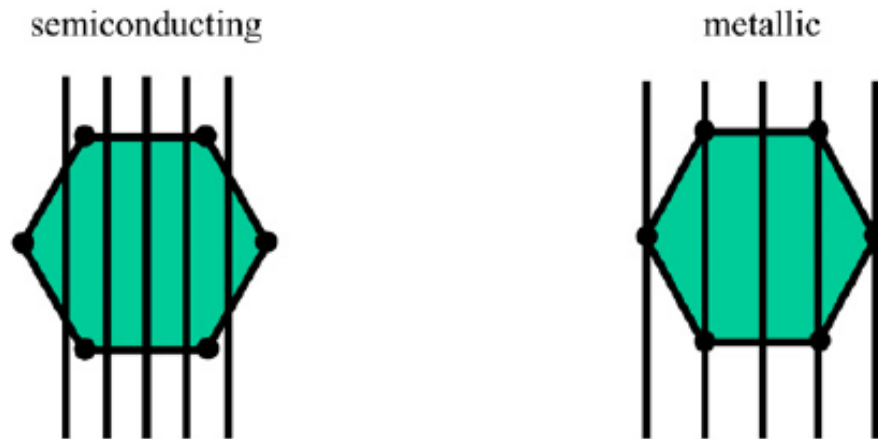
Figure 1.4.2 Illustration of allowed wave vector, shown as bold line, in a 2D Brillouin zone of graphene. Only when the wave vectors go through the vertices of the Brillouin zone, the CNT is metallic as shown in the right figure. Otherwise the CNT is semiconducting, shown in the left figure. Adapted from reference [11].
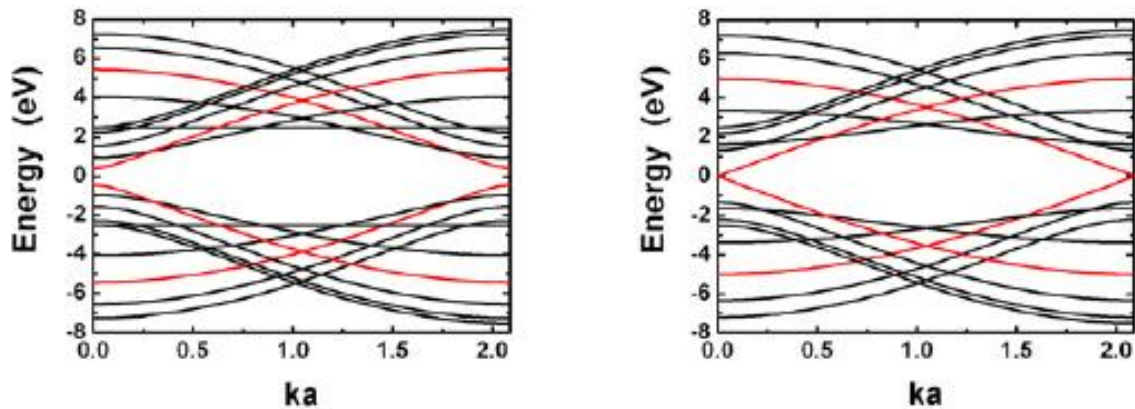
Figure. 1.4.3 Illustration of the band structure of a semiconducting (left) and metallic zigzag CNTs. Adapted from reference [11].

1.5 Outline

Chapter 2 of this thesis will concentrate on the techniques of CNT characterization. STM and Raman Spectroscopy will be introduced briefly. CNT imaging by transmission electron microscope and determination of CNT chiral structure by nano-beam electron diffraction patterns will be described in detail in this chapter. In Chapter 3, device fabrication techniques will be presented. The procedure of how to make suspended carbon nanotube nano-electromechanical devices will be the main topic. The design and fabrication of a customized TEM sample holder which is used for in situ TEM imaging and electronic measurement is described in the last section of this chapter. Chapter 4 discusses the resistance of SWNT and DWNT with known chiral indices. Chapter 5 focuses on the interlayer interactions of a DWNT under an external torsional stress. The use of a suspended CNT nanoelectro-mechanical device to apply an external strain on a DWNT as electron diffraction patterns being taken on the DWNT is demonstrated. Chapter 6 discusses how to reveal handedness of a CNT by analyzing the

shift of diffraction patterns under torsional strain. Finally, Chapter 7 summarizes the thesis and discusses future directions and other uses of the devices.

1.6 References

[1]   Iijima, S., Helical Microtubules of Graphitic Carbon. *Nature* **354**, 56-58 (1991).

[2]   Iijima, S. & Ichihashi, T., Single-Shell Carbon Nanotubes of 1-Nm Diameter. *Nature* **363**, 603-605 (1993).

[3]   Bethune, D. S., Kiang, C. H., Devries, M. S., Gorman, G., Savoy, R., Vazquez, J. & Beyers, R., Cobalt-Catalyzed Growth of Carbon Nanotubes with Single-Atomic-Layerwalls. *Nature* **363**, 605-607 (1993).

[4]   Kreupl, F., Graham, A. P., Duesberg, G. S., Steinhogl, W., Liebau, M., Unger, E. & Honlein, W., Carbon Nanotubes in Interconnect Applications. *Microelectron. Eng.* **64**, 399-408 (2002).

[5]   Lu, J. P., Elastic Properties of Carbon Nanotubes and Nanoropes. *Phys. Rev. Lett.* **79**, 1297-1300 (1997).

[6]   Lu, J. P., Elastic Properties of Single and Multilayered Nanotubes. *J. Phys. Chem. Solids* **58**, 1649-1652 (1997).

[7]   Qin, L.-C., Electron Diffraction from Carbon Nanotubes. *Rep. Prog. Phys.* **69**, 2761-2821 (2006).

[8]   Ngo, Q., Petranovic, D., Krishnan, S., Cassell, A. M., Ye, Q., Li, J., Meyyappan, M. & Yang, C. Y., Electron Transport through Metal-Multiwall Carbon Nanotube Interfaces. *IEEE Trans. Nanotechnol.* **3**, 311-317 (2004).

[9]   Wei, B. Q., Vajtai, R. & Ajayan, P. M., Reliability and Current Carrying Capacity of Carbon Nanotubes. *Appl. Phys. Lett.* **79**, 1172-1174 (2001).

[10]   Kis, A., Jensen, K., Aloni, S., Mickelson, W. & Zettl, A., Interlayer Forces and Ultralow Sliding Friction in Multiwalled Carbon Nanotubes. *Phys. Rev. Lett.* **97** (2006).

[11]   Anantram, M. P. & Leonard, F., Physics of Carbon Nanotube Electronic Devices. *Rep. Prog. Phys.* **69**, 507-561 (2006).

[12]   Heinze, S., Tersoff, J., Martel, R., Derycke, V., Appenzeller, J. & Avouris, P., Carbon Nanotubes as Schottky Barrier Transistors. *Phys. Rev. Lett.* **89** (2002).

[13]   Javey, A., Guo, J., Wang, Q., Lundstrom, M. & Dai, H. J., Ballistic Carbon Nanotube Field-Effect Transistors. *Nature* **424**, 654-657 (2003).

[14]   Fennimore, A. M., Yuzvinsky, T. D., Han, W. Q., Fuhrer, M. S., Cumings, J. & Zettl, A., Rotational Actuators Based on Carbon Nanotubes. *Nature* **424**, 408-410 (2003).

[15]   Treacy, M. M. J., Ebbesen, T. W. & Gibson, J. M., Exceptionally High Young's Modulus Observed for Individual Carbon Nanotubes. *Nature* **381**, 678-680 (1996).

[16]   Babic, B., Furer, J., Sahoo, S., Farhangfar, S. & Schonenberger, C., Intrinsic Thermal Vibrations of Suspended Doubly Clamped Single-Wall Carbon Nanotubes. *Nano Lett.* **3**, 1577-1580 (2003).

[17]   Gao, R. P., Wang, Z. L., Bai, Z. G., de Heer, W. A., Dai, L. M. & Gao, M., Nanomechanics of Individual Carbon Nanotubes from Pyrolytically Grown Arrays. *Phys. Rev. Lett.* **85**, 622-625 (2000).

[18]   Krishnan, A., Dujardin, E., Ebbesen, T. W., Yianilos, P. N. & Treacy, M. M. J., Young's Modulus of Single-Walled Nanotubes. *Phys. Rev. B* **58**, 14013-14019 (1998).

[19]   Poncharal, P., Wang, Z. L., Ugarte, D. & de Heer, W. A., Electrostatic Deflections and Electromechanical Resonances of Carbon Nanotubes. *Science* **283**, 1513-1516 (1999).

[20]   Wong, E. W., Sheehan, P. E. & Lieber, C. M., Nanobeam Mechanics: Elasticity, Strength, and Toughness of Nanorods and Nanotubes. *Science* **277**, 1971-1975 (1997).

[21]   Hall, A. R., An, L., Liu, J., Vicci, L., Falvo, M. R., Superfine, R. & Washburn, S., Experimental Measurement of Single-Wall Carbon Nanotube Torsional Properties. *Phys. Rev. Lett.* **96** (2006).

[22]   Falvo, M. R., Clary, G. J., Taylor, R. M., Chi, V., Brooks, F. P., Washburn, S. & Superfine, R., Bending and Buckling of Carbon Nanotubes under Large Strain. *Nature* **389**, 582-584 (1997).

[23]   Gupta, S., Dharamvir, K. & Jindal, V. K., Elastic Moduli of Single-Walled Carbon Nanotubes and Their Ropes. *Phys. Rev. B* **72** (2005).

[24]   Tombler, T. W., Zhou, C. W., Alexseyev, L., Kong, J., Dai, H. J., Lei, L., Jayanthi, C. S., Tang, M. J. & Wu, S. Y., Reversible Electromechanical Characteristics of Carbon Nanotubes under Local-Probe Manipulation. *Nature* **405**, 769-772 (2000).

[25]   Salvetat, J.-P., Briggs, G. A. D., Bonard, J.-M., Bacsa, R. R., Kulik, A. J., St, ouml, ckli, T., Burnham, N. A., Forr, oacute, L., aacute & szl, Elastic and Shear Moduli of Single-Walled Carbon Nanotube Ropes. *Phys. Rev. Lett.* **82**, 944 (1999).

[26]   Ono, Y. & Ogino, T., Observation of Suspended Carbon Nanotube Configurations Using an Atomic Force Microscopy Tip. *Jpn. J. Appl. Phys.* **48** (2009).

[27]   Volodin, A., Van Haesendonck, C., Tarkiainen, R., Ahlskog, M., Fonseca, A. & Nagy, J. B., Afm Detection of the Mechanical Resonances of Coiled Carbon Nanotubes. *Appl. Phys. A-Mater. Sci. Process.* **72**, S75-S78 (2001).

[28]   Papadakis, S. J., Hall, A. R., Williams, P. A., Vicci, L., Falvo, M. R., Superfine, R. & Washburn, S., Resonant Oscillators with Carbon-Nanotube Torsion Springs. *Phys. Rev. Lett.* **93** (2004).

[29]   Williams, P. A., Papadakis, S. J., Patel, A. M., Falvo, M. R., Washburn, S. & Superfine, R., Torsional Response and Stiffening of Individual Multiwalled Carbon Nanotubes. *Phys. Rev. Lett.* **89** (2002).

[30]   Meyer, J. C., Paillet, M. & Roth, S., Single-Molecule Torsional Pendulum. *Science* **309**, 1539-1541 (2005).

[31]   Demczyk, B. G., Wang, Y. M., Cumings, J., Hetman, M., Han, W., Zettl, A. & Ritchie, R. O., Direct Mechanical Measurement of the Tensile Strength and Elastic Modulus of Multiwalled Carbon Nanotubes. *Mater. Sci. Eng. A-Struct. Mater. Prop. Microstruct. Process.* **334**, 173-178 (2002).

[32]   Charlier, J. C. & Michenaud, J. P., Energetics of Multilayered Carbon Tubules. *Phys. Rev. Lett.* **70**, 1858-1861 (1993).

[33]   Kolmogorov, A. N. & Crespi, V. H., Smoothest Bearings: Interlayer Sliding in Multiwalled Carbon Nanotubes. *Phys. Rev. Lett.* **85**, 4727-4730 (2000).

[34]   Saito, Y., *Fullerenes: Recent Advances in the Chemistry and Physics of Fullerenes and Related Materials* (1994).

[35]   Zhao, Y., Ma, C. C., Chen, G. H. & Jiang, Q., Energy Dissipation Mechanisms in Carbon Nanotube Oscillators. *Phys. Rev. Lett.* **91** (2003).

[36]   Servantie, J. & Gaspard, P., Methods of Calculation of a Friction Coefficient: Application to Nanotubes. *Phys. Rev. Lett.* **91** (2003).

[37]   Legoas, S. B., Coluci, V. R., Braga, S. F., Coura, P. Z., Dantas, S. O. & Galvao, D. S., Molecular-Dynamics Simulations of Carbon Nanotubes as Gigahertz Oscillators. *Phys. Rev. Lett.* **90** (2003).

[38]   Yakobson, B. I., Brabec, C. J. & Bernholc, J., Nanomechanics of Carbon Tubes: Instabilities Beyond Linear Response. *Phys. Rev. Lett.* **76**, 2511-2514 (1996).

[39]   Guo, W. L., Zhong, W. Y., Dai, Y. T. & Li, S. A., Coupled Defect-Size Effects on Interlayer Friction in Multiwalled Carbon Nanotubes. *Phys. Rev. B* **72** (2005).

[40]   Cumings, J. & Zettl, A., Low-Friction Nanoscale Linear Bearing Realized from Multiwall Carbon Nanotubes. *Science* **289**, 602-604 (2000).

[41]   Bourlon, B., Glattli, D. C., Miko, C., Forro, L. & Bachtold, A., Carbon Nanotube Based Bearing for Rotational Motions. *Nano Lett.* **4**, 709-712 (2004).

[42]   Cohen-Karni, T., Segev, L., Srur-Lavi, O., Cohen, S. R. & Joselevich, E., Torsional Electromechanical Quantum Oscillations in Carbon Nanotubes. *Nat. Nanotechnol.* **1**, 36-41 (2006).

[43]   Craighead, H. G., Nanoelectromechanical Systems. *Science* **290**, 1532-1535 (2000).

[44]   Deniz, H., Electron Diffraction and Microscopy Study of Nanotubes and Nanowires. PhD Thesis, The University of North Carolina at Chapel Hill, (2007).

[45]   Yorikawa, H. & Muramatsu, S., Energy Gaps of Semiconducting Nanotubules. *Phys. Rev. B* **52**, 2723-2727 (1995).

[46]   Rochefort, A., Avouris, P., Lesage, F. & Salahub, D. R., Electrical and Mechanical Properties of Distorted Carbon Nanotubes. *Phys. Rev. B* **60**, 13824-13830 (1999).

Chapter 2

Characterization Techniques for Carbon Nanotubes

Identification of the atomic structures of carbon nanotube has been on the center stage of research ever since the nanotubes were discovered. Many techniques have been developed and applied to characterize CNT structure including transmission electron microscopy (TEM), scanning tunneling microscopy (STM), scanning electron microscopy (SEM), atomic force microscope (AFM), X-ray diffraction (XRD), Raman spectroscopy, optical absorption spectroscopy, and nuclear magnetic resonance (NMR). So far TEM has been the most popular and powerful technique for characterizing CNT structure although STM, Raman spectroscopy and optical absorption spectroscopy are also widely used for elucidation of the CNT atomic structure. Due to various limitations of their probing methods, the later three techniques still have formidable difficulties on obtaining accurate atomic structure compared to TEM.

2.1 Scanning Tunneling Microscopy (STM)

Scanning tunneling microscope is a non-optical surface imaging instrument with atomic precision invented in 1981. The invention won its inventors Gerd Binning and Heinrich Rohrer, the Nobel Prize in Physics in 1986. A STM can have a lateral resolution of 0.1 nm and a depth resolution of 0.01 nm. Within such a high resolution, the outermost atoms on surface can be routinely imaged.

The working principle and high resolution capability of STM are based on the concept of quantum tunneling. When the metal probe of a STM is brought very close to sample surface (usually about $4-7$ $\overset{\circ}{A}$) with a voltage bias applied between the probe tip and surface, electrons will tunnel through the vacuum between them and form a tunneling current. This current is a function of the separation distance between tip and surface, bias voltage, tip radius and local density of states of the surface. Morphological information is acquired through monitoring the tunneling current when the probe is scanning across the surface. The local density of states can be derived from the differential conductance calculated from tunneling current and bias voltage curve. The surface morphology thus can be reconstructed based on the local density of states.

Experiments [1-3] by STM and scanning tunneling spectroscopy (STS) have been reported on the characterization of SWNT's atomic structure as well as electronic structure. Fig. 2.1.1 shows a high resolution STM image of a SWNT, in which the lattice of black dots are attributed to the centers of the hexagons [1]. The dashed line and the solid line represent the tube axis and the zigzag direction, respectively. The angle between the two lines is the helical angle from which chiral indices (*u, v*) of the SWNT can be derived if the tube diameter is known. The diameter can be measured by

estimating the line profiles perpendicular to the tube axial direction. An accuracy of $\pm 1^\circ$ in helical angle and ± 0.1 nm in diameter measurement can be obtained and this allows for an identification of the chiral structure. Besides the atomic structure of a SWNT, the SWNT's band gap can also be derived from the conductance calculated from an I-V curve measured by STM.

STM is a very powerful characterization tool in the sense that the atomic structure and the electronic properties can be investigated simultaneously. But the structure deformation [4, 5] resulted from interactions between a SWNT and the substrate may induce errors in structure characterization by STM, especially when the diameter of a SWNT is larger than a couple of nanometers. Existing STM studies on MWNTs show that STM resolves the charity and the electronic properties of outer shell only. The effects of the inner shells on the electronic spectroscopy of MWNTs are very weak [6]. Therefore, STM technique is not able to detect the atomic structures of inner shells in MWNT. In 2007, Giusca *et. al.* demonstrates that the chirality of the inner shell in a DWNT can be obtained from the STS measurement combined with calculated local density of states [7]. However, the method to derive inner shell information works only in certain combinations of inner and outer shells and thus is not a universal method for all DWNTs.
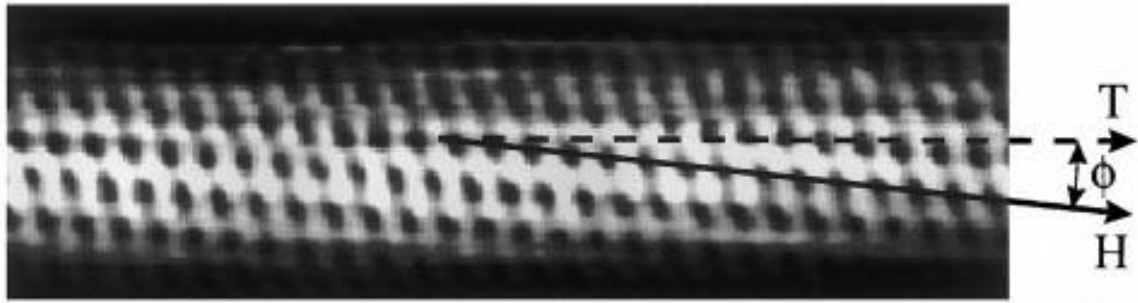
Figure 2.1.1 Atomically resolved STM image of an individual SWNT. T, H and Ø are the tube axis, zigzag direction and helical angle, respectively. The lattice of black dots represents the centers of the hexagons. Adapted from reference [1].

2.2 Raman Spectroscopy

Raman spectroscopy is a widely used technique for the study of vibrational, rotational, and other low frequency modes in materials. The basic principle of Raman spectroscopy is the concept of Raman scattering of monochromatic light which is usually comes from lasers in the visible, near infrared and near ultraviolet range. The interactions between photons of the laser and molecular vibrations, phonons or other excitation modes in the system will shift the laser photons' energy up and down. The information about phonon modes in the system can be obtained from this energy shift.

The diameter dependence of vibrational mode frequencies and the electronic structure of carbon nanotubes can be studied by Raman spectroscopy. Raman scattering occurs when the energy of incident laser photons matches one inter-band electronic transition energy of a carbon nanotube. A typical Raman spectrum of a SWNT has two sharp peaks corresponding to the radial breathing mode (RBM) and the graphitic mode (also called G-band), respectively [8]. The RBM mode, where all carbon atoms move in phase in radial direction, is a low frequency vibration mode and very sensitive to the

diameters of the nanotubes but not their helicities. The peaks are located between 120 cm^{-1} and 350 cm^{-1}, respectively. The frequency of RBM mode is usually used to determine the diameter of a SWNT and is given by

$$w_{RBM} = \frac{A}{d} + B \tag{2.2.1}$$

where d is tube diameter, A (unit: $cm^{-1}nm$) and B (unit: cm^{-1}) are constants and vary between individual SWNT and SWNT bundles. A and B have been found to be 248 $cm^{-1}nm$ and 0 cm^{-1} for isolated SWNTs on Si/SiO_2 substrate [9].

The diameter alone is not enough to identify the chirality of a SWNT. The second parameter needed is the transition energies of inter-bands which can be obtained from resonant Raman scattering (RRS). A plot of transition energies of all chiral structures calculated from tight-binding model should be compared with those obtained from RRS experiments. With the tube diameter, the chiral indices can be determined by a match between theoretical and measured transition energies [10].

As we can seen from Eqn. 2.2.1, Raman spectroscopy is a tool very sensitive to nanotube diameters (<2 nm). The RBM signals become very weak and are broadened for SWNT with large diameter and MWNTs. This is because that the curvature of CNT has less influences and the Raman spectra resemble to that of graphene when the diameter is large. However, the innermost shell of a MWNT still shows strong RBM modes in the spectra and the chiral indices of the shell can be determined by Raman spectroscopy because of its small inner diameter (< 2 nm) [11, 12].

2.3 Optical Absorption Spectroscopy

Optical absorption spectroscopy refers to the technique which measures the absorption spectrum of a material when the material is exposed to light (usually the light source covers a broad swath of wavelengths from infrared to ultraviolet). If the incident wavelength matches certain transition energy, the photon will be absorbed and the material will transit to an excited state. Emission occurs a photon with energy equal to the energy difference between the ground state and excited state. Therefore, the absorption spectrum of a material can be calculated from its emission spectrum using appropriate theoretical models and additional information about the quantum mechanical states of the substance. The inter-band transition energies and electronic structure of SWNTs can be studied by optical absorption spectroscopy based on the principle mentioned above. In an optical absorption spectroscopy measurement, SWNTs are usually well dispersed in a solution and show high energy-resolution in their optical absorption spectrum. The method to indentify the chiral indices of SWNTs is similar to that of Raman spectroscopy mentioned in last section [13-16].

The disadvantage of optical absorption spectroscopy is that it is hard to characterize the structure of a MWNT. It is also difficult to identify the structure of a single SWNT because of the weak signal.

2.4 Transmission Electron Microscopy and Electron Diffraction

Transmission electron microscopy is a powerful tool for microstructure and nanostructure characterization. It is a microscopy where fast electrons go through a very thin specimen, interacting with the atoms in the specimen as electrons pass through.

Scattered electrons are focused to form a magnified image onto an imaging device such as a fluorescent screen, a photographic film, or a sensor such as a CCD camera. The physical principles behind the development of TEM should be attributed to the following two aspects: (1) the wave-like characteristics of electrons first postulated by Louis de Broglie in 1925 [17]; (2) the discovery of electron focusing lenses which use electromagnetic field to focus moving electrons in desired direction by Hans Busch in 1926 [18]. The first transmission electron microscope was built by Ernst Ruska and Max Knoll in 1932 [19]. Ernst Ruska shared the Nobel Prize in Physics with Gerald Binning and Hans Rohrer in 1986. The wavelength of an electron accelerated by a voltage between 100 kV to 400 kV is about two orders magnitude smaller than the size of an atom which has a diameter of about 0.1 nm. In principle, it is possible to resolve material structure well below the atomic level according to the Raylaigh criteria [20]. However, a TEM with this resolution limit is impossible to construct due to the imperfections of the magnetic lenses. Nowadays, a good TEM can achieve the resolution on the order of 0.1 nm. In contrast, electron diffraction is much less sensitive to the imperfections of magnetic lenses, but more dependent on the convergence of incident electrons [21].

Within this research, CNT images and electron diffraction patterns are taken on JEM 2010F FasTEM electron microscope (vender JEOL). All the diffraction patterns are taken by the nanobeam electron diffraction method with beam waist of about 80 nm.

2.4.1 Theory of Electron Imaging in TEM

A TEM produces an image in the following two-step Abbe principle: (1) the incident electrons are scattered by the specimen and form a diffraction pattern on the back focal plane of the objective lens; (2) the scattered electrons are recombined to form

an image on the image plane. Two imaging mechanisms are usually used: amplitude contrast and phase contrast [22]. In the amplitude contrast mode, the image contrast is the result from the electrons scattered in different angles within a specimen. The areas of the specimen with higher mass or larger Coulomb potential will scatter more electrons toward large angular regions which are away from optical axis. If a small aperture is used, most electrons which are scattered in large angles can be excluded except the selected beam. As a result, the areas corresponding to the higher mass or strong atomic potential positions within the specimen will turn dark in the image. On the other hand, image contrast in the phase contrast mode comes from the phase difference of electrons caused by interactions between electrons and the Coulomb potential of the specimen. A large objective aperture is usually used to allow more scattered beams to pass through the objective lenses to form an image. It offers a much higher structural resolution and is usually called high resolution TEM compared to the amplitude contrast mode. But it requires that the specimen be thin.

Like the image formation in an optical microscope, the scattered electron waves in the diffraction plane will form a two-dimensional structure image projected from three-dimensional specimen on the image plane. However, in order to better interpret the electron imaging process, both non-linear imaging and dynamical electron diffraction effects need to be considered [23].

For phase contrast imaging, the interactions between the incident electrons and the specimen are usually weak and theories can be greatly simplified. In the phase-grating approximation, the wave function of the electron scattered by specimen can be described by [24]

$$\psi_o(x,y) = \exp\left[-i\beta V_p(x,y)\right],\tag{2.4.1}$$

where $\beta = \pi/(\lambda U)$ is the relativistic interaction constant with U being the accelerating voltage applied on electrons, $V_p(x,y)$ is the projected Coulomb potential of specimen in a plane perpendicular to the direction of the incident electron beam and λ is the wave length of the electrons. For a thin specimen constituted of light atoms, the weak phase object approximation can be applied and Eqn. 2.4.1 can be simplified to

$$\psi_o(x,y) \cong 1 - i\beta V(x,y),\tag{2.4.2}$$

where the unit 1 represents the transmitted wave which has no interaction with the specimen and the imaginary part corresponds to the scattered waves. The image wave on the image plane is a convolution between the object wave and a contrast transfer function $T(\vec{r})$:

$$\psi_i(\vec{r}) = \psi_o(\vec{r}) \otimes T(\vec{r}),\tag{2.4.3}$$

where $\otimes$ is the convolution operator. The convolution operation of two functions can be expressed as the product of their corresponding Fourier transforms in the reciprocal space:

$$\Psi_i(\vec{q}) = \Psi_o(\vec{q}) \cdot T(\vec{q}).\tag{2.4.4}$$

The contrast function in a TEM includes the information of aperture function, spherical aberration and imperfection of focusing of the objective lens and is given by [25]

$$T(\vec{q}) = a(\vec{q})\exp[2\pi i\chi(\vec{q})],\tag{2.4.5}$$

where $a(\vec{q})$ is the aperture function of the objective lens and

$$\chi(\vec{q}) = \frac{1}{4}C_s\lambda q^4 + \frac{1}{2}\Delta f q^2,\tag{2.4.6}$$

25

where C_s and Δf are the spherical aberration coefficient and defocus of the objective lens, respectively. Using Eqn. 2.4.5 and 2.4.6, Eqn. 2.4.3 can then be expressed as

$$\psi_i(x, y) = 1 + \beta V_p(x, y) \otimes Im[T(x, y)] - i\beta V_p(x, y) \otimes Im[T(x, y)]. \tag{2.4.7}$$

In weak phase object approximation, $\sigma V_p \ll 1$, the image intensity can then be further simplified into

$$I(x, y) = |\Psi_i(x, y)|^2 \cong 1 + 2\beta V_p(x, y) \otimes Im[T(x, y)]. \tag{2.4.8}$$

Eqn. 2.4.8 shows that only the imaginary part of the contrast transfer function contributes to the image intensity in the weak phase object approximation and linear imaging.

2.4.2 TEM Imaging of CNT

Because CNTs are formed by graphene layers and carbon atoms have a low atomic number ($N_A = 6$), the weak phase object approximation discussed in the last section can be used to interpret the TEM images of carbon nanotubes structure (an image actually corresponds to the projected Coulomb potential of the CNT [26]). A high resolution TEM equipped with a field emission electron gun can easily obtain structural images of a CNT with a resolution of about 0.2 nm. Thermal and mechanical vibrations, stage drift, and instabilities of the magnetic lenses will compromise the quality and the resolution of a TEM image.

Fig. 2.4.1 shows high resolution TEM images of a SWNT, a DWNT and a six-wall carbon nanotube. Hollow cylinder structure of the carbon nanotubes is seen clearly in the images. In the DWNT and the six-wall carbon nanotubes, two and six concentric cylinders can be identified in the figure. The two parallel darks lines run along the tube axis are the projected structure of the tube walls. The diameter of the nanotube can be

measured from a line profile perpendicular to the tube axis. But the measurement needs to be very careful because the position and width of the dark line are very sensitive to the imaging condition such as the defocus of the objective lens. It also causes errors in the diameter measurement if the nanotube is not oriented within a horizontal plane, *i.e.* not perpendicular to incident beam. The error becomes more significant when measuring the smaller diameter tube due to the pronounced curvature [27].
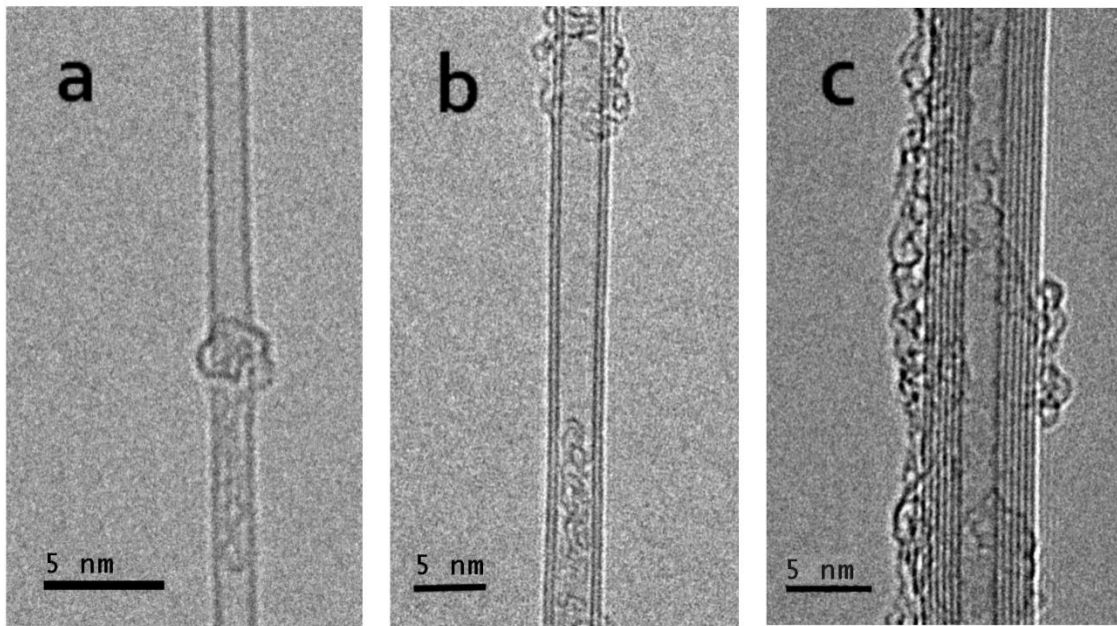
Figure 2.4.1 TEM images of (a) SWNT, (b) DWNT, and (c) 6-wall carbon nanotube taken with JEM 2010F operated at 80 kV.

2.5 Electron Diffraction Theory of Carbon Nanotube

The kinematical theory of electron diffraction is used to understand the diffraction patterns of carbon nanotubes because carbon atoms have a small scattering amplitude for fast incident electrons. A brief understanding of electron diffraction from CNT could start

from the diffraction pattern of graphene. Since carbon nanotubes are formed from graphene, they share some features in the diffraction patterns: diffraction layer lines resulting from the honeycomb lattice of graphite have a well-defined periodicity in the tube axial direction. But the structure in the radial direction is not periodic in a CNT when the graphene is rolled along the chiral vector to form a nanotube. As a result, the reflections are sharply defined along tube axis but elongated perpendicular to the tube axis.

A complete CNT electron diffraction theory was formulated by Qin in 1994 [28] and Lucas et al. in 1996 [29, 30] based on the kinematical theory of scattering from helical structure developed by Cochran, Crick and Vand in 1952 [31]. The theory has been proved to be powerful in characterization of carbon nanotube's chiral structure. The atomic scattering amplitude for electrons incident on atoms are described by the first Born approximation [30]

$$F(\vec{q}) = \frac{2\pi m e}{h^2} \int v(\vec{r}) \exp(2\pi i \vec{q} \cdot \vec{r}) d\vec{r} \,, \tag{2.5.1}$$

where $v(\vec{r})$ is the Coulomb potential of the scattering atom, e is the charge of an electron, m is the relativistic mass of electron, h is Plank's constant and $\vec{q}$ is the scattering vector with the magnitude defined as

$$q = \frac{2\sin(\Theta/2)}{\lambda}, \tag{2.5.2}$$

where Θ is the total scattering angle and λ is the wave length of the incident electron.

The diffraction intensity distribution $I(\vec{q})$ in reciprocal space is the square of the scattering amplitude

$$I(\vec{q}) = |F(\vec{q})|^2. \tag{2.5.3}$$

Since the atoms of a CNT are periodically located on a pair of helices about the tubular axis, we start the derivation of diffraction patterns from the scattering amplitude of a continuous helix, which is expressed in the cylindrical coordinates for the convenience:

$$F(R,\Phi,l) = \frac{1}{c}\sum_{n=1}^{\infty} z \exp[in(\Phi+\frac{\pi}{2})]$$

$$\times \int_0^c \int_0^{2\pi} \int_0^{\infty} V(r,\varphi,z)J_n(2\pi rR)\exp[i(-n\varphi+\frac{2\pi lz}{c})]rdrd\varphi dz \qquad (2.5.4)$$

where (R,Φ,l) are the cylindrical coordinates in reciprocal space, (r,φ,z) are the cylindrical coordinates in real space, J_n is the n-th order Bessel function, c is the periodicity in the tube axis, and $V(r,\varphi,z) = \frac{2\pi me}{h^2}v(\vec{r})$ is the modified scattering potential.

When the atoms are located on a helix with a radius of r_o and a pitch length C, the modified scattering potential has the following form

$$V(r,\varphi,z) = V_o\delta(r-r_o)\delta(\frac{2\pi z}{C}-\varphi). \qquad (2.5.5)$$

Using Eqn 2.5.5, the scattering amplitude can be expressed as

$$F(R,\Phi,l) = r_0 V_0 J_n(2\pi r_0 R)\exp\left[i\left(\Phi+\frac{\pi}{2}\right)\right], \qquad (2.5.6)$$

For a SWNT, carbon atoms are only located on discrete points of the helix with radius r_0, shown in Fig. 2.4.1, the structure factor become

$$F(R,\Phi,l) = \sum_n \exp[in(\Phi+\frac{\pi}{2})]J_n(2\pi r_0 R)\sum_j f_j\exp[i(-n\varphi_j+\frac{2\pi lz_j}{c})], \qquad (2.5.7)$$

29

where (φ_j, z_j) are the coordinates of carbon atoms, f_j is the atomic scattering amplitude

of carbon, summation j is done over atoms in an asymmetric cell and n over all integers

which are allowed by selection rule ($\dfrac{l}{c} = \dfrac{n}{C} + \dfrac{m}{\Delta}$) discussed later.

Since carbon atoms can be treated as discrete points with an equally spacing Δ on

a continuous helix, as shown in Fig 2.5.1 [26]. The scattering potential of carbon atoms

can be regarded as the product of a continuous helix and these equally spacing points.

The diffraction pattern in reciprocal space is then convolution of the structure factor of

the helix and that of the equally spacing points. This gives the allowed reflections on the

diffraction layer line l through the following selection rule:

$$\frac{l}{c} = \frac{n}{C} + \frac{m}{\Delta}, \tag{2.5.8}$$

where l is the coordinate for $F(R, \Phi, l)$, c is the new structural periodicity in the axial

direction of a single helix in a SWNT, and m is an integer. For a SWNT with chiral

indices (u, v), we have perimeter $A = a_o(u^2 + v^2 + uv)^{1/2}$, pitch length $C = A\tan(60° - \alpha)$,

helical angle $\alpha = \arctan\left(\dfrac{\sqrt{3}v}{v + 2u}\right)$ and the distance between atoms $\Delta = a_o\sin(60° - \alpha)$.

The axial periodicity is given by $c = \sqrt{3}C_h / M$ where M is the maximum common divisor

of $(2u+v)$ and $(u+2v)$. By using these relations, we can rewrite the Eqn. 2.5.8 as

$$l = \left[n(u + wv) + wm(u^2 + v^2 + uv)\right] / uM . \tag{2.5.9}$$
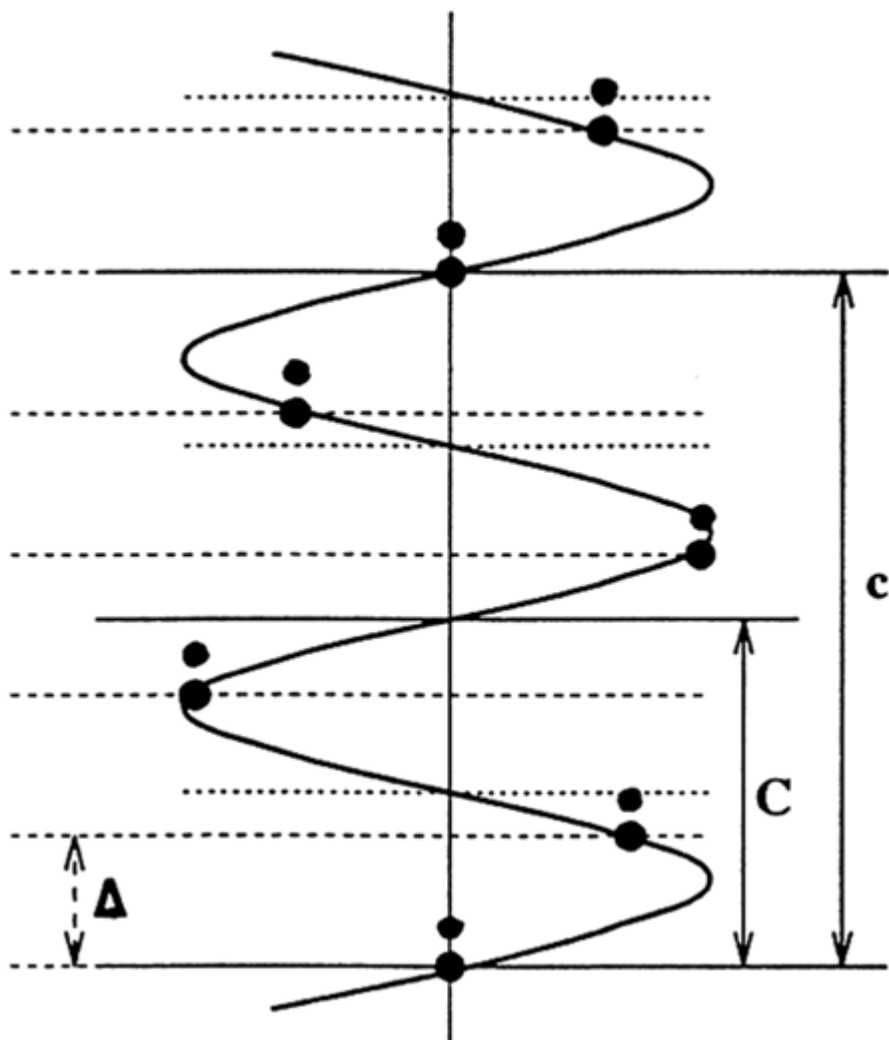
Figure 2.5.1 Schematic of discrete points located on a continuous helix with a pitch length C. Δ is the spacing between two neighboring points group along tubule axis and c is the periodicity of the structure. Figure adapted from [26].

Meanwhile, the positions of carbon atoms in a SWNT can be expressed in cylindrical coordinates in the following equation

$$\begin{cases} x_j^{(1,0)} = -ja_0 cos(30^\circ - \alpha) \\ z_j^{(1,0)} = ja_0 sin(30^\circ - \alpha) \end{cases} \qquad j = 0,1,2,...,v-1 \qquad (2.5.10)$$

and

$$\begin{cases} x_j^{(1,1)} = x_j^{(1,0)} + \dfrac{a_0}{\sqrt{3}} ja_0 cos(30^\circ - \alpha) \\ z_j^{(1,1)} = z_j^{(1,0)} - \dfrac{a_0}{\sqrt{3}} ja_0 sin(30^\circ - \alpha) \end{cases} \qquad j = 0,1,2,...,v-1. \qquad (2.5.11)$$

Plugging Eqn. 2.5.10 and 2.5.11 into Eqn. 2.5.7, we can have the structure factor expressed as

$$F_{uv}\left(R, \Phi, l\right) = \sum_{n,m} f\gamma_{uv}\left(n,m\right)\chi_{uv}(n,m)J_n\left(\pi dR\right)\exp\left[in\left(\Phi + \dfrac{\pi}{2}\right)\right], \qquad (2.5.12)$$

where

$$\gamma_{uv}\left(n,m\right) = 1 + \exp\left[2\pi i\left(-\dfrac{n+(u+2v)m}{3v}\right)\right] \text{ and } \chi_{uv}\left(n,m\right) = \dfrac{1-\exp\left[2\pi i\left[n+(u+v)m\right]\right]}{1-\exp\left[2\pi i\left[n+\dfrac{(u+v)m}{v}\right]\right]}.$$

From the above expression, the structure factor can be divided into two parts: (1) reflections of graphene lattice, which is described as $\sum_{n,m}\gamma_{uv}\left(n,m\right)\chi_{uv}(n,m)$; (2) curvature effects from the cylindrical structure described as $\sum_{n,m}J_n\left(\pi dR\right)\exp[in\left(\Phi + \dfrac{\pi}{2}\right)]$.

The intensity distribution of diffraction pattern is obtained by

$$I_{uv} = | F(R, \Phi, l)|^2. \qquad (2.5.13)$$

The intensity distribution on each allowed diffraction layer is governed by Bessel functions with different orders. But only one specific Bessel function will be dominant in the intensity distribution while the contribution from other Bessel functions are insignificant [24]. This feature actually results in great convenience in the experiment for the determination of the chiral indices of a CNT.

Fig. 2.5.2 is a simulated diffraction pattern of a SWNT [32]. The three primary layer lines l_1, l_2 and l_3, are the most significant diffraction layer lines. They are formed by the (10), $(\bar{1}0)$ and (11) reflections of graphene. The two hexagons indicate the primary Bragg reflections from the top and the bottom surfaces of the carbon nanotube, giving six primary diffraction layer lines on the diffraction pattern. The elongation of the diffraction spots perpendicular to the tubule axis is due to a lack of translational periodicity in this direction. As we can see from the image, the peak of intensity is shifted because of the curvature of the carbon nanotube.

The scattering intensity on the equatorial layer line ($l = 0$) is dominated by Bessel function of order 0 and the intensity is proportional to the square of the zero order Bessel function J_0. The three primary layer lines, l_1, l_2 and l_3 have the values $l_1 = (2u + v)/M$, $l_2 = (u + 2v)/M$ and $l_3 = (u - v)/M$, respectively. By using the selection rule, Eqn. 2.5.9, together with the value of l_1, l_2 and l_3, the order of dominant Bessel function of the three layer lines are solved out to be $n_1 = -v$, $n_2 = u$ and $n_3 = -(u + v)$, respectively. Therefore, the intensities of the 3 primary diffraction layer lines are

$$I(R, \Phi, l_1) \propto |J_v(\pi dR)|^2, \tag{2.5.14}$$

33

$$I\left(R,\Phi,l_2\right) \propto \mid J_u(\pi dR)\mid^2,$$
(2.5.15)

$$I\left(R,\Phi,l_3\right) \propto \mid J_{u+v}(\pi dR)\mid^2.$$
(2.5.16)

Eqn. 2.5.14, 2.5.15 and 2.5.16 provide a way to identify the chiral indices of a SWNT accurately and unambiguously by electron diffraction. Since intensities of the layer line l_1 and l_2 are dominated by the Bessel functions of order v and u, respectively, the order of the Bessel function can be derived from the ratio of the first two peak positions which can be measured directly on the diffraction layer lines. Fig. 2.5.3(a) is the electron diffraction pattern of the SWNT (17, 2) together with the TEM image (inset) of the nanotube. The chiral indices (17,2) are derived from the ratio of first two peak positions, $\dfrac{X_1}{X_2}$ measured on the intensity profiles of the layer lines l_1 and l_2 as illustrated in the Fig. 2.5.3(b) and (c), respectively.

The layer line spacings provide another way to identify the chiral indices of a CNT. As shown in Fig. 2.5.2, the line spacing D_1 and D_2 can be expressed

$$\begin{cases} D_1 = a^* sin(90^\circ - \alpha) \\ D_2 = a^* sin(30^\circ + \alpha) \end{cases}$$
(2.5.17)

where a^* is basis vector of the graphene lattice in reciprocal space. Thus, the helical angle α can be rewritten as

$$\tan(\alpha) = \frac{2D_2 - D_1}{\sqrt{3}D_1},$$
(2.5.18)

Combining the Eqn. 1.2.5 and 2.5.18, the ratio of chiral indices are deduced into

$$\frac{v}{u} = \frac{2D_2 - D_1}{2D_1 - D_2},$$
(2.5.19)

Once the ratio of the chiral indices is obtained from the layer line spacings, the chiral indices can be usually determined unambiguously with supplementary information of tube diameter which can be directly measured from TEM images.

Fig. 2.5.4 shows a diffraction pattern of a DWNT in which the red and the blue arrows are corresponding to the three primary diffraction layer lines from the inner and outer shells, respectively. The chiral indices are determined to be (43, 15) and (48, 21) according to the ratio of spacing of the layer lines l_1 and l_2.
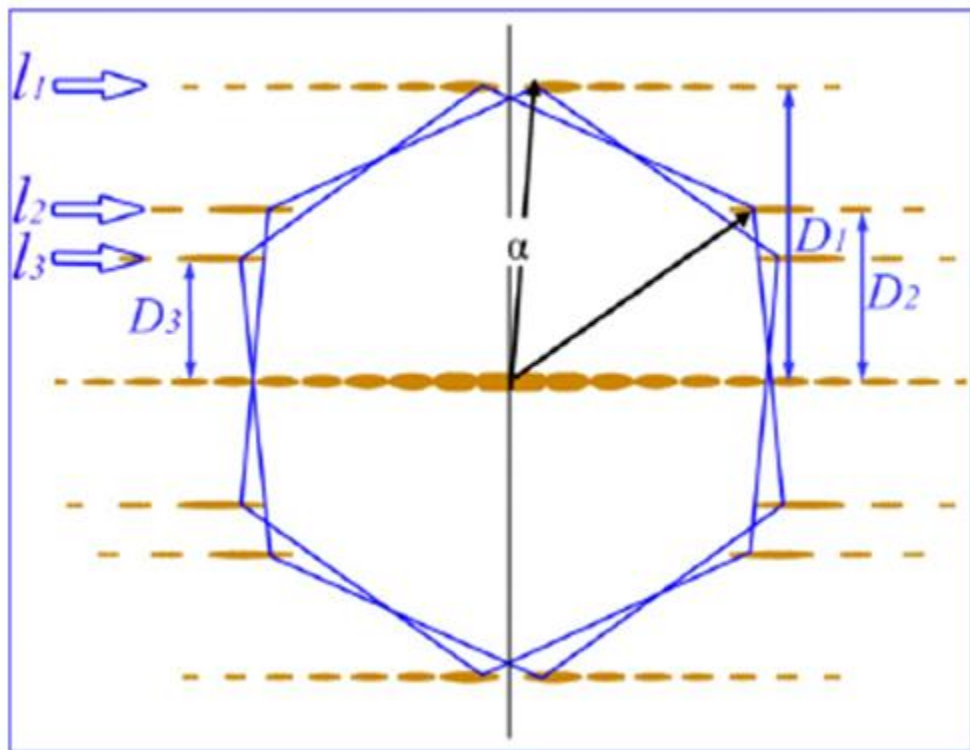
Figure 2.5.2 Simulated electron diffraction pattern of a SWNT. α is the helical angle of the nanotube. l_1, l_2 and l_3 are the primary diffraction layers resulting from the Bragg reflections of indices (1 0, ($\bar{1}$0) and (11) directions. The two hexagons indicate the primary Bragg reflections from the top and the bottom portion of the carbon nanotube, giving six primary diffraction layer lines on the diffraction pattern. D_1, D_2 and D_3 are the spacing between layer lines l_1, l_2 and l_3 and the equatorial line. The elongation of the diffraction spots perpendicular to the tubule axis is due to a lack of translational periodicity in this direction. The peak is shifted because of the curvature of the carbon nanotube. Figure adapted from [32].
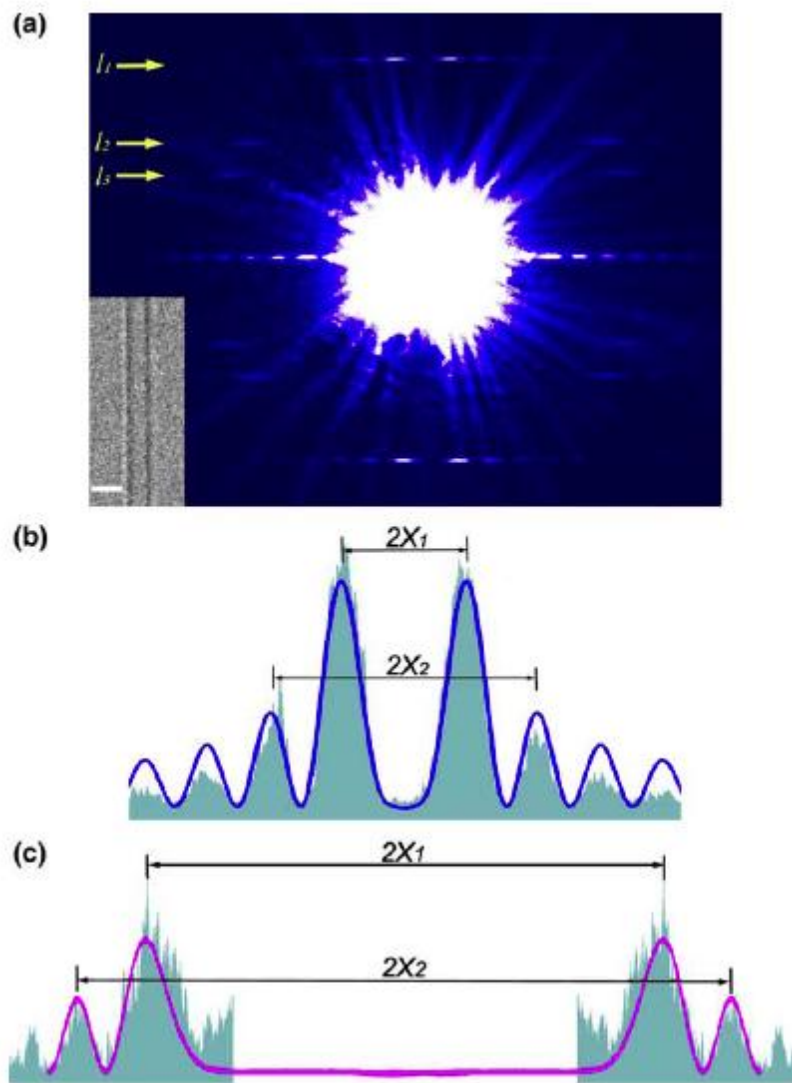
Figure 2.5.3 (a) Electron diffraction pattern of SWNT (17, 2) taken in an experiment. The image is dyed for illustration purpose. Inset is the TEM image of the SWNT. (b) and (c) are the intensity profiles measured along the diffraction layer lines l_1 and l_2. The blue curve and the red curve are the Bessel functions of order 2 and 17 used to fit the peak positions of the diffraction intensity, which is marked by $2X_1$ and $2X_2$ in the figures. Figure adapted from [32].
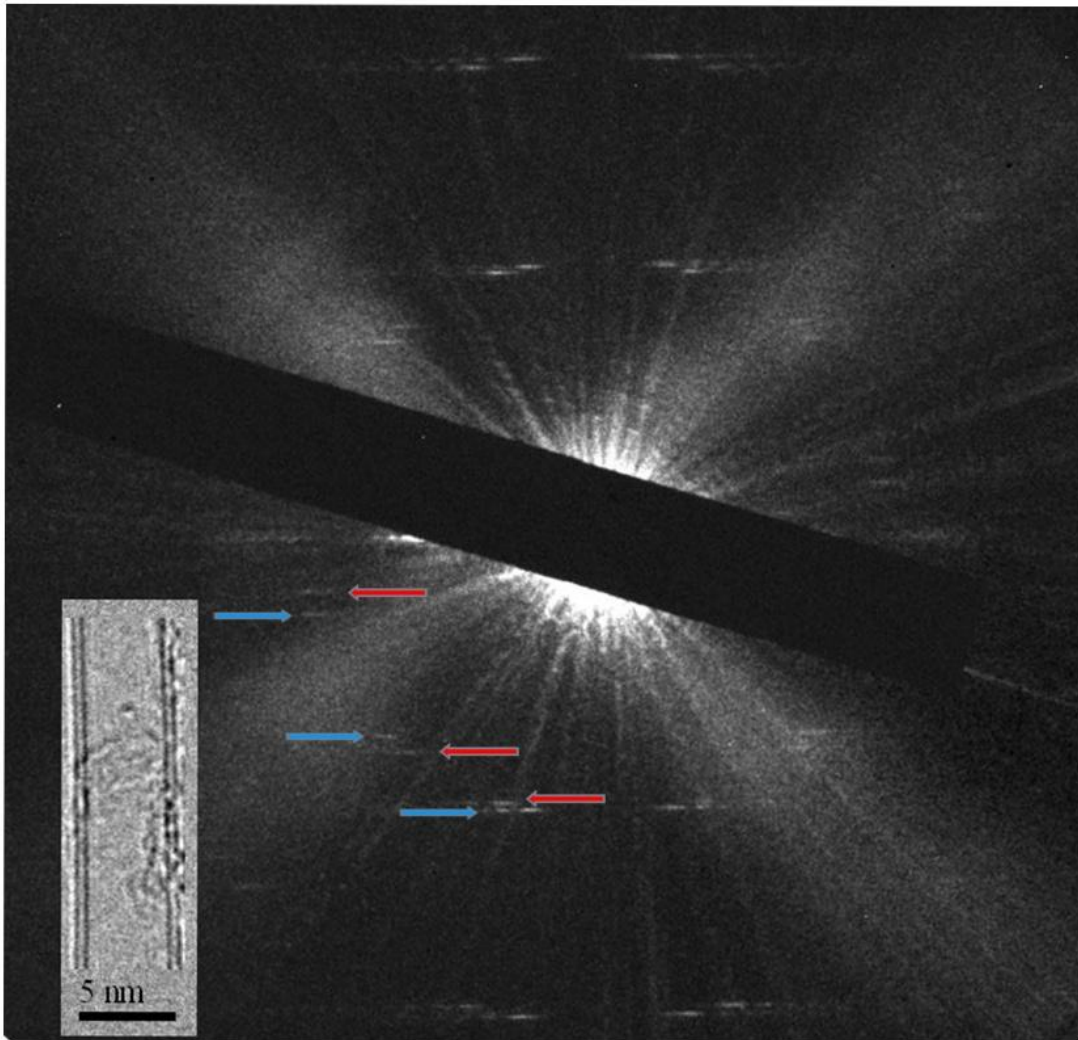
Figure 2.5.4 Electron diffraction pattern of a DWNT of chiral indices (43, 15) and (48, 21). The red and blue arrows point to the diffraction layer lines coming from (43, 15) and (48, 21), respectively. Inset is the TEM image of the DWNT.

2.6 References

[1]   Wildoer, J. W. G., Venema, L. C., Rinzler, A. G., Smalley, R. E. & Dekker, C., Electronic Structure of Atomically Resolved Carbon Nanotubes. *Nature* **391**, 59-62 (1998).

[2]   Odom, T. W., Huang, J. L., Kim, P. & Lieber, C. M., Atomic Structure and Electronic Properties of Single-Walled Carbon Nanotubes. *Nature* **391**, 62-64 (1998).

[3]   Hassanien, A., Tokumoto, M., Kumazawa, Y., Kataura, H., Maniwa, Y., Suzuki, S. & Achiba, Y., Atomic Structure and Electronic Properties of Single-Wall Carbon Nanotubes Probed by Scanning Tunneling Microscope at Room Temperature. *Appl. Phys. Lett.* **73**, 3839-3841 (1998).

[4]   Hertel, T., Walkup, R. E. & Avouris, P., Deformation of Carbon Nanotubes by Surface Van Der Waals Forces. *Phys. Rev. B* **58**, 13870-13873 (1998).

[5]   Wong, E. W., Sheehan, P. E. & Lieber, C. M., Nanobeam Mechanics: Elasticity, Strength, and Toughness of Nanorods and Nanotubes. *Science* **277**, 1971-1975 (1997).

[6]   Rubio, A., Spectroscopic Properties and Stm Images of Carbon Nanotubes. *Appl. Phys. A-Mater. Sci. Process.* **68**, 275-282 (1999).

[7]   Giusca, C. E., Tison, Y., Stolojan, V., Borowiak-Palen, E. & Silva, S. R. P., Inner-Tube Chirality Determination for Double-Walled Carbon Nanotubes by Scanning Tunneling Microscopy. *Nano Lett.* **7**, 1232-1239 (2007).

[8]   Dresselhaus, M. S., Dresselhaus, G., Saito, R. & Jorio, A., Raman Spectroscopy of Carbon Nanotubes. *Phys. Rep.-Rev. Sec. Phys. Lett.* **409**, 47-99 (2005).

[9]   Jorio, A., Saito, R., Hafner, J. H., Lieber, C. M., Hunter, M., McClure, T., Dresselhaus, G. & Dresselhaus, M. S., Structural (N, M) Determination of Isolated Single-Wall Carbon Nanotubes by Resonant Raman Scattering. *Phys. Rev. Lett.* **86**, 1118-1121 (2001).

[10]   Telg, H., Maultzsch, J., Reich, S., Hennrich, F. & Thomsen, C., Chirality Distribution and Transition Energies of Carbon Nanotubes (Vol 93, Art No 177401, 2004). *Phys. Rev. Lett.* **93** (2004).

[11]   Benoit, J. M., Buisson, J. P., Chauvet, O., Godon, C. & Lefrant, S., Low-Frequency Raman Studies of Multiwalled Carbon Nanotubes: Experiments and Theory. *Phys. Rev. B* **66** (2002).

[12]   Zhao, X. L., Ando, Y., Qin, L.-C., Kataura, H., Maniwa, Y. & Saito, R., Radial Breathing Modes of Multiwalled Carbon Nanotubes. *Chem. Phys. Lett.* **361**, 169-174 (2002).

[13]   Lian, Y. F., Maeda, Y., Wakahara, T., Akasaka, T., Kazaoui, S., Minami, N., Choi, N. & Tokumoto, H., Assignment of the Fine Structure in the Optical Absorption Spectra of Soluble Single-Walled Carbon Nanotubes. *Journal of Physical Chemistry B* **107**, 12082-12087 (2003).

[14]   Liu, X., Pichler, T., Knupfer, M., Golden, M. S., Fink, J., Kataura, H. & Achiba, Y., Detailed Analysis of the Mean Diameter and Diameter Distribution of Single-Wall Carbon Nanotubes from Their Optical Response. *Phys. Rev. B* **66** (2002).

[15]   Kataura, H., Kumazawa, Y., Maniwa, Y., Umezu, I., Suzuki, S., Ohtsuka, Y. & Achiba, Y., Optical Properties of Single-Wall Carbon Nanotubes. *Synth. Met.* **103**, 2555-2558 (1999).

[16]   Jost, O., Gorbunov, A. A., Pompe, W., Pichler, T., Friedlein, R., Knupfer, M., Reibold, M., Bauer, H. D., Dunsch, L., Golden, M. S. & Fink, J., Diameter Grouping in Bulk Samples of Single-Walled Carbon Nanotubes from Optical Absorption Spectroscopy. *Appl. Phys. Lett.* **75**, 2217-2219 (1999).

[17]   Broglie, L. D., Research on the Theory of Quanta. *Ann. De Physiques* **3**, 107 (1925).

[18]   Busch, H., On the Modes of Action of the Concentrating Coil in the Braun Tube. *Arch. Electrotechnik* **18**, 12 (1927).

[19]   Knoll, M. & Ruska, E., The Electron Microscope. *Physik* **78**, 22 (1932).

[20]   Born, M. & Wolf, E., *Principles of Optics* 1964).

[21]   Joy, D. C., Romig, A. D. & Goldstein, J., *Principles of Analytical Electron Microscopy* (Plenum Press, New York, 1986).

[22]   Deniz, H., Electron Diffraction and Microscopy Study of Nanotubes and Nanowires. PhD Thesis, The University of North Carolina at Chapel Hill, (2007).

[23]   Cowley, J. M., *Diffraction Physics* (North-Holland Pub. Co. ; Sole distributors for the U.S.A. and Canada, Elsevier North-Holland, Amsterdam; New York; New York, 1981).

[24]   Liu, Z., Atomic Structure Determination of Carbon Nanotubes by Electron Diffraction. PhD Thesis, The University of North Carolina at Chapel Hill, (2005).

[25]   Hanszen, K. J., Problems of Image Interpretation in Electron Microscopy with Linear and Nonlinear Transfer. *Zeitschrift Fur Angewandte Physik* **27**, 125-& (1969).

[26]   Qin, L.-C., Electron Diffraction from Carbon Nanotubes. *Rep. Prog. Phys.* **69**, 2761-2821 (2006).

[27]   Qin, C. & Peng, L. M., Measurement Accuracy of the Diameter of a Carbon Nanotube from Tem Images. *Phys. Rev. B* **65** (2002).

[28]   Qin, L.-C., Electron-Diffraction from Cylindrical Nanotubes. *J. Mater. Res.* **9**, 2450-2456 (1994).

[29]   Lambin, P. & Lucas, A. A., Quantitative Theory of Diffraction by Carbon Nanotubes. *Phys. Rev. B* **56**, 3571-3574 (1997).

[30]   Lucas, A. A., Bruyninckx, V. & Lambin, P., Calculating the Diffraction of Electrons or X-Rays by Carbon Nanotubes. *Europhys. Lett.* **35**, 355-360 (1996).

[31]   Cochran, W., Citation-Classic - the Structure of Synthetic Polypeptides .1. The Transform of Atoms on a Helix. *Current Contents/Physical Chemical & Earth Sciences*, 16-16 (1987).

[32]   Liu, Z. J. & Qin, L.-C., A Direct Method to Determine the Chiral Indices of Carbon Nanotubes. *Chem. Phys. Lett.* **408**, 75-79 (2005).

Chapter 3

Experimental Techniques

3.1 Introduction

All the experiments detailed in this thesis are done on a nano-electromechnical device built on a suspended CNT. The advantage of such a device is that it allows us to take the *in situ* CNT electron diffraction patterns while measuring its electrical and mechanical properties. The fabrication of the devices requires a lot of specialized nano-device techniques. Some are routine fabrication techniques, such as photolithography and electron beam lithography. These methods will only be discussed briefly. However, the more original methods and skills are required for the success of fabricating high quality suspended CNT devices. They will be discussed in more detail in this chapter. A customized TEM specimen holder for these nano-electromechnical devices is also designed and constructed. It is capable of *in situ* electro-mechanical measurement via feed-through electrical probes. The details of the TEM holder will be described in the last section of this chapter.

3.2 Carbon Nanotube Deposition

Since the discovery of CNT [1], there have been three major methods to grow SWNTs or MWNTs: (a) arc-discharge evaporation of graphite [1-5]; (b) laser ablation of graphite [6-9]; and (c) chemical vapor deposition [10-20]. They will only be discussed briefly here to explain the reason why chemical vapor deposition is chosen for my devices.

In an arc-discharge synthesis, a DC or AC voltage is applied between two graphite electrodes which are separated by about 1 mm to create discharge plasma. The material on the anode is evaporated by high temperature plasma and is condensed on the cathode. Carbon nanotubes are found in the deposits on the cathode. When transition metals are present in the anode serving as catalysts, SWNTs can be synthesized on the cathode. Otherwise, only MWNTs are produced in the deposits [2].

In the laser ablation method, a solid carbon target is placed in a quartz tube at high temperature. A pulsed laser is used to blast and to evaporate the carbon target. The products are found to be 90% pure CNT. If the target contains transition metal catalysts such as Rh/Pd and Ni/Co [6, 7], SWNT can be synthesized. Otherwise, products only contain MWNTs.

The CNTs synthesized by both arc-discharge method and laser ablation method are in the form of black carbon soot. In order to make a single MWNT (number of shells larger than 2) device on a silicon based substrate, the products are usually suspended in dichloromethane because nanotubes tend to suspend freely in non-polar solvents. For MWNT deposition onto the substrate, a diluted drop of MWNT solution is mixed with several drops of isoproponal and is placed onto the substrate. The addition of isoproponal

can change the polarity of the MWNTs and makes the MWNTs easily to disperse on the substrate from the solution. The substrate is ready for further fabrication after it is dried under nitrogen flow.

The dispersion of individual SWNTs or DWNTs on substrate is more challenging than MWNTs by the above method due to nanotube bundling, resulted from their low mass-to-surface area ratio. Surfactants or organic polymers are usually added into the nanotube solution to debundle carbon nanotubes by attaching positive or negative chemical molecules on the surface of nanotubes to overcome the attractive van der Waals force within the nanotube bundles [21, 22]. These suffactants can be removed later from nanotubes by changing solvent or by smooth oxidation. The result is good for dispersing CNTs on carbon grids for TEM imaging, but is far from being satisfied for dispersing individual CNTs uniformly on silicon substrate at a low concentration. The device fabrication requires a CNT density of about 5 nanotubes per one hundred square micrometers on the substrate. Thus, dispersion by liquid solution requires a CNT solution with a very low concentration. However, effects of surfactants in such a low concentration solution are not good and the individual CNT deposition is often not certain. Furthermore, the removal of surfactants by oxidation can very easily burn nanotubes or results in structural defects, especially when the number of nanotubes is small.

Contrary to the arc-discharge or the laser ablation method, chemical vapor deposition can grow SWNTs or DWNTs directly onto a silicon substrate with a desired density which is controlled by the density of catalysts dispersed on the substrate. In this method, a silicon based substrate dispersed with metal catalysts is placed in a quartz tube

at high temperature. When passing through the quartz tube, organic gases are thermally decomposed and carbon nanotubes grow on the catalysts. It requires the catalyst particles, which usually contain Fe or Ni nano-particles, be of very small diameter (<10 nm). Since the nanotubes are grown on the catalysts, the density of CNT on the substrate can be precisely controlled by the catalyst density dispersed on the substrate.

3.3 CNT Synthesis by Chemical Vapor Deposition

The CNTs in our experiment are grown by chemical vapor deposition. Different catalysts, silicon based substrates and growth methods guided by Dr Jie Liu's group in Duke University have been tried to achieve the required CNT deposition density on the device substrates [16-20, 23].

Fe/Mo nano-particles are first used as the catalysts for SWNT synthesis in the CVD system. The catalysts are diluted into 1:100000 in hexane and then dispersed onto the silicon substrate. The substrates are annealed in air at $700\,^{\circ}C$ for 10 minutes and then feeding gases consisting of methane, ethylene and hydrogen are purged through at $900\,^{\circ}C$ for CNT synthesis. The products are all SWNT nanotubes with diameter distributed between 2nm to 5nm. Fig. 3.3.1 shows a typical SEM image of the SWNTs produced in this method. The distribution of SWNTs is not uniform on the substrate because the catalyst particles aggregate during the quick evaporation of hexane on the substrate surface.

Figure 3.3.1 SEM image of SWNTs using Fe/Mo nano-particles as catalysts.

The quartz wafer (as the substrate) and iron chloride (as catalysts) are used to grow long and straight CNTs. The catalysts diluted in toluene are dispersed on the quartz wafer and then the wafer is transferred to the furnace at $900\,^{\circ}C$. The feeding gases consisting of methanol and ethanol are purged though the tube for CNT growth for 10 minutes. The results turn out that the nanotubes are all SWNTs and are grown strictly along the (100) direction on the quartz wafer at the density of about 20 nanotubes per micrometer as illustrated in the Fig. 3.3.2. The SWNT can be transferred from the quartz wafer to the silicon substrate by sticking CNTs on a thick PMMA layer. The diameter is distributed from 1.5 nm to 3 nm sampled in TEM by transferring SWNTs to trenches on silicon nitride TEM grid as illustrated in Fig. 3.3.3. However, the density of CNTs is too high for fabricating individual CNT devices.
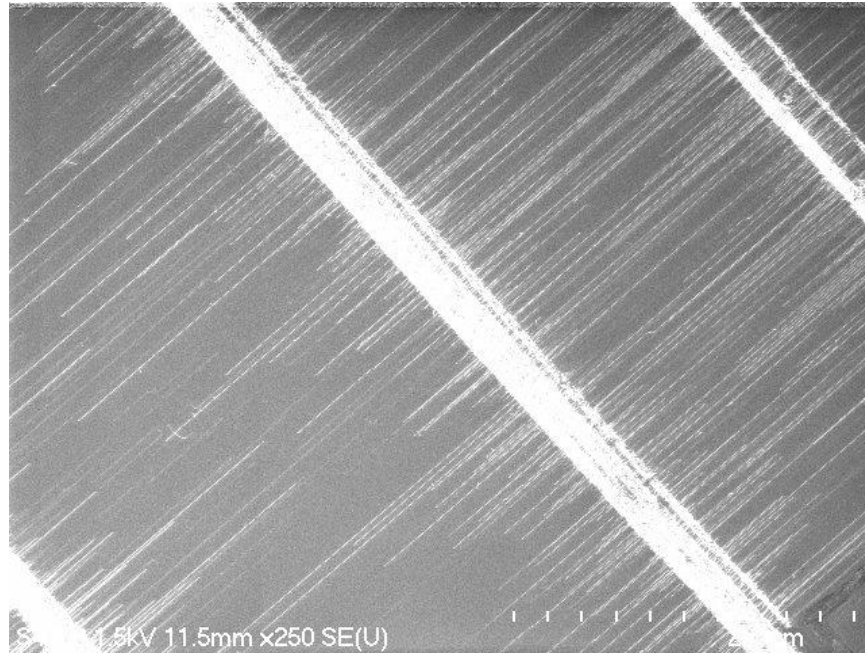
Figure 3.3.2 SEM images of SWNTs using quartz wafer as the substrate and iron chloride as catalysts.
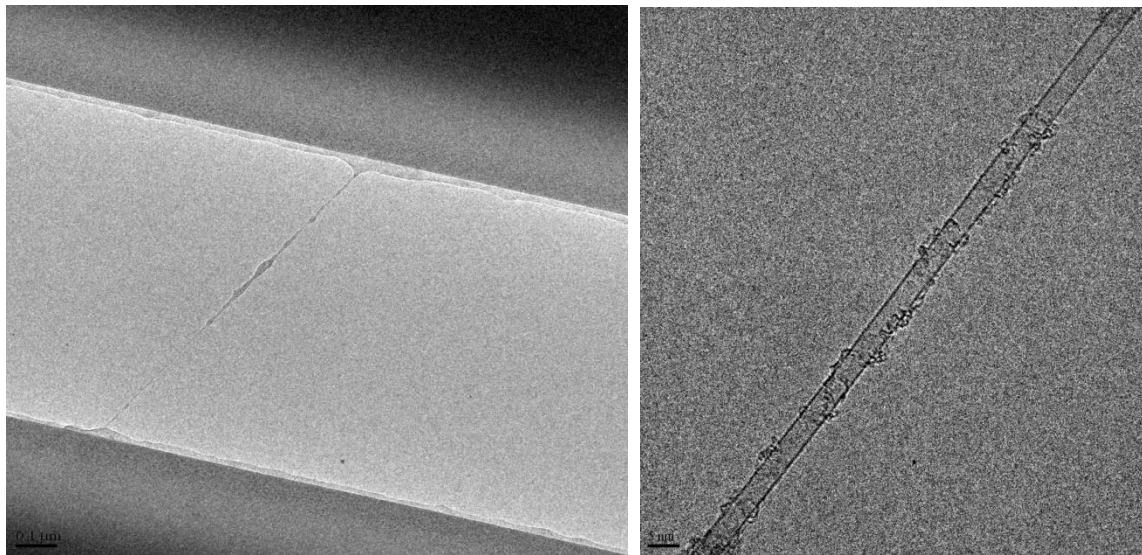
Figure 3.3.3 Low resolution (left) and high resolution (right) TEM images of a SWNT transferred from the SWNTs in Fig. 3.3.3. Scale bars, 100 nm (left) and 5 nm (right).

In order to grow long nanotubes and reach the required SWNT/DWNT density on the silicon substrate, the following method is finally chosen in our experiments (the details of the growth method are discussed in Appendix I) [18]. For a DWNT growth, $FeSi_2$ is used as the metal catalyst. The $FeSi_2$ is first crushed into small particles and then is soaked in ethanol. The catalysts are deposited onto the substrate by evaporation of the catalyst suspension. The substrate is heated in a 2.5 cm quartz tube in air at $900\ ^o C$ for 20 minutes and followed by a 10 minutes purge of Ar to remove the air. The temperature is raised to $925\ ^o C$ and carbon feeding gases, which consist of methane (1500 sccm), ethylene (30 sccm), and hydrogen (500 sccm), are introduced into the tube for nanotube growth. After 10 minutes of growth, argon, methane and ethylene gases are turned off. The system is cooled to room temperature in the purge process with hydrogen gas. The products show a DWNT percentage of more than 90% without any purification and a DWNT diameter of $4.5 \pm 0.5\ nm$, as illustrated in Fig. 3.3.5 [18]. Fig. 3.3.6 is a TEM image of a DWNT grown across the trench on a silicon nitride membrane. In SWNT growth, most procedures are the same as that of DWNT, but iron nitrate is usually used as metal catalyst and no anneal procedure is needed.
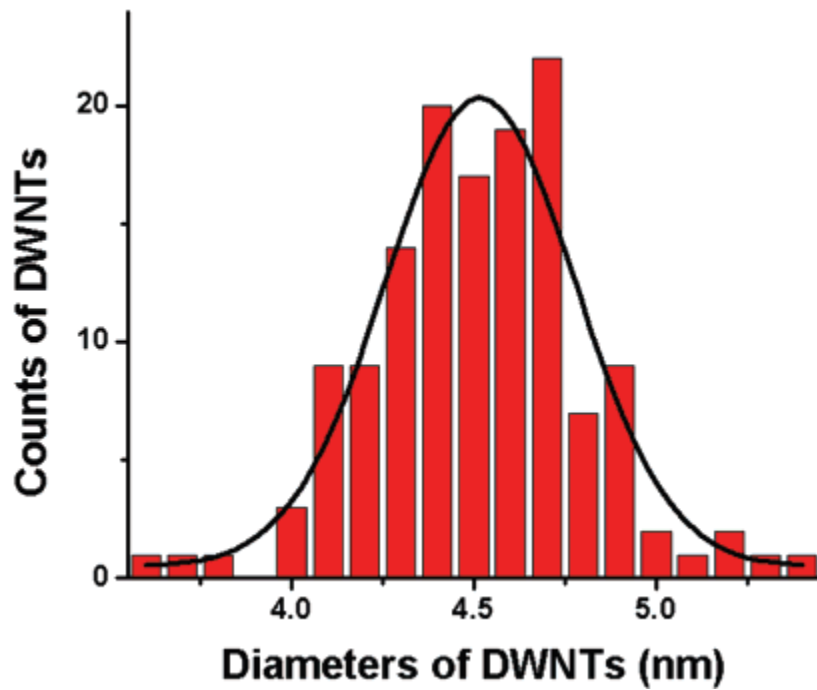
Figure 3.2.5 Diameter distribution of DWNT grown by chemical vapor deposition directly onto a substrate. The image is adapted from [18].
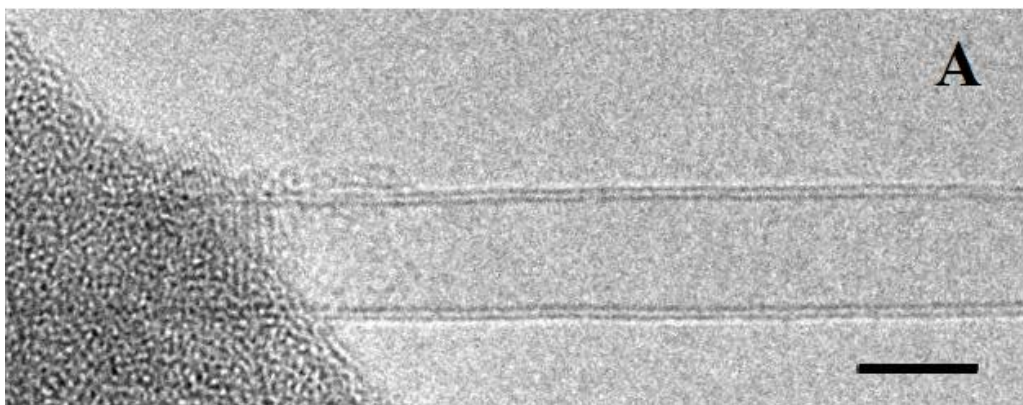
Figure 3.2.6 High resolution TEM image of a DWNT grown across a trench on a silicon nitride membrane by the chemical vapor deposition method. The scale bar is 5 nm.

3.4 Nano-Electromechanical Device Based on a Suspended CNT

Two types of CNT devices are used in this thesis to study the correlations between the nanotube properties and its chiral structure. In the first type of device, a single carbon nanotube is suspended in air between two or four anchoring electrodes which are used to measure the electrical resistance of the CNT. In the second type of device, a single carbon nanotube, which is suspended between two anchoring electrodes, works as a torional bearing attached with a metal anchor. An external electric field is applied via a side gate to actuate the metal paddle and thus to twist the nanotube, as illustrated in Fig. 3.3.1. The torsional strains and the corresponding electromechanical response of the CNT can be measured simultaneously on this type of device. The details of device fabrication will be described in Appendix II. Due to the similarities between two types of devices, this section focuses on a brief description of the fabrication of the second type device.

(1) Positive photolithography is performed on the back side of the wafer, Fig. 3.3.2(A). A commercial photoresist (Shipley S1813) is spin-coated (3000 rpm for 60s) on the wafer backside. After soft baking the sample on a hot plate at 115℃ for 1 minute, the sample is cooled down and transferred to a mask aligner (Karl Suss MA6/BA6). Ultraviolet light (wavelength 365 nm) is used to expose the photoresist through a photomask which is patterned with a matrix of 1 mm×1 mm squares separated by 10 mm. Then, the sample is dipped into a developer solution (Rohm and Haas MF 319) to remove the de-crosslinked regions.
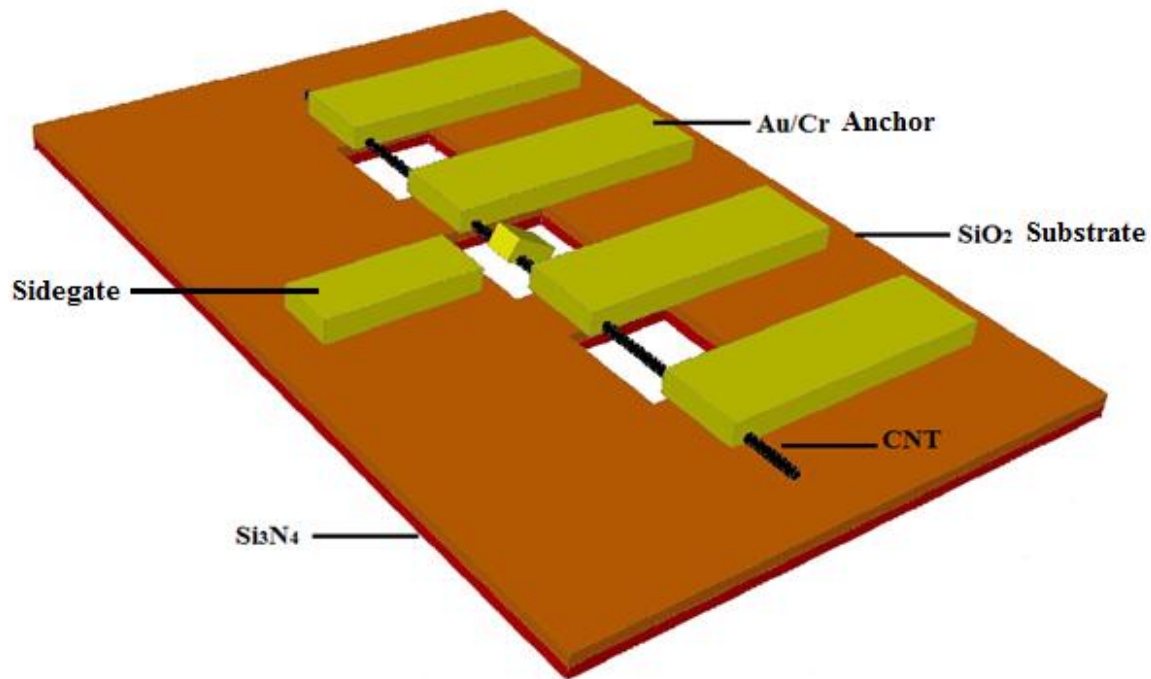
Figure 3.3.1 Schematic of CNT torsional device. A metal paddle is suspended on an individual CNT which is held by two metal anchors across an opening etched on a membrane consisting of 300 nm silicon dioxide and 300 nm silicon nitride. A side gate is placed aside to actuate the metal paddle by an applied voltage.

(2) The silicon nitride layer on top of which the photoresist has been removed is etched away in a reactive ion etching (RIE) process, as illustrated in Fig. 3.3.2(B). The sample is placed in the RIE chamber at an atmosphere of C_3F_8 and O_2 gases. Chemically reactive plasma are induced in the chamber by an electromagnetic field to etch the exposed silicon nitride layer. The rest of the wafer is protected from etching by photoresist. The photoresist is removed by sonication in acetone for 30 seconds after etching.

(3) The sample is placed in 15% potassium hydroxide solution at $70°C$ for silicon etching, as illustrated in Fig. 3.3.2(C). Potassium hydroxide is an anisotropic silicon

etchant and etches the silicon (100) with an angle of $54.74°$ from the plane at a speed about 1 μm per minute. The silicon nitride layers coated on both sides of the wafer work as a KOH stopper to protect the silicon beneath from etching. Only the areas on top of which the nitride layer is etched away by RIE in the last step are exposed to KOH. The etching process is stopped when the etching depth reaches 400 μm, leaving a 100 μm silicon layer which works as a support to protect the underlying nitride layer from breaking in future sonication. The entire process is supervised in an optical microscope in case the sample is over-etched.

(4) A 50 nm silicon nitride layer and a 300 nm silicon dioxide layer are deposited onto the top surface of the sample by plasma enhance chemical vapor deposition (PECVD), Fig. 3.3.2(D). Although silicon nitride is a good etchant stopper in KOH solution, the defects on the nitride layer will be enlarged and thus the local nitride will be etched through by KOH in a long time etching process (usually about several hours). This effect results in pin holes (on the micrometer order) on the surface. As the result, circuit fabricated on the surface will be short to the substrate if metal happens to be deposited on these pin holes. Therefore, a 50 nm PECVD silicon nitride layer is first coated on the wafer surface to block these pin holes. Another 300 nm silicon dioxide layer is deposited onto the substrate for CNT growth.

(5) CNTs are grown onto the sample surface by chemical vapor deposition as mentioned in the last section. The samples are checked by SEM to ensure that there are enough CNTs on the wafer for the next step fabrication.
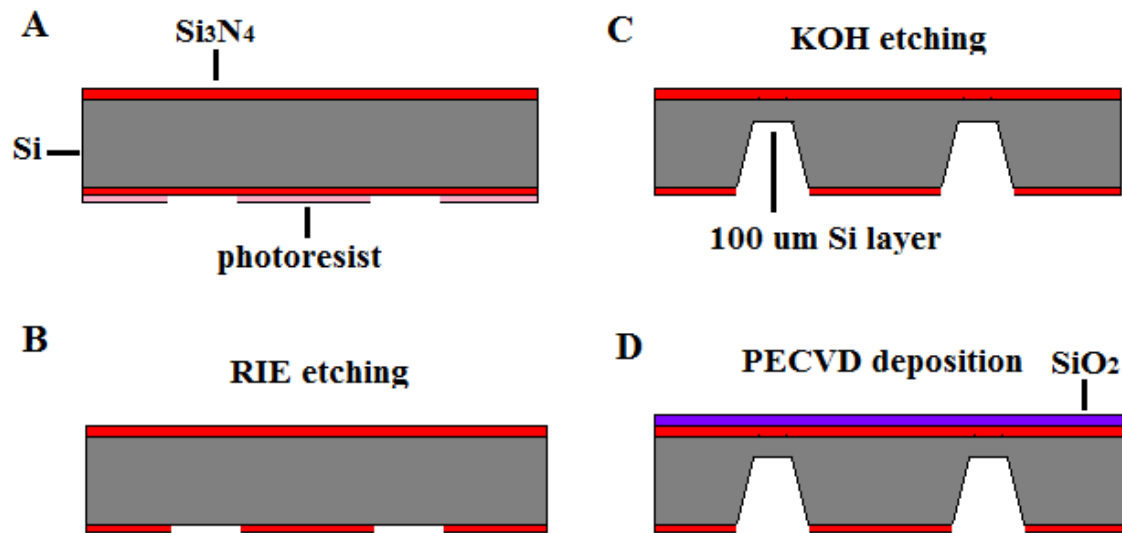
Figure 3.3.2 Schematic of the first 4 steps of device fabrication. (A) Photolithography is performed on the backside of the wafer. The photoresist protects the covered area from RIE etching. (B) RIE etching is applied to etch the silicon nitride without the protection of photoresisit. (C) The sample is dipped in 15% KOH solution for silicon etching. Etching is stopped when the etching depth reaches 400 μm. 100 μm silion layer is left as a support for the silicon nitride layer. (D) A 40 nm silicon nitride film and 300 nm dioxide film is deposited onto the top surface of the wafer by PECVD.

(6) Another positive photolithography is performed on the top surface of the samples. The procedure is the same as those discussed in the first step. The only difference is that a different photo mask patterned with electric circuits is used here. The samples are carefully aligned to the mask so that the micro-electrodes will be patterned onto the places which are right on the top of those trenches etched on the backside in the last step. Following directional evaporation of metal (10 nm Cr and 60 nm Au) onto the patterned wafer, all the photoresist is removed with an acetone soak. Metal deposited atop the resist is removed along with the resist by acetone soak, leaving metal where exposure occurred. The surface is patterned with eight individually addressable

macroscopic electrodes that decrease in size to an 80 μm × 80 μm area where devices are to be fabricated, marked by the circle as illustrated in Fig. 3.3.3 [24].
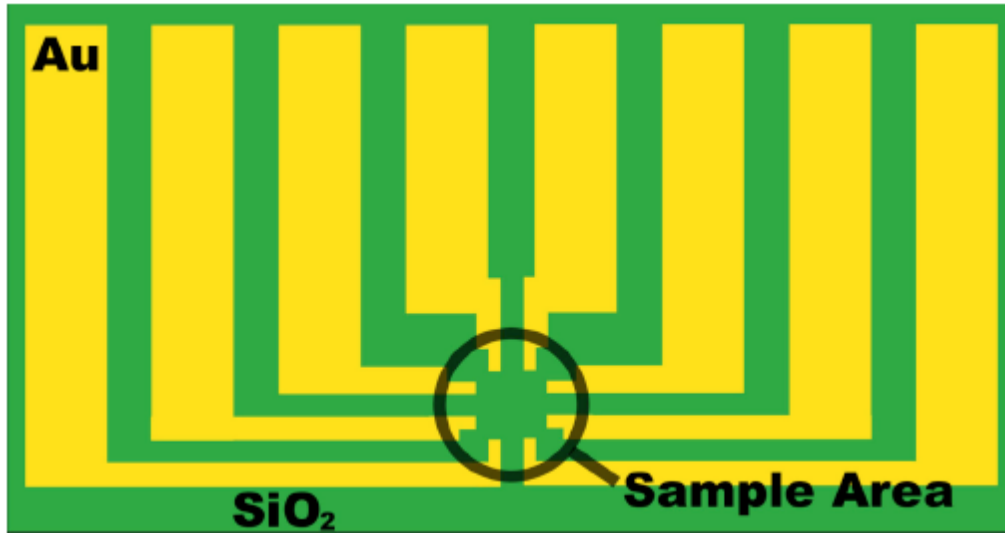
Figure 3.3.3 Schematic of the macroscopic electrodes deposited onto a wafer by photolithography. The schematic is not drawn to scale for illustration purpose. Adapted from [24].

(7) CNTs are broken apart by applying a large current (tens of micro amperes) between the neighboring electrodes if the CNTs are bridging multiple leads as illustrated in Fig. 3.3.4(A) and (B). The large amount of heat generated as a large current (about $10 - 40$ μA) passing through CNTs causes the oxidation of carbon atoms and thus breaks the nanotubes. As the result, the applied current will become immeasurable once the nanotube is broken.

(8) Two steps of electron beam lithography are performed on the sample: the 1st lithography for small fiduciary marks used as the precise location marks of CNTs for the metal patterns in the 2nd lithography; the 2nd lithography for patterning metal anchors and paddles onto the nanotubes as illustrated in Fig. 3.3.4(B) and (D). The procedure of

electron beam lithography is very similar to that of photolithography, except that the photoresist is replaced by electron beam resist poly methyl methacrylate (PMMA) here. A low molecular weight (M=350 K) PMMA is spin-coated on the sample at the spin speed of 5000 rpm, and then subject to a soft bake (180 ℃) for 2 minutes on a hot plate. A second layer PMMA (M=996K) is spin-coated on the sample at the spin speed of 4000 rpm, and then subject to a 2 hours bake (180 ℃) in a furnace to remove the solvent. After exposed to electron beam, the sample is soaked in developer (mixture of methyl isobutyl ketone and isoproponal at the ratio of 1: 3) to remove the exposed PMMA. Thermal evaporation is followed to deposit 10 nm Cr and 80 nm Au onto the sample surface. The metal atop the undeveloped PMMA is removed by acetone soak, leaving the substrate-bound areas only where exposure occurred. Double PMMA layers are used to help metal peel off in acetone soak. Since the lighter PMMA is more sensitive to electron beam than the heavier PMMA, it will be de-crosslinked more under the same electron dose and give an undercutting gutter after lithography, as illustrated in Fig. 3.3.5. Such a shape makes the metal atop the PMMA more easily to peel off when the underlying PMMA is dissolved in acetone.

(9) A wet etching process is used to remove the 100 μm silicon layer underlying the devices, as shown in Fig. 3.3.6 (A) and (B). The sample is placed up-side down on a hot plate at 60 ℃ and HNA (the solution mixed by hydrofluoric acid, nitric acid and acetic acid) is dripped into the trenches which are etched in the third step to remove the remaining 100 μm silicon layer, leaving a 300 nm nitride and 300 nm silicon dioxide membranes to support the devices. HNA can etch the silicon at a speed about 2 μm per minute at 60 ℃.
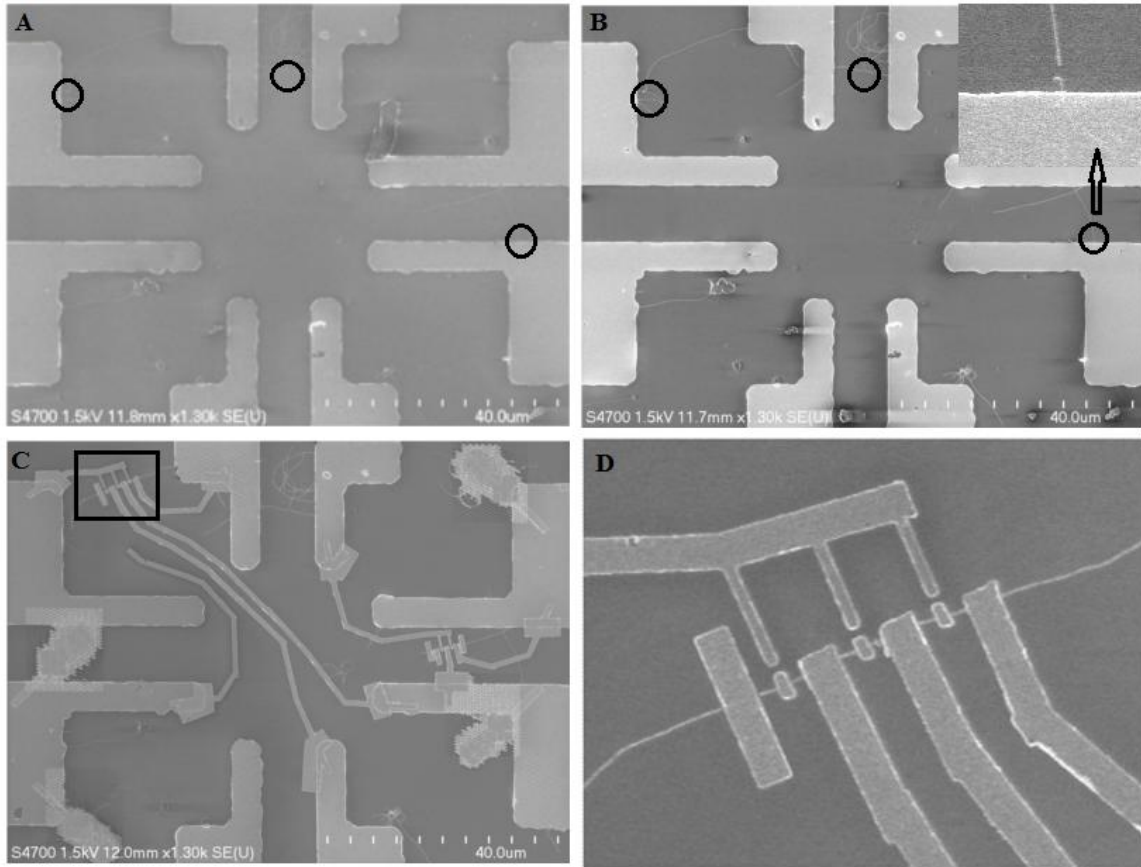
Figure 3.3.4 (A) SEM image of the device area before electron beam lithography. The CNTs marked by black circle bridge the neighboring electrodes and are broken by applying a large electric current. (B) The nanotubes are broken after a large current oxidizes the carbon atoms. The inset is an enlarged SEM image where the CNT is broken point. (C) SEM image of the device after metal paddles and anchors are patterned. (D) An enlarged SEM device image of the area marked by the rectangle in (C).
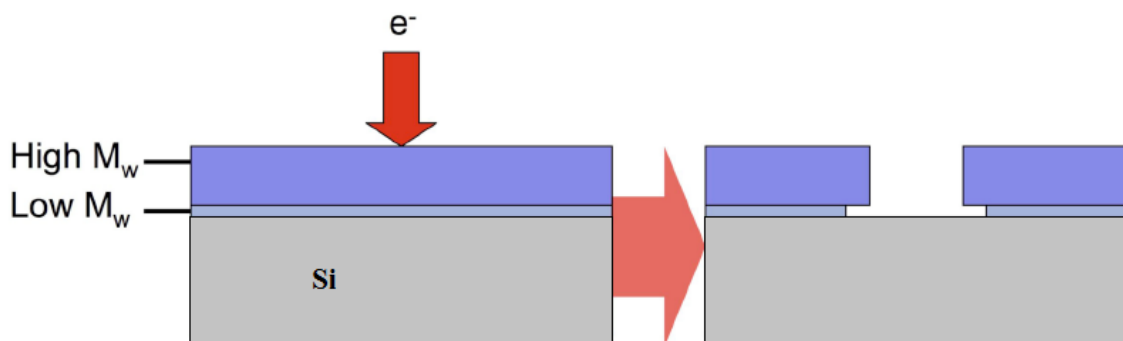
Figure 3.3.5 Schematic of bilayer PMMA for electron beam lithography, resulting in a desirable T-structure (right) and low remnant material on the surface. Adapted from [18].

(10) Focused ion beam (FIB) is used to etch away the silicon nitride layer right below the CNT device as illustrated in Fig. 3.3.6(C). A cross fiduciary mark used as alignment mark is first etched through on the front side of the device. Then, the device is flipped 180° and the positions of CNT devices on the membrane are located according to the fiduciary mark. Windows with a size of 1.2 μm×1.8 μm are etched on these positions, leaving a 300 nm silicon dioxide layer to support the devices.

(11) Buffered hydrofluoric acid (BHF) is used to etch the 300 nm silicon dioxide layer which is left in the last step to fully suspend the nanotube and the paddle on the tube as illustrated in Fig. 3.3.6(C). PMMA (M=996 K) is first spin-coated onto the sample surface, working as a BHF stopper. Another electron beam lithography is then performed on the sample to open a 0.4 μm×0.8 μm etching window on the device, leaving the rest of sample protected by PMMA from BHF. A drop of BHF is placed onto the device for 5 minutes to etch away the silicon dioxide layer.

(12) In the final step, the sample is dried by (super)critical point drying, which prevents the suspended nanotube devices from being exposed to surface tension during evaporative drying, which generally causes devices to fail. The sample is first submerged in acetone to remove the PMMA. Then the sample is transferred to ethanol and immediately dried using supercritical carbon dioxide. The final device is then complete and ready for experimentation as illustrated in Fig. 3.3.6(D) and Fig. 3.3.7.
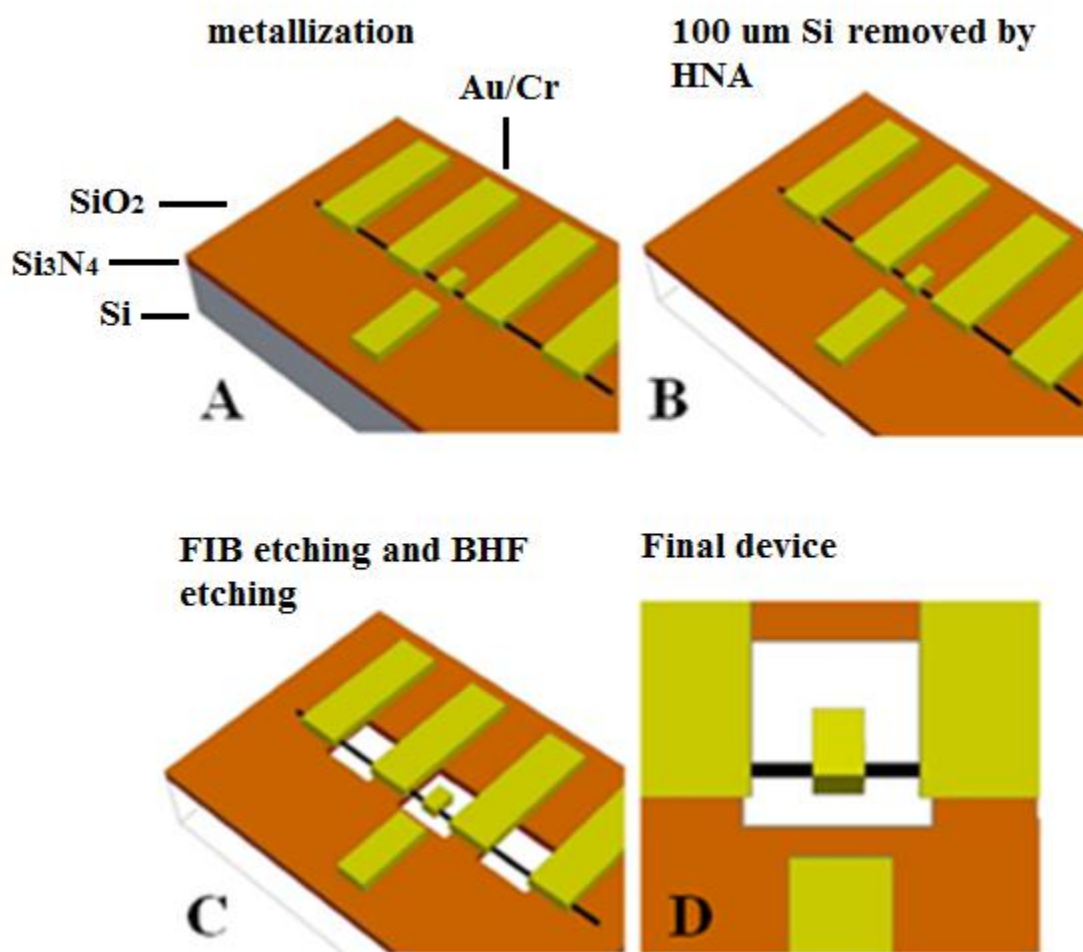
Figure 3.3.6 Schematic of device fabrication step 8 to 12. (A) Electrodes and paddles are patterned onto CNTs by electron beam lithography followed by metallization. (B) HNA is dripped into the tenches etched on the backside of the wafer to remove the 100 μm silicon layer. (C) FIB is performed to remove the silicon nitride layer right underlying the metal paddle and BHF is used to remove the silicon dioxide layer underlying the paddle, leaving the paddle suspended in air. (D) The schematic of a final device.
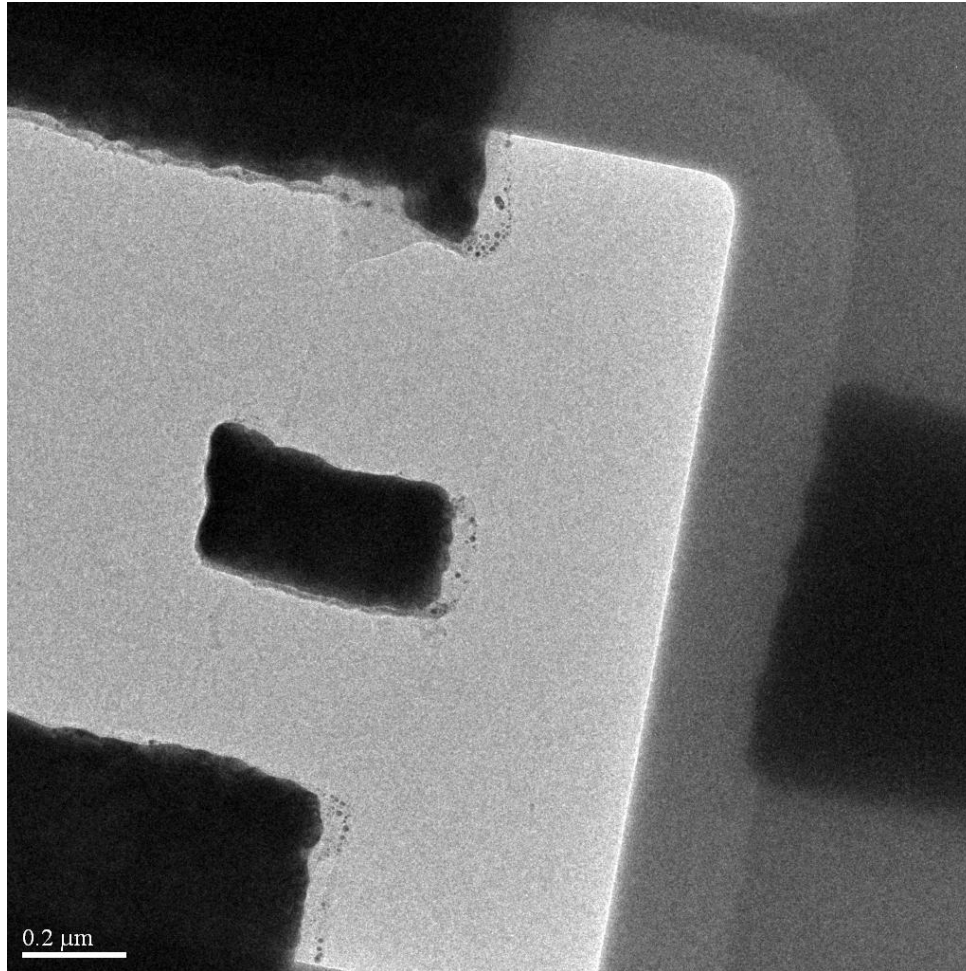
Figure 3.3.7 TEM image of a finished device with one fully suspended CNT and a pedal on it.

3.5 Design and Construction of a Customized Transmission Electron Microscope Specimen Holder

In order to input electric signals into the device in TEM, the TEM specimen holder has to have feedthrough electric probes. The most common specimen holders are the single tilt and double tilt holders, in which samples can be rotated by a single axis and

two axes, respectively. A customized holder was designed and constructed in this study in order to adapt the size of my devices shown in Fig. 3.3.3.

The specimen holder consists of 4 major parts: (i) shaft, (ii) device stage, (iii) head feedthrough and (iv) tail feedthrough, as illustrated in Fig. 3.4.1. The shaft is very similar to the normal single tilt TEM holder and most dimensions are measured from the JEOL JEM 2010F single tilt sample holder. It is made from aluminum for convenience and weight consideration. The two grooves on the shaft marked in Fig. 3.4.1 are fabricated for o-rings, which are used to seal the vacuum. The two ends of the holder shaft are designed to fit the head feedthrough and the tail feedthrough.

The tail feedthrough feeds 8 electric wires into the specimen holder from atmosphere. The commercial 8 Pins- Del Seal CF electrical feedthrough purchased from MDC Vacuum Products Corporation is used here as shown in Fig. 3.4.2. It is attached to the end of the holder shaft by vacuum glue. It can be removed from the holder shaft by heating the holder at 200 ℃ for 1 hour if needed.

The head feedthrough is used to connect the 8 electric wires sealed inside the holder shaft to the 8 electrical probes on the sample stage as illustrated in Fig. 3.4.3. It is inserted into the head of the holder shaft and fixed by two screws (size 0-80). Eight holes are drilled through the feedthrough and 8 metal pins are inserted, serving as electrical connectors between the wires inside the holder and the probes on the sample stage. The whole feedthrough coated with alumina by anode oxidation and it is electrically insulating to the eight pin leads. Vacuum glue is applied on the sealing grooves on both ends to seal the apertures between the pins and the holes.

The 8 electrical probes attached to the grooves on the sample stage (illustrated in Fig. 3.4.4) by vacuum glue are made by phosphor bronze because the material is elastic and has a low Hooke constant. When the sample is pushed onto the 8 pins, the end of the probes will be bent down like a spring and secure good contacts between the pins and the electrodes. The other ends of the probes are connected to the head feedthrough by electrical wires.

device stage

head feedthrough

grooves for O-rings

shaft
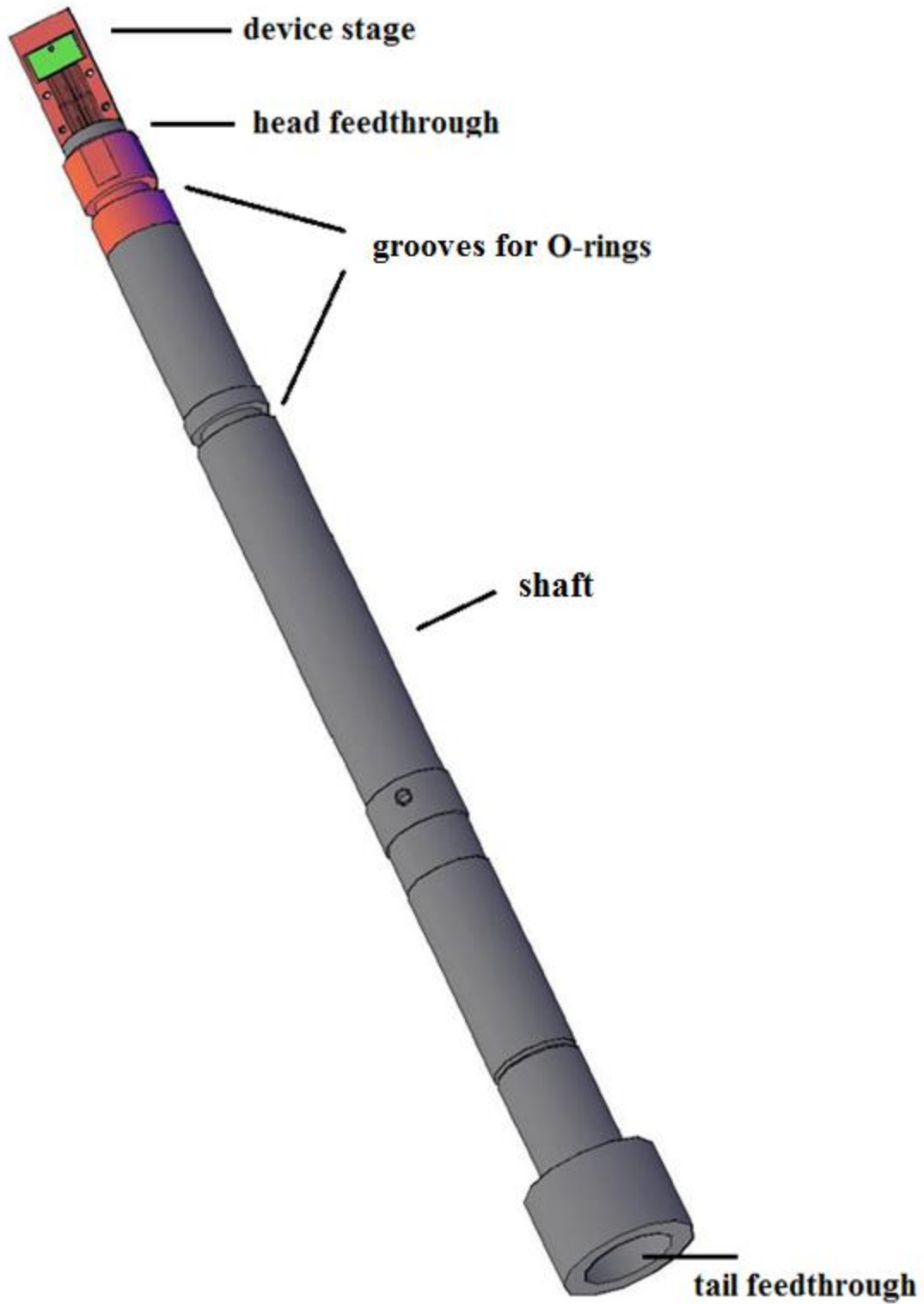
tail feedthrough

Figure 3.4.1 Schematic of the home built TEM holder. It consists of 4 parts: device stage, head feedthrough, tail feedthrough and shaft.

Figure 3.4.2 Picture of the commercial feedthrough purchased from MDC Vacuum Products Corporation. It is attached to the end of the TEM holder shaft, connecting the 8 electrical wires inside the holder to the power supply outside the TEM.
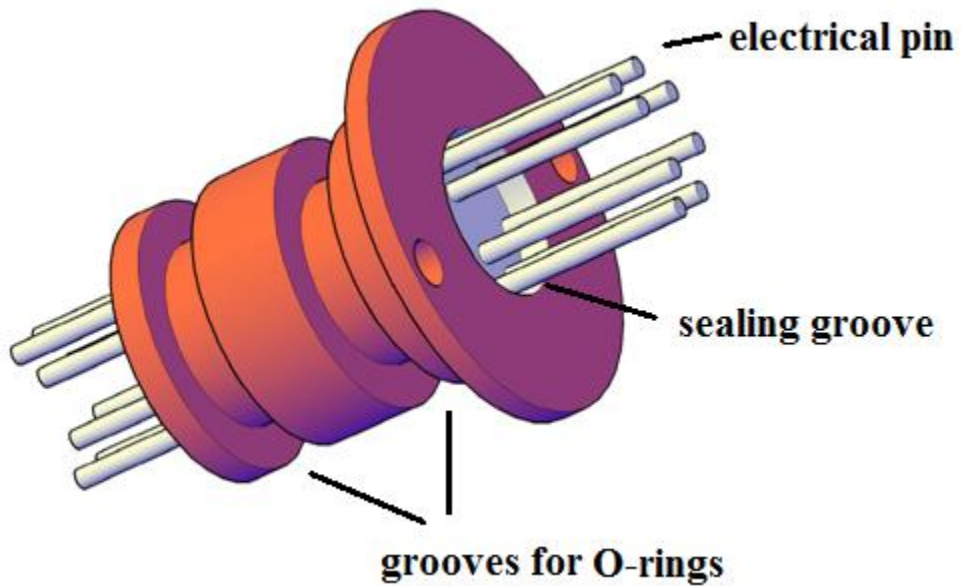
Figure 3.4.3 Schematic of head feedthrough. The two grooves are for o-rings to seal the air inside the holder shaft. The length of an electrical pin is about 2 cm.
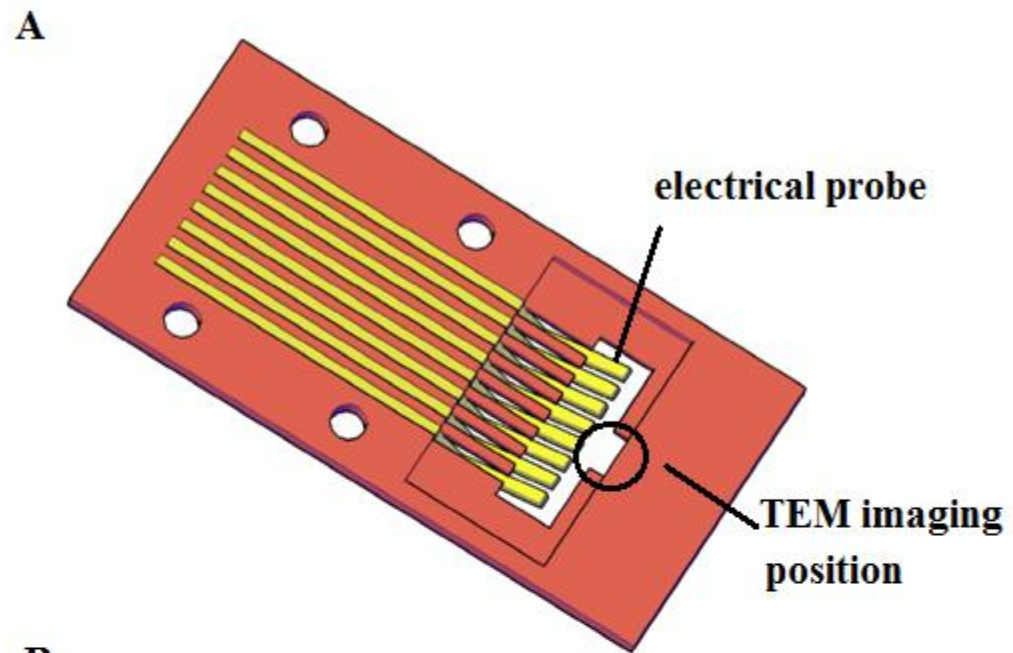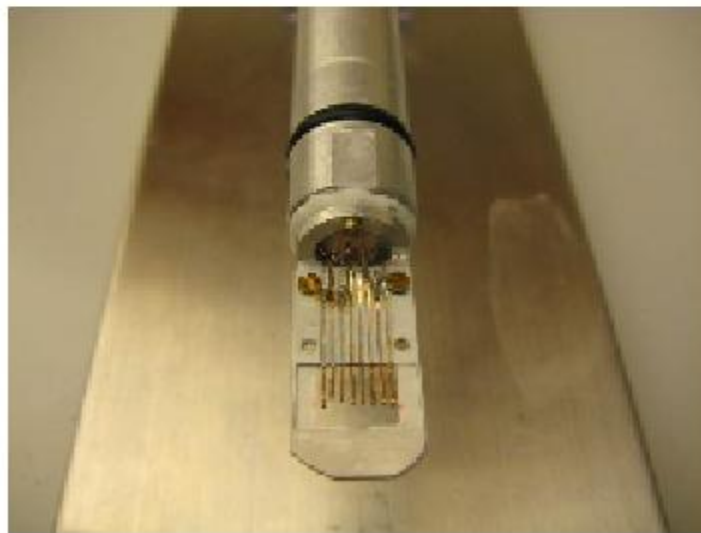
Figure 3.4.4 (A) Schematic of the sample stage. (B) Optical image of the TEM sample stage.

3.6 References

[1]   Iijima, S., Helical Microtubules of Graphitic Carbon. *Nature* **354**, 56-58 (1991).

[2]   Ebbesen, T. W. & Ajayan, P. M., Large-Scale Synthesis of Carbon Nanotubes. *Nature* **358**, 220-222 (1992).

[3]   Journet, C., Maser, W. K., Bernier, P., Loiseau, A., delaChapelle, M. L., Lefrant, S., Deniard, P., Lee, R. & Fischer, J. E., Large-Scale Production of Single-Walled Carbon Nanotubes by the Electric-Arc Technique. *Nature* **388**, 756-758 (1997).

[4]   Wang, X. K., Lin, X. W., Dravid, V. P., Ketterson, J. B. & Chang, R. P. H., Carbon Nanotubes Synthesized in a Hydrogen Arc-Discharge. *Appl. Phys. Lett.* **66**, 2430-2432 (1995).

[5]   Zhao, X., Ohkohchi, M., Wang, M., Iijima, S., Ichihashi, T. & Ando, Y., Preparation of High-Grade Carbon Nanotubes by Hydrogen Arc Discharge. *Carbon* **35**, 775-781 (1997).

[6]   Thess, A., Lee, R., Nikolaev, P., Dai, H. J., Petit, P., Robert, J., Xu, C. H., Lee, Y. H., Kim, S. G., Rinzler, A. G., Colbert, D. T., Scuseria, G. E., Tomanek, D., Fischer, J. E. & Smalley, R. E., Crystalline Ropes of Metallic Carbon Nanotubes. *Science* **273**, 483-487 (1996).

[7]   Kataura, H., Kumazawa, Y., Maniwa, Y., Ohtsuka, Y., Sen, R., Suzuki, S. & Achiba, Y., Diameter Control of Single-Walled Carbon Nanotubes. *Carbon* **38**, 1691-1697 (2000).

[8]   Guo, T., Nikolaev, P., Thess, A., Colbert, D. T. & Smalley, R. E., Catalytic Growth of Single-Walled Nanotubes by Laser Vaporization. *Chem. Phys. Lett.* **243**, 49-54 (1995).

[9]   Qin, L.-C. & Iijima, S., Structure and Formation of Raft-Like Bundles of Single-Walled Helical Carbon Nanotubes Produced by Laser Evaporation. *Chem. Phys. Lett.* **269**, 65-71 (1997).

[10]   Endo, M., Takeuchi, K., Igarashi, S., Kobori, K., Shiraishi, M. & Kroto, H. W., The Production and Structure of Pyrolytic Carbon Nanotubes (Pcnts). *J. Phys. Chem. Solids* **54**, 1841-1848 (1993).

[11]   Li, W. Z., Xie, S. S., Qian, L. X., Chang, B. H., Zou, B. S., Zhou, W. Y., Zhao, R. A. & Wang, G., Large-Scale Synthesis of Aligned Carbon Nanotubes. *Science* **274**, 1701-1703 (1996).

[12]   Qin, L.-C., Cvd Synthesis of Carbon Nanotubes. *J. Mater. Sci. Lett.* **16**, 457-459 (1997).

[13]   Qin, L.-C. & Iijima, S., Fibrilliform Growth of Carbon Nanotubes. *Mater. Lett.* **30**, 311-314 (1997).

[14]   Ren, Z. F., Huang, Z. P., Xu, J. W., Wang, J. H., Bush, P., Siegal, M. P. & Provencio, P. N., Synthesis of Large Arrays of Well-Aligned Carbon Nanotubes on Glass. *Science* **282**, 1105-1107 (1998).

[15]   Kong, J., Soh, H. T., Cassell, A. M., Quate, C. F. & Dai, H. J., Synthesis of Individual Single-Walled Carbon Nanotubes on Patterned Silicon Wafers. *Nature* **395**, 878-881 (1998).

[16]   Fu, Q., Huang, S. M. & Liu, J., Chemical Vapor Depositions of Single-Walled Carbon Nanotubes Catalyzed by Uniform Fe2o3 Nanoclusters Synthesized Using Diblock Copolymer Micelles. *Journal of Physical Chemistry B* **108**, 6124-6129 (2004).

[17]   Ding, L., Zhou, W. W., McNicholas, T. P., Wang, J. Y., Chu, H. B., Li, Y. & Liu, J., Direct Observation of the Strong Interaction between Carbon Nanotubes and Quartz Substrate. *Nano Res.* **2**, 903-910 (2009).

[18]   Qi, H., Qian, C. & Liu, J., Synthesis of Uniform Double-Walled Carbon Nanotubes Using Iron Disilicide as Catalyst. *Nano Lett.* **7**, 2417-2421 (2007).

[19]   Lu, J. Q., Kopley, T. E., Moll, N., Roitman, D., Chamberlin, D., Fu, Q., Liu, J., Russell, T. P., Rider, D. A., Manners, I. & Winnik, M. A., High-Quality Single-Walled Carbon Nanotubes with Small Diameter, Controlled Density, and Ordered Locations Using a Polyferrocenylsilane Block Copolymer Catalyst Precursor. *Chem. Mat.* **17**, 2227-+ (2005).

[20]   Zheng, L. X., O'Connell, M. J., Doorn, S. K., Liao, X. Z., Zhao, Y. H., Akhadov, E. A., Hoffbauer, M. A., Roop, B. J., Jia, Q. X., Dye, R. C., Peterson, D. E., Huang, S. M., Liu, J. & Zhu, Y. T., Ultralong Single-Wall Carbon Nanotubes. *Nat. Mater.* **3**, 673-676 (2004).

[21]   Duesberg, G. S., Burghard, M., Muster, J., Philipp, G. & Roth, S., Separation of Carbon Nanotubes by Size Exclusion Chromatography. *Chem. Commun.*, 435-436 (1998).

[22]   Bandyopadhyaya, R., Nativ-Roth, E., Regev, O. & Yerushalmi-Rozen, R., Stabilization of Individual Carbon Nanotubes in Aqueous Solutions. *Nano Lett.* **2**, 25-28 (2002).

[23]   Li, Y., Liu, J., Wang, Y. Q. & Wang, Z. L., Preparation of Monodispersed Fe-Mo Nanoparticles as the Catalyst for Cvd Synthesis of Carbon Nanotubes. *Chem. Mat.* **13**, 1008-1014 (2001).

[24]   Hall, A. R., Material and Device Investigations on a Carbon Nanotube-Based Torsional Nanoelectromechanical System. PhD Thesis, The University of North Carolina at Chapel Hill, (2007).

Chapter 4

Electrical Resistance of Singe-Wall and Double-Wall Carbon Nanotubes with Determined Chiral Indices

4.1 Introduction

Nanotubes can be metallic and their carrier mobilities are much higher than metals, suggesting that they could be ideal interconnects in nanoelectronic devices. They can also be semiconducting, as controlled by their chiralities, and the intrinsic semiconducting characteristics allow us to build logic devices on the nanometer scale. Furthermore, their mechanical stability and robustness make it possible to fabricate long-lasting devices. Therefore, tremendous theoretical and experimental research on the electrical properties of carbon nanotube has been done to explore this novel one-dimensional material since its discovery 20 years ago [1-10].

A number of molecular simulations and theoretical calculations have been applied to study the band gaps of semiconducting CNTs. In 1995, a precise expression between nanotube's chirality and its energy gap was given by Yorikawa and Muramatsu [11]. This expression includes the effect of mixing between the π and the σ orbitals due to the

curvature of CNT and thus gives a precise description of the band gap based on the tight-binding approximation. Starting from graphene, the band gap consists of two parts in their model: one is independent of the nanotube helical angle donated by E_0; another is dependent on helical angle α donated by E_α. The energy gap can be written as [11]

$$E_g = E_0 + E_\alpha. \tag{4.1.1}$$

If the curvature is neglected, the energy gap given by Eqn. 4.1.1 will reduce to that of a two-dimensional graphene sheet. In the π-electron model,

$$E_0 = \left|V_{pp\pi}\right| / R_d, \tag{4.1.2}$$

where $V_{pp\pi}$ is the tight-binding parameter for π orbital, R_d is the tube radius divided by the carbon-carbon atom distance $d_0 = 0.142$ nm and E_α has the form

$$E_\alpha = \sum_{n \geq 2} (-1)^{p(n-1)} f_n(\alpha) / R_d^n, \tag{4.1.3}$$

whose the leading term is $(-1)^p |V_{pp\pi}| \gamma \cos(3\alpha) / R_d^2$, and where γ is a constant factor having value of 1/12 and p is the reminder of $|u - v|/3$. But when the curvature of tube causes a mixing of the π and σ orbitals, $V_{pp\pi}$ in E_0 and E_α should be modified with a coefficient related to nanotube's radius and γ should take a value different from 1/12.

In their calculation, Yorikawa and Muramatsu constructed an 8×8 Hamiltonian matrix $H(k)$ with a wave vector k and included the $2s$ and $2p$ orbitals to take into the account of mixing of the π and σ orbitals. The matrix elements are given as a function of R_d and the helical angle and contain 5 tight-binding parameters, $V_{pp\pi}$, $V_{pp\sigma}$, $V_{sp\sigma}$, $V_{ss\sigma}$ and $\Delta\varepsilon = (\varepsilon_s - \varepsilon_p)$. Each primitive cell of the carbon nanotube has two independent atoms, A and B, and $H(k)$ has the following form:

$$H_{A_iA_j}(k) = H_{B_iB_j}(k) = \varepsilon_i \delta_j, \tag{4.1.4}$$

$$H_{A_iB_j}(k) = \sum_{l=1,2,3} h_{ij}^l \exp[ik \cdot (r_l - r_A)], \tag{4.1.5}$$

and

$$H_{B_iA_j} = \sum_{l'=1,2,3} h_{ij}^{l'} \exp[ik \cdot (r_{l'} - r_B)], \tag{4.1.6}$$

where i or j is a suffix for the basic states of π and σ orbitals, r_A and r_B are the positional vectors for atoms A and B, r_l and $r_{l'}$ are the positional vectors for the nearest neighbors, and h_{ij}^l and $h_{ij}^{l'}$ contain the five tight-binding parameters $V_{pp\pi}$, $V_{pp\sigma}$, $V_{sp\sigma}$, $V_{ss\sigma}$ and $\Delta\varepsilon = (\varepsilon_s - \varepsilon_p)$. After solving the matrix, the expression of band gap is given as

$$E_g = \eta(R_d) \frac{|V_{pp\pi}|}{R_d} [1 + (-1)^p \gamma \frac{\cos(3\alpha)}{R_d}], \tag{4.1.7}$$

where $|V_{pp\pi}| = 2.24$ eV, $\gamma = 0.4$ and $\eta = 1 - 0.4/R_d^2$ for Tomanek and Schluter parameters and $|V_{pp\pi}| = 2.77$ eV, $\gamma = 0.25$ and $\eta = 1 - 0.3/R_d^2$ for Mintmire, Robertson and White parameters [12, 13].

Experimental measurements on the atomic structure and electronic properties of single-wall carbon nanotubes followed quickly by Odom *et al.* at Harvard University [14] and Wildoer *et al.* at Delft University of Technology [15] in 1998. STM was used to characterize the atomic structure of a single carbon nanotube which was deposited on a Au (1,1,1) surface. The chiral indices were determined from the tube diameter and the angle between the tube axis T and the direction of nearest-neighbor hexagon rows H, as shown in Fig. 4.1.1. Meanwhile, I-V curves of the nanotube were measured via a bias voltage between the STM tip and the Au substrate. Fig. 4.1.2b gives the calculated

normalized conductance and the measured I-V curves from the positions on the nanotube

indicated by the symbols in Fig. 4.1.2a, from which the nanotube's chiral indices were

determined to be (14, 3) (helical angle $11.2°±0.5°$ and diameter $0.95±0.05$ nm). The

calculated $(V/I)dI/dV$ showed two sharp increases at -325 and 425 mV that correspond

to the valence and conduction band edges in the local density of states. Thus, the energy

gap can be assigned to be 750 mV. Their results show that the energy gap has a 1/r

dependence, and can be fitted to $E_g = V_{pp\pi} a_{c-c} / r$, where $V_{pp\pi} = 2.45$ eV is the carbon-

carbon tight-binding overlap energy, a_{c-c} is the carbon-carbon bond distance and r is the

tube radius.

In an STM experiment, the I-V curves were measured between the STM tip and

the underlying gold substrate instead of the two ends of a nanotube. Two terminal

electrical transport measurements on a single nanotube with ohmic contact to the metal

probes were reported by Dai's research group in 1999 [16, 17]. In their experiment, metal

probes (15 nm Ti followed by 70 nm Au) were patterned onto the two ends of an

individual single-wall carbon nanotube which was deposited on the SiO_2 surface by

chemical vapor deposition. Electrical transport properties of the nanotube were

characterized by the I-V curves measured on the metal probes at room temperature and 4

K, respectively. Fig. 4.1.3 shows the I-V curves of a semiconducting SWNT measured at

different gate voltages (V_g) at room temperature. The linear relation at $V_g = 0$ indicates

that the semiconducting SWNT has a constant electrical resistance at low bias voltage at

room temperature. The inset is the I-V curve of the SWNT at 4 K without gate voltage.

The sharp increase at both sides of voltage indicates that the nanotube has a band gap of

0.8 eV. On the contrary, the I-V curve shown in Fig. 4.1.4 is linear and indicates the

nanotube is a metallic SWNT. The inset is the electrical resistance as a function of source-drain voltage derived from the I-V curve.
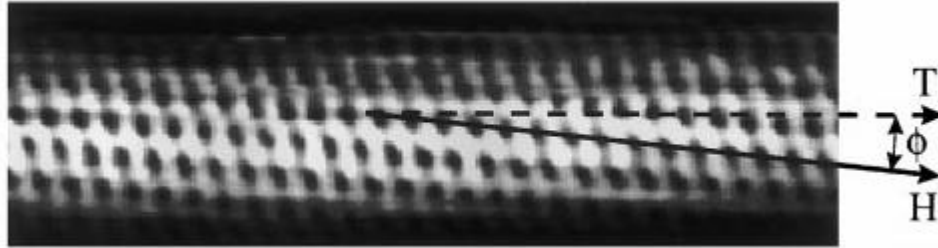
Figure 4.1.1 Atomically resolved STM image of individual single-walled carbon nanotube on the Au (1,1,1) surface. The dashed arrow indicates the tubes axis T and the solid arrow indicates the direction of the nearest-neighbor hexagon rows H. The angle between T and H is the helical angle of $7°$ (chiral indices (11, 7) and diameter 1.2 nm). Image adapted from [15].

Later on, many modifications [18-21], such as side gates and contacting metals, were made on this circuit design to improve the measurement and a much better picture of nanotubes' electrical properties has been obtained. However, the determination of the nanotube's chiral structure is impossible in this kind of experiment. It would be desirable from both a scientific and technological point of view to measure the electrical transport properties and the chiral indices simultaneously. STM, as we mention above, has the capability to measure the chiral structure and band gap of a nanotube, but its application is only limited to the SWNTs of small diameter because of the morphological deformation caused between the substrate and SWNTs [22, 23]. Furthermore, the I-V curves in STM experiment were measured between STM tip and the underlying gold substrate and thus, did not directly represent the electrical transport properties along the tubule axis.

One way to achieve this goal is to make CNT based two-terminal electrical circuits applicable to *in situ* TEM imaging and electron diffraction. This requires that the nanotube between the two metal probes be suspended and the substrate beneath the nanotube be etched completely away. Another important advantage of such device geometry is that it is not only applicable to SWNTs but also to MWNTs. This chapter details this new method and the results obtained.
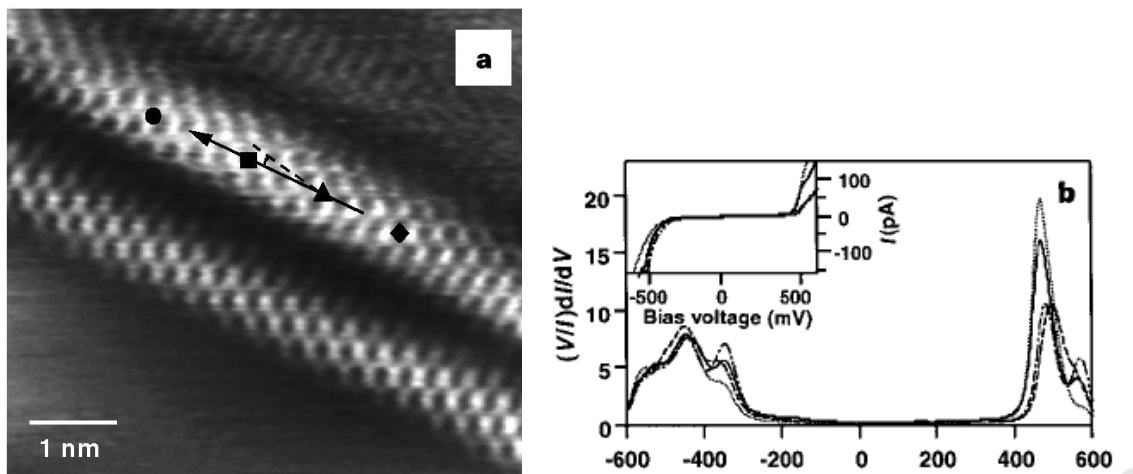
Figure 4.1.2 (a) STM image of an individual single-walled carbon nanotube deposited on the Au (1,1,1) surface. The chiral indices are determined to be (14, 3) (helical angle 11.2 °±0.5 ° and diameter 0.95 ±0.05 nm). (B) Calculated normalized conductance and measured I-V (inset) data from the positions indicated by the symbols in (A). Images adapted from [14].
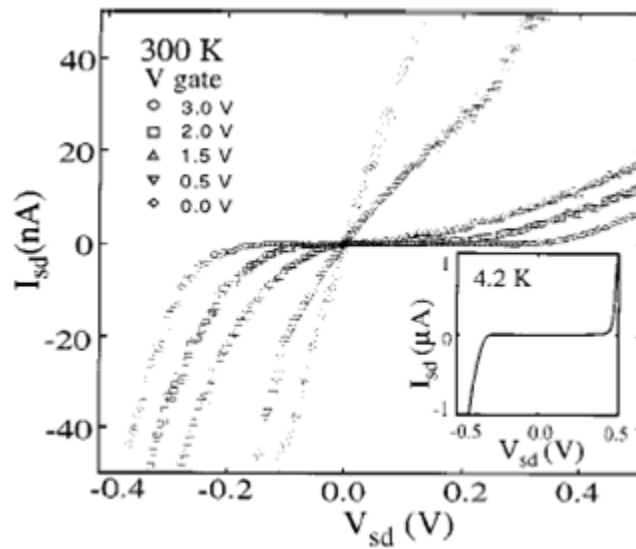
Figure 4.1.3 I-V curves of a semiconducting SWNT measured at different gate voltages at room temperature. Inset is the I-V curve of the same nanotube measured at 4 K with no gate voltage. Image adapted from [16].
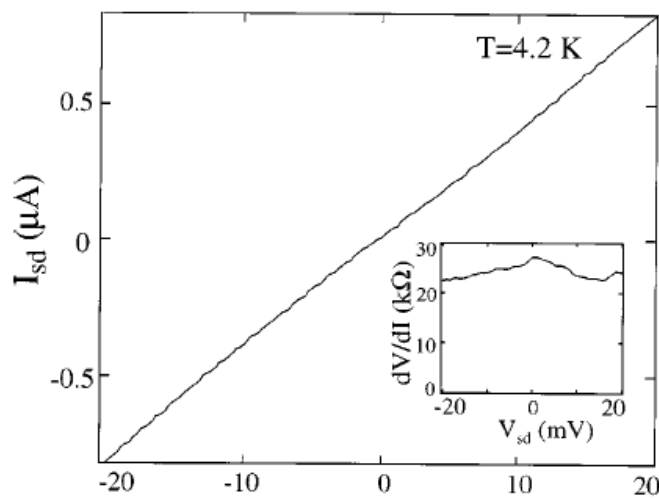
Figure 4.1.4 I-V curve measured on a metallic SWNT at 4.2 K. Inset is the electrical resistance as a function of the source-drain voltage. Image adapted from [16].

4.2 Experimental Method

Electrical leads were deposited onto the nanotube by electron beam lithography in order to measure the I-V curves of the nanotube at room temperature as shown in Fig. 4.2.1(A) (the device fabrication is discussed in Chapter 3). Two types of metals, Au/Cr and Pd, were utilized as the metal electrodes here. Four-probe electrodes consisting of 60 nm Au and 5 nm Cr were patterned on the SWNTs to minimize the effect of Schottky barriers between the nanotubes and metal probes in the I-V measurements. Since Pd has a very good ohmic contact to nanotubes (four probe measurements show that the contact resistances are about a few kΩ, much smaller than those of nanotubes at room temperature) [21], two-probe electrodes of 70 nm Pd were deposited onto the DWNTs. All the electrode leads were earthed first to remove the possible static electric charges before an I-V measurement. After the I-V curves were measured on nanotubes, HNA (a solution mixed with hydrofluoric acid, nitric acid and acetic acid) and focused ion beam (FIB) system were used to etch away the silicon layer and the silicon nitride layer beneath the CNT. The silicon dioxide layer was removed by hydrofluoric acid, leaving a free standing CNT anchored by the metal leads as shown in Fig. 4.2.1(B). The CNT device was then transferred to the TEM (JEOL JEM 2010F operated at 80 kV) for imaging and nano-beam electron diffraction as shown in Fig. 4.2.1(B)-(C). Finally, the chiral indices of the CNT were determined from the electron diffraction patterns and the diameter which was directly measured in the TEM images [24].
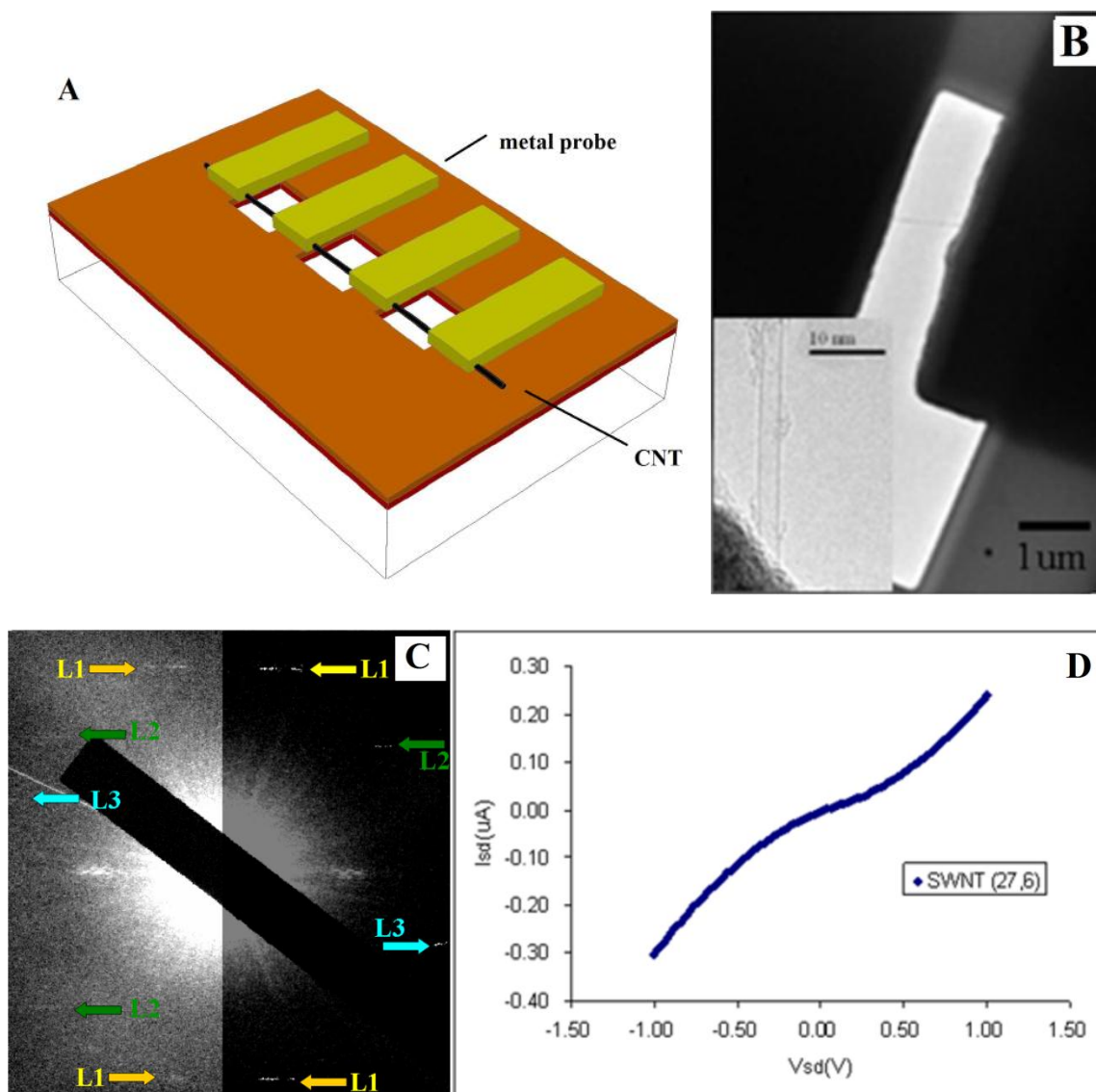
Figure 4.2.1 (A) Schematic of a 4-probe CNT device ready for TEM imaging and electron diffraction. (B) TEM image of the first SWNT listed in Table 4.1. The SWNT was suspended in air and anchored by metal leads (dark area) on the two sides. Inset: A high magnification TEM image of the same SWNT. The scale bar of inset is 10 nm. (C) An electron diffraction pattern of the same SWNT from which the chiral indices (27, 6) were derived. L1, L2 and L3 are the principal layer lines. The left half of the image is the original electron diffraction pattern of the SWNT. The signal-to-noise ratio of the right half was enhanced by adjusting the contrast and brightness. (D) I-V curve of the SWNT measured at room temperature. The non-linearity of the I-V curve and the high resistance indicate large Schottky barriers between the SWNT and the metal leads in the device.

4.3 Results and Discussion

Eight individual SWNTs, four semiconducting SWNTs and four metallic SWNTs, and two DWNTs have been measured in our experiment. The chiral indices (u, v), metallicity, electrical resistance, nanotube length, nanotube diameter, and calculated electronic band gap E_g [4], electrical resistivity are listed in Table 4.1.

The chiral indices of the first nanotube, (27, 6), determined by the ratio of the principal diffraction line spacings in combination with a measurement of the nanotube diameter from the TEM image [24], satisfy the condition $p=0$, , where p is the reminder of $|u - v|/3$ [2]. It is therefore a metallic CNT. However, its I-V curve measured at room temperature (300 K) has an obvious non-linearity and a resistance of about 3 MΩ. This resistance is much larger than the quantum-limit resistance expected for the ballistic SWNT ($R_0 = \dfrac{h}{4e^2} \approx 6.5$ kΩ , quantum-limit conductance $G_0 = 1/R_0$) [25, 26] and it actually resulted from the Schottky barriers in the poor contacts between the metal leads and the SWNT [27]. An annealing process was used in our experiment to improve the contact between the gold metal lead and the SWNT [28]. A four-probe method was used to minimize the effects from the contact resistances. In the measurement of the latter seven SWNTs, the contact resistances are in the range of 3-5 kΩ (~5% of the SWNT resistance) measured by the four-probe method.

No.	Type	(u,v)	Metallicity	Resistance (kΩ)	Diameter (nm)	Length (μm)	Eg(eV)	Resistivity (kΩ/μm)	Estimated Resistivity (kΩ/μm)
1	SWNT	(27,6)	metallic	~3000	2.39	1.00	0.000	~3000	n/a
2	SWNT	(46,16)	metallic	56	4.36	0.90	0.000	62	n/a
3	SWNT	(40,7)	metallic	25	3.44	0.57	0.000	44	n/a
4	SWNT	(22,13)	metallic	30	2.40	0.60	0.000	46	n/a
5	SWNT	(44,24)	semiconducting	86	4.67	0.70	0.137	122	95
6	SWNT	(48,7)	semiconducting	85	4.06	0.61	0.160	139	149
7	SWNT	(38,21)	semiconducting	80	4.05	0.62	0.158	129	143
8	SWNT	(33,16)	semiconducting	156	3.39	0.62	0.191	252	254
9	DWNT	(40,12)	semiconducting	90	3.69	0.62	0.167	163	172
		(28,15)	semiconducting		2.96		0.218		460
10	DWNT	(54,11)	semiconducting	60	4.72	0.53	0.131	95	85
		(47,8)	metallic		4.03		0.000		n/a

Table 4.1 Chiral indices (*u*,*v*), metallicity, electrical resistance, nanotube diameter, nanotube length, resistivity of the 8 SWNTs and 2 DWNTs measured in our experiment. Column 8 lists the electronic band gaps of the nanotubes calculated by the method reported by Yorikawa and Muramatsu [11] using Tomanek and Schluters' parameters [12]. The last column is the resistivity estimated by Eqn. 4.3.2.
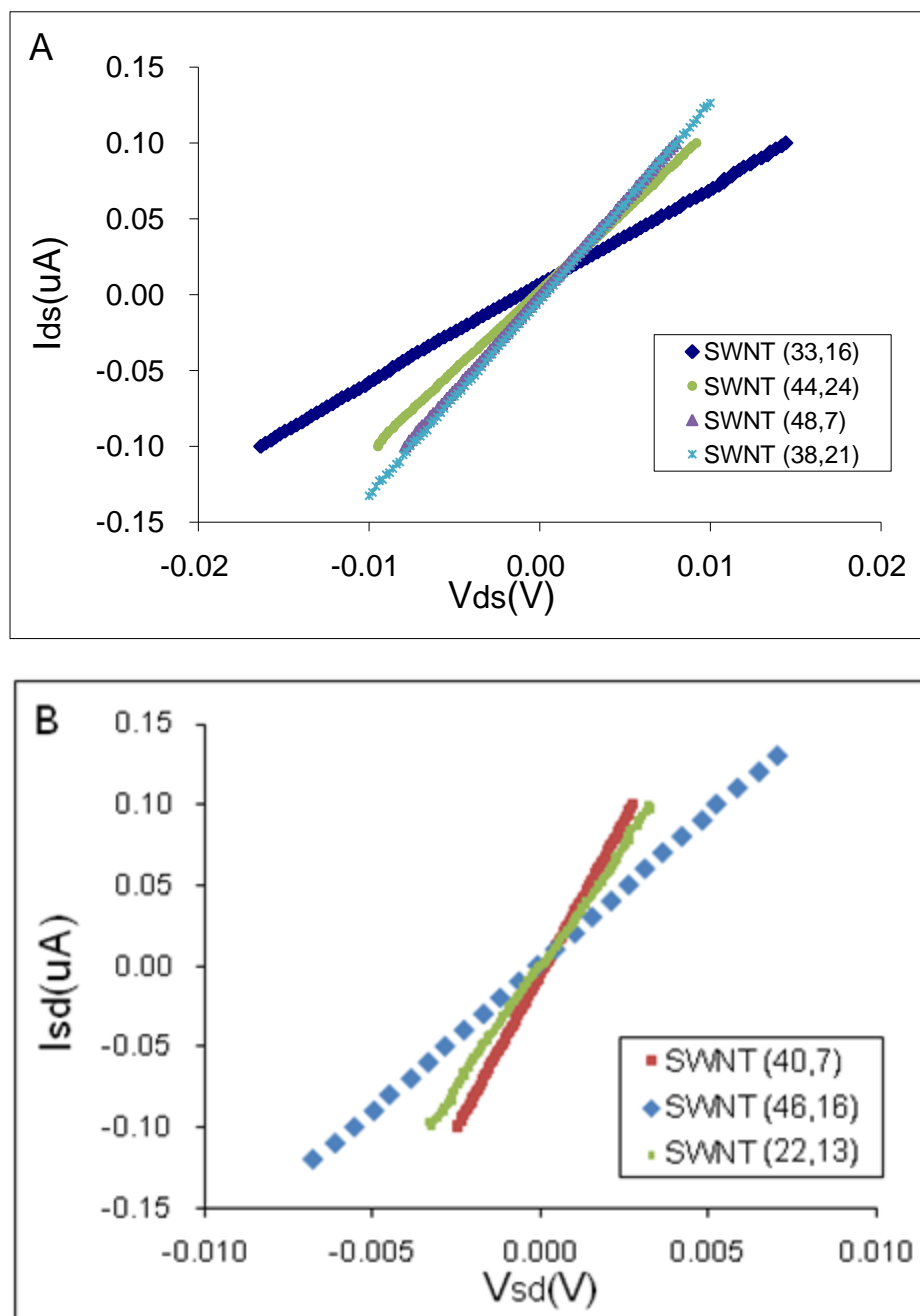
Figure 4.3.2. (A) I-V curves for the four semiconducting SWNTs (no. 5, 6, 7 and 8) measured by 4-probe method at room temperature. (B) I-V curves for the metallic SWNTs (no. 2, 3 and 4) measured by 4-probe method at room temperature.

The second, third and fourth metallic SWNT listed in Table 4.1 have resistances of 56 kΩ, 25 kΩ and 30 kΩ at room temperature (300 K), as measured from their I-V curves shown in Fig. 4.2.2(A). For a metallic SWNT, acoustic phonon scattering is the main factor which determines the resistance at low bias [29, 30]. The resistance in a metallic SWNT due to this factor can be expressed as

$$R_{ap}(T) = \frac{h}{4e^2} \frac{L}{L_{ap}(T)},$$

(4.3.1)

where h is the Planck's constant, e is the electric charge of electron, L is the length of the SWNT between two metal leads and L_{ap} is the mean free path (mfp) for acoustic phonon scattering, which is a function of temperature of T and increases with increasing temperature [21]. From the measured electrical resistance, it provides a rough estimation of L_{ap} to be about 120 nm, 148 nm and 130 nm for these three metallic SWNTs at 300 K.

An SEM image of the 4-probe metal leads on the 7th SWNT in Table 4.1 is shown in Fig. 4.3.3(A). The chiral indices determined from the electron diffraction pattern in Fig. 4.3.3(B) are (38, 21) which satisfy the semiconducting SWNT condition that $|u - v| = 3g + 2$ [2], where g is an integer. Similar to the metallic SWNT, the four semiconducting SWNTs in Table 4.1 exhibit a linear I-V relationship as shown in Fig. 4.3.2(A) and the resistances are about 100 kΩ. The amorphous material around the SWNT shown in Fig. 4.3.3(C) is amorphous carbon deposited onto the nanotube during long exposure.

As expected, the resistivity of SWNT increases with the band gap for a semiconducting SWNT. We can make an estimate of the electrical resistivity at room temperature based on the band gap of a nanotube. The static electric charges on the

nanotube are removed via grounding of all the electrodes before I-V measurement. The low bias voltage (about 10 mV) which is much smaller than the energy gap of a nanotube (around 100 mV) is insufficient to induce the tunneling between the conduction band and the covalence band. Therefore, the electronic transport carriers of a semiconducting SWNT at room temperature mainly come from the electrons which are thermally excited from the valance band into the conduction band. At a fixed temperature, the density of charge carriers is a constant in a semiconducting SWNT. Therefore, it gives a linear relationship in the I-V curves.
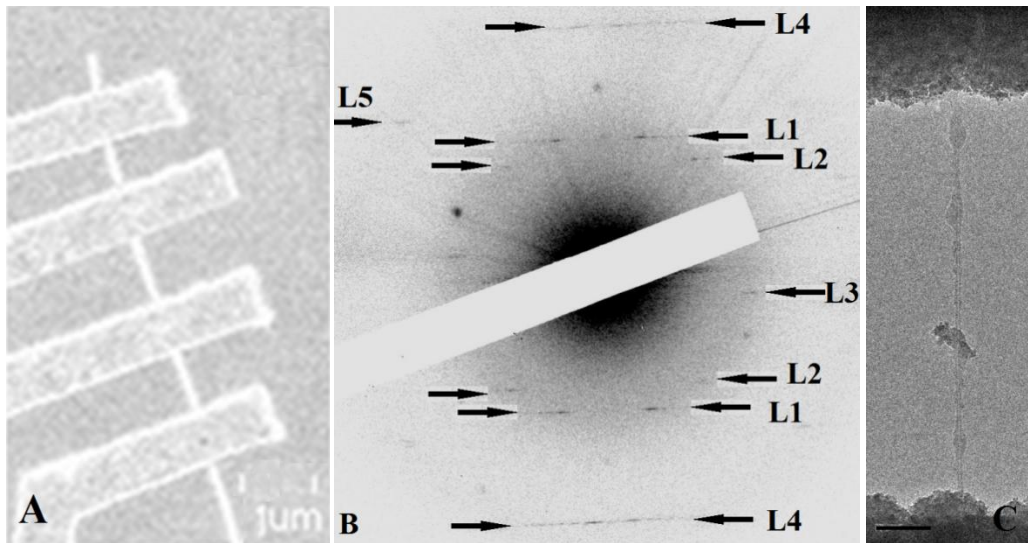
Figure 4.3.3 (A) SEM image of the 4 metal (Au/Cr) leads on the 7th SWNT given in Table 4.1 produced by electron beam-lithography. The I-V curve of the SWNT is measured by these 4 probes. (B) Electron diffraction pattern of the same SWNT. L1, L2, L3, L4, and L5 are the principal layer lines from this SWNT. The chiral indices were determined to be (38, 21) from the diffraction pattern. The image is inverted to negative contrast for clarity. (C) TEM image of the SWNT. Scale bar, 50 nm.

The possibility for an electron being excited to the conduction band is proportional to $\exp(-\dfrac{E_g}{k_B T})$, where E_g is the band gap and k_B is the Boltzmann constant.

The carrier (electrons) density is proportional to $\exp(-\frac{E_g}{2k_BT})$. The conductance is proportional to the same factor. The lengths of the four semiconducting SWNTs are around 0.5-1 μm which are smaller than $L_{ap} = 4 \times 10^5 D/T$ [31], where D is the nanotube diameter in nm and T is the absolute temperature. Hence phonon scattering may have only a small effect on the resistances. The resistivity of a semiconducting SWNT at room temperature can then be estimated by

$$R = \frac{h}{4e^2}\exp(\frac{E_g}{2k_BT}). \tag{4.3.2}$$

The estimation of the resistivity is listed in the last column of Table 4.1. The 8th SWNT (33, 16) is 254 kΩ, in excellent agreement with the experimentally measured resistance normalized by its length (251 kΩ) as shown in Table 4.1. The numerical estimation of the resistivities on the rest semiconducting SWNTs is also very close to (about 10%-13% off) the measured resistivities.

Other factors may also contribute to the electrical resistance of a carbon nanotube such as morphological deformation. SWNTs show a dramatic band gap dependence on their deformation such as uniaxial and/or torsional deformation [2, 22, 32-34]. In our experiment, the SWNTs might be under stress at the interface between the substrate surface and the nanotube and therefore have some deformation. The decrease on the band gap caused by the deformation would decrease the electrical resistance.

Two DWNTs were measured in devices 9 and 10 as listed in Table 4.1. From the diffraction pattern and direct TEM imaging, Fig. 4.3.4(A)-(B), we derived that the DWNT in device 9 has the chiral indices of (40, 12) and (28, 15) which has a semiconducting-semiconducting shell combination. DWNT in device 10 has the chiral

indices of (54, 11) and (47, 8) which has a semiconducting-metallic shell combination. The room temperature resistivities of the two DWNTs derived from the I-V curves, Fig. 4.3.5, are very close to (about 10% off) the estimated resistivities (see Table 4.1) calculated from the band gaps of outer-shells, but are far away from the estimated resistivities of inner-shells. For the DWNT device 9, the estimated resistivity of the inner shell is about 200% larger than the experimental values. If the shells were parallel in the electrical transport, the total resistance would be 120 kΩ and about 30% smaller than the experimental value. For the DWNT device 10, the total resistance of the parallel transport is 31 kΩ if the average resistivity of the metallic SWNT device 2, 3 and 4 is used as that of the inner shell. It is about 70% smaller than the experimental value. Therefore, I conclude that electrons only transport along the outer-shell of a DWNT in a metal-on-top mode circuits, even though the nanotubes are buried beneath the metal electrodes. One very possible reason is that the metal probes only has good contact to the outer-shell and the coupling between the two shells is very weak due to the weak van der Waals interaction [35, 36].
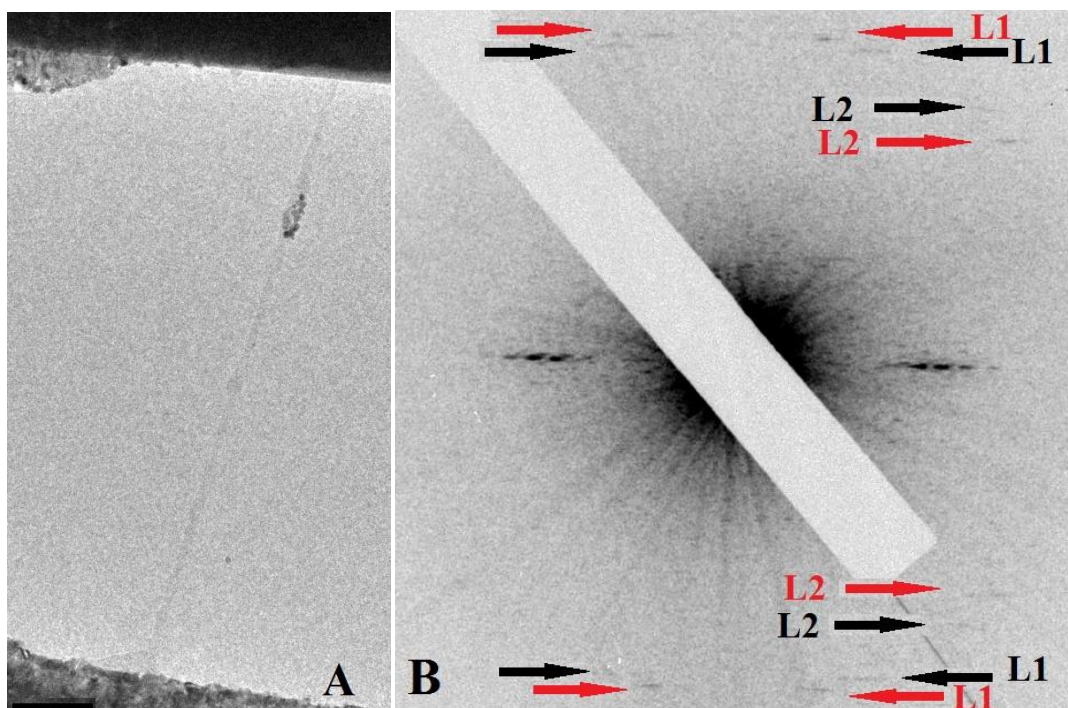
Figure 4.3.4 (A) TEM image of the DWNT in device 9 listed in Table 4.1. The DWNT was suspended in air and anchored by metal leads (dark area) on the two sides. The amorphous material around the nanotube is carbon deposited onto the nanotube during long exposure. The scale bar is 50 nm. (B) An electron diffraction pattern of the same DWNT from which the chiral indices (40, 12) and (28, 15) were derived. Principal layer lines L1 and L2 marked by red and black arrows are coming from the outer-shell and inner-shell, respectively.
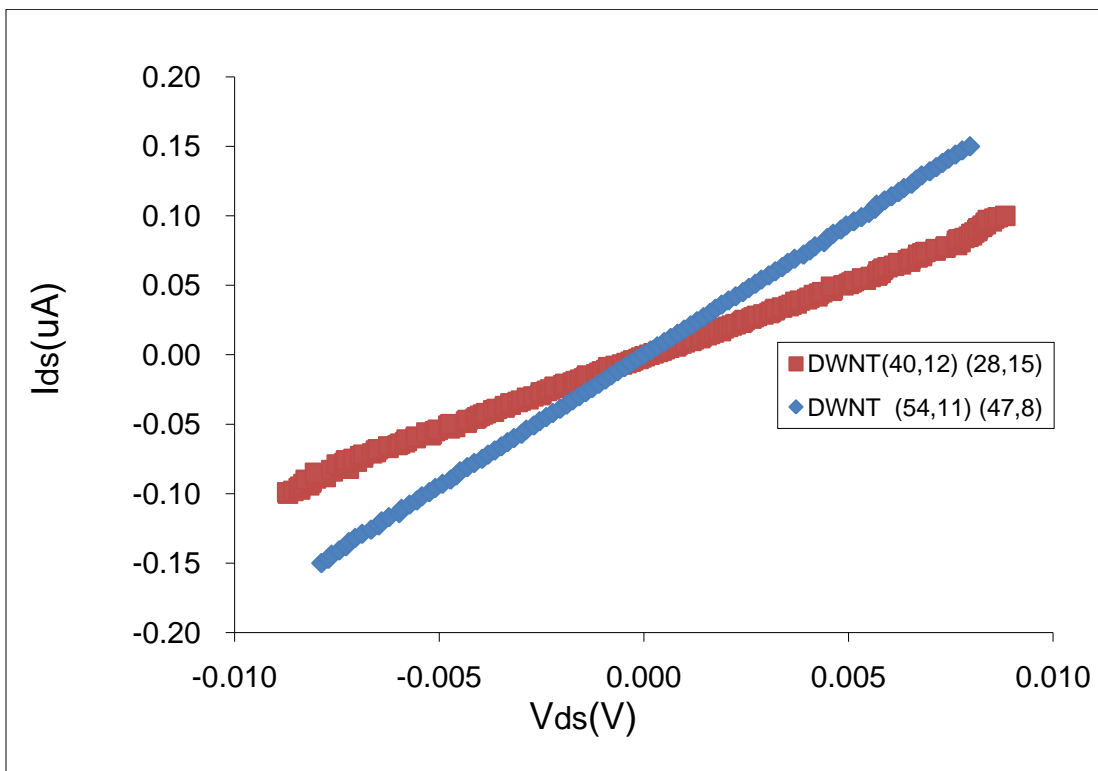
Figure 4.3.5 I-V curve for the DWNTs in device 9 and 10 measured by 2-probe method at room temperature.

4.4 References

[1]   Charlier, J. C., Blase, X. & Roche, S., Electronic and Transport Properties of Nanotubes. *Rev. Mod. Phys.* **79**, 677-732 (2007).

[2]   Anantram, M. P. & Leonard, F., Physics of Carbon Nanotube Electronic Devices. *Rep. Prog. Phys.* **69**, 507-561 (2006).

[3]   Jones, D. E. H., Dresselhaus, M. S, Dresselhaus, G, Eklund, P. C, Science of Fullerenes and Carbon Nanotubes. *Nature* **381**, 384-384 (1996).

[4]   Kreupl, F., Graham, A. P., Duesberg, G. S., Steinhogl, W., Liebau, M., Unger, E. & Honlein, W., Carbon Nanotubes in Interconnect Applications. *Microelectron. Eng.* **64**, 399-408 (2002).

[5]   Ngo, Q., Petranovic, D., Krishnan, S., Cassell, A. M., Ye, Q., Li, J., Meyyappan, M. & Yang, C. Y., Electron Transport through Metal-Multiwall Carbon Nanotube Interfaces. *IEEE Trans. Nanotechnol.* **3**, 311-317 (2004).

[6]   Wei, B. Q., Vajtai, R. & Ajayan, P. M., Reliability and Current Carrying Capacity of Carbon Nanotubes. *Appl. Phys. Lett.* **79**, 1172-1174 (2001).

[7]   Appenzeller, J., Knoch, J., Martel, R., Derycke, V., Wind, S. J. & Avouris, P., Carbon Nanotube Electronics. *IEEE Trans. Nanotechnol.* **1**, 184-189 (2002).

[8]   Kong, J., Yenilmez, E., Tombler, T. W., Kim, W., Dai, H. J., Laughlin, R. B., Liu, L., Jayanthi, C. S. & Wu, S. Y., Quantum Interference and Ballistic Transmission in Nanotube Electron Waveguides. *Phys. Rev. Lett.* **87** (2001).

[9]   Collins, P. C., Arnold, M. S. & Avouris, P., Engineering Carbon Nanotubes and Nanotube Circuits Using Electrical Breakdown. *Science* **292**, 706-709 (2001).

[10]   Nakanishi, T., Bachtold, A. & Dekker, C., Transport through the Interface between a Semiconducting Carbon Nanotube and a Metal Electrode. *Phys. Rev. B* **66** (2002).

[11]   Yorikawa, H. & Muramatsu, S., Energy Gaps of Semiconducting Nanotubules. *Phys. Rev. B* **52**, 2723-2727 (1995).

[12]   Tomanek, D. & Schluter, M. A., Growth Regimes of Carbon Clusters. *Phys. Rev. Lett.* **67**, 2331-2334 (1991).

[13]   Mintmire, J. W., Robertson, D. H. & White, C. T., Properties of Fullerene Nanotubules. *J. Phys. Chem. Solids* **54**, 1835-1840 (1993).

[14]   Odom, T. W., Huang, J. L., Kim, P. & Lieber, C. M., Atomic Structure and Electronic Properties of Single-Walled Carbon Nanotubes. *Nature* **391**, 62-64 (1998).

[15]   Wildoer, J. W. G., Venema, L. C., Rinzler, A. G., Smalley, R. E. & Dekker, C., Electronic Structure of Atomically Resolved Carbon Nanotubes. *Nature* **391**, 59-62 (1998).

[16]   Soh, H. T., Quate, C. F., Morpurgo, A. F., Marcus, C. M., Kong, J. & Dai, H. J., Integrated Nanotube Circuits: Controlled Growth and Ohmic Contacting of Single-Walled Carbon Nanotubes. *Appl. Phys. Lett.* **75**, 627-629 (1999).

[17]   Kong, J., Zhou, C., Morpurgo, A., Soh, H. T., Quate, C. F., Marcus, C. & Dai, H., Synthesis, Integration, and Electrical Properties of Individual Single-Walled Carbon Nanotubes. *Appl. Phys. A-Mater. Sci. Process.* **69**, 305-308 (1999).

[18]   Zhou, C. W., Kong, J. & Dai, H. J., Electrical Measurements of Individual Semiconducting Single-Walled Carbon Nanotubes of Various Diameters. *Appl. Phys. Lett.* **76**, 1597-1599 (2000).

[19]   Zhou, C. W., Kong, J. & Dai, H. J., Intrinsic Electrical Properties of Individual Single-Walled Carbon Nanotubes with Small Band Gaps. *Phys. Rev. Lett.* **84**, 5604-5607 (2000).

[20]   Franklin, N. R., Wang, Q., Tombler, T. W., Javey, A., Shim, M. & Dai, H. J., Integration of Suspended Carbon Nanotube Arrays into Electronic Devices and Electromechanical Systems. *Appl. Phys. Lett.* **81**, 913-915 (2002).

[21]   Mann, D., Javey, A., Kong, J., Wang, Q. & Dai, H. J., Ballistic Transport in Metallic Nanotubes with Reliable Pd Ohmic Contacts. *Nano Lett.* **3**, 1541-1544 (2003).

[22]   Hertel, T., Walkup, R. E. & Avouris, P., Deformation of Carbon Nanotubes by Surface Van Der Waals Forces. *Phys. Rev. B* **58**, 13870-13873 (1998).

[23]   Wong, E. W., Sheehan, P. E. & Lieber, C. M., Nanobeam Mechanics: Elasticity, Strength, and Toughness of Nanorods and Nanotubes. *Science* **277**, 1971-1975 (1997).

[24]   Qin, L.-C., Electron Diffraction from Carbon Nanotubes. *Rep. Prog. Phys.* **69**, 2761-2821 (2006).

[25]   White, C. T. & Todorov, T. N., Carbon Nanotubes as Long Ballistic Conductors. *Nature* **393**, 240-242 (1998).

[26]   Dekker, C., Carbon Nanotubes as Molecular Quantum Wires. *Phys. Today* **52**, 22-28 (1999).

[27]   Yaish, Y., Park, J. Y., Rosenblatt, S., Sazonova, V., Brink, M. & McEuen, P. L., Electrical Nanoprobing of Semiconducting Carbon Nanotubes Using an Atomic Force Microscope. *Phys. Rev. Lett.* **92** (2004).

[28]   Hall, A. R., Falvo, M. R., Superfine, R. & Washburn, S., Electromechanical Response of Single-Walled Carbon Nanotubes to Torsional Strain in a Self-Contained Device. *Nat. Nanotechnol.* **2**, 413-416 (2007).

[29]   Yao, Z., Kane, C. L. & Dekker, C., High-Field Electrical Transport in Single-Wall Carbon Nanotubes. *Phys. Rev. Lett.* **84**, 2941-2944 (2000).

[30]   Perebeinos, V., Tersoff, J. & Avouris, P., Electron-Phonon Interaction and Transport in Semiconducting Carbon Nanotubes. *Phys. Rev. Lett.* **94** (2005).

[31]   Naeemi, A. & Meindl, J. D., Compact Physical Models for Multiwall Carbon-Nanotube Interconnects. *IEEE Electron Device Lett.* **27**, 338-340 (2006).

[32]   Yang, L., Anantram, M. P., Han, J. & Lu, J. P., Band-Gap Change of Carbon Nanotubes: Effect of Small Uniaxial and Torsional Strain. *Phys. Rev. B* **60**, 13874-13878 (1999).

[33]   Nolting, F., Scholl, A., Stohr, J., Seo, J. W., Fompeyrine, J., Siegwart, H., Locquet, J. P., Anders, S., Luning, J., Fullerton, E. E., Toney, M. F., Scheinfein, M. R. & Padmore, H. A., Direct Observation of the Alignment of Ferromagnetic Spins by Antiferromagnetic Spins. *Nature* **405**, 767-769 (2000).

[34]   Chen, D., Sasaki, T., Tang, J. & Qin, L.-C., Effects of Deformation on the Electronic Structure of a Single-Walled Carbon Nanotube Bundle. *Phys. Rev. B* **77** (2008).

[35]   Lunde, A. M., Flensberg, K. & Jauho, A. P., Intershell Resistance in Multiwall Carbon Nanotubes: A Coulomb Drag Study. *Phys. Rev. B* **71** (2005).

[36]   Stetter, A., Vancea, J. & Back, C. H., Determination of the Intershell Conductance in a Multiwall Carbon Nanotube. *Appl. Phys. Lett.* **93** (2008).

Chapter 5

Direct Measurement of the Friction between Walls of Carbon Nanotubes and Shear Modulus

5.1 Introduction

Besides the rich variety of intriguing electronic properties, carbon nanotubes also exhibit amazing mechanical properties which make them a very attractive candidate for use in nano-electromechanical system (NEMS) devices [1-5]. As discussed in the Chapter 1, mechanical modulus, which is larger than that of diamond, makes CNTs the strongest and most robust material known to man [3, 6]. Furthermore, SWNTs and MWNTs can bear large torsional strains along their tubule direction without plastic deformation or buckling [7-9]. Based on these properties, nano-scale devices which employ a CNT as a torisonal bearing, such as nano-motors and nano-switches [9-14], have been fabricated and tested in many laboratories around the world. Therefore, the knowledge of the shear modulus and the interlayer friction of a CNT is very important in the understanding and design of CNT based nano-electromechanical systems that require a fine control of actuation and friction between nano-scale objects.

A number of investigations have been carried out on the shear modulus of CNTs including a few on the interlayer friction within a MWNT. The first measurement of MWNT's shear modulus was reported by Williams *et al.* in 2002 [15]. A torsional device was fabricated on a MWNT deposited on a silicon substrate with a dioxide layer on the top and the nanotube was then suspended in air by etching the dioxide layer away beneath the nanotube as shown in Fig. 5.1.1. Scanning probe technique with a hybrid AFM/SEM was used to investigate the torsional properties. The measured shear modulus qualitatively agreed with theoretical values of ~0.5 TPa [3, 16]. Later on, the torsional devices were modified into a MWNT and SWNT oscillator for further study on shear modulus [12, 17]. The silicon substrate was made to a back-gate by doping of aluminum. A small AC signal was added to a DC offset on the back-gate to drive the oscillation of metal paddle. An optical interferometer was employed in the SEM to detect and record these deflections. Because the resonance frequency is related to the shear modulus by [12]

$$G = \frac{8\pi^2 \rho L}{r_o^4 - r_i^4} F_0^2 ,$$
(5.1.1)

where G is the CNT shear modulus, ρ is the moment of inertia, L the length of CNT, r_o and r_i are the outer and inner radius, respectively and F_0 is the resonance frequency. Because the inner radius could not be measured in any event and how much interaction would occur between shells was not clear, two limiting models were used to calculate shear modulus: G_e the solid rod model and G_s the thin shell model.

In the solid model, all the shells were assumed to twist as much as the outermost shell just like a solid rod, while only the outermost shell was torqued in the thin shell model. The shear moduli of the MWNTs from 9 devices were calculated based on the

89

above two models. Interestingly, the G_e of 4 MWNTs agreed qualitatively with the experimental values while the G_s of another 4 MWNTs was in agreement. For one device, neither value was close to the experimental value. This indicates that the interaction and relative torisonal motion within a MWNT may vary with the number of shells. Both the solid rod model and the thin shell model are too simplified to explain the interactions between the neighboring layers.
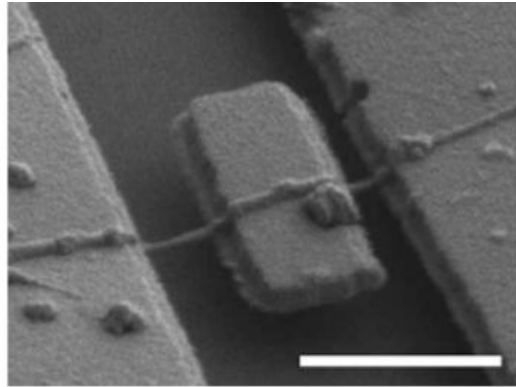
Figure 5.1.1 SEM image of an MWNT torsional device. The MWNT is suspended on the silicon substrate by etching away the dioxide layer beneath the tube. Scale Bar, $1 \, \mu m$. Image adapted from [15].

Torsional devices built on SWNTs were also fabricated to examine this phenomenon for the simplest case [8]. The SWNT pendulum which employed SWNT as a torsional bearing with a metal pad was suspended on the silicon substrate by etching away the dioxide layer beneath the nanotube. The doped silicon substrate was used as a back-gate to actuate the paddle via a bias DC voltage. The deflection of the paddle was measured from the change in the projected length of the paddle in SEM images as shown in Fig. 5.1.2. The torque applied on the paddle from the electrical static force was

calculated from a finite element model with the detailed knowledge of the device geometry. The shear modulus of SWNT was obtained by solving the equation [18]

$$G = \frac{\tau l_1 l_2}{r^3 t \pi \theta (l_1 + l_2)},$$ (5.1.2)

where l_1 and l_2 are the nanotube length to the left and right of the paddle, respectively, r is the radius of the nanotube, θ is the delfection angle and t=0.34 nm is the wall thickness and τ is the net torque. The average value for the SWNT shear modulus of the device was 0.41 $\pm$ 0.36 TPa. No detectable nonlinear response was observed in the experiment. This result indicates that the torsional response is linear in SWNT at least before plastic deformation occurs. However, the torsional response for a DWNT or a few wall carbon nanotube is still to be answered. Meanwhile, the uncertainty of the shear modulus was quite large due to a lack of precise measurement on the radii which cannot be measured by SEM.

The interlayer force was measured in a telescoping motion between the neighboring layers with the least surface resistance within a MWNT [19, 20]. An arc-discharge grown nanotube was glued onto the tip of a sample manipulator in the TEM. Outer layers of the nanotube were removed by electrical breakdown and the exposed core was spot welded to the tip of an AFM as shown in Fig. 5.1.3. When the AFM tip was pulled along the tubule direction, the telescopic motion between the neighboring layers with the least surface resistance would occur via a self-selecting process. Interlayer friction was estimated to be less than 1.4×10^{-15} N/atom measured from the AFM signal. However, the measurement actually gave the minimum estimation on the interlayer friction since the telescopic motion prejudicially slides between the smoothest layers. The

interlayer force among other layers is still unclear. Furthermore, the contact area was constantly shrinking during the telescoping motion and this could also affect the measurement of the interlayer force.
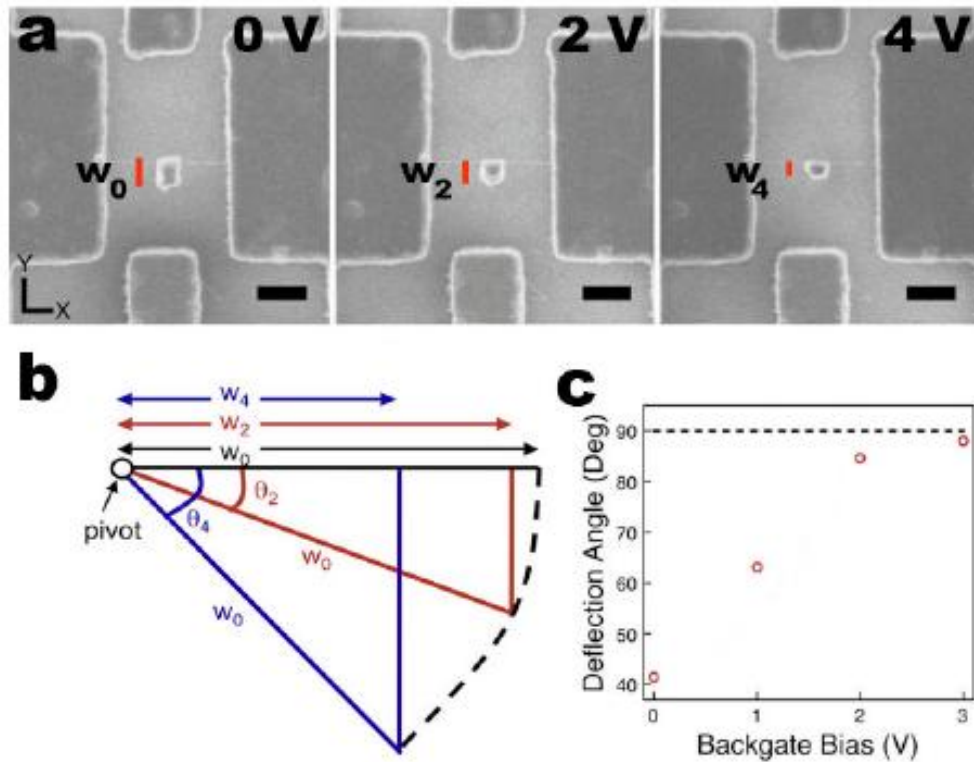
Figure 5.1.2 (a) SEM images of a device from the top view at different back-gate voltage. The width of the paddle is marked by the red line. Scale bar 500 nm. (b) Geometric relation between apparent paddle widths and deflection angles. (c) Applied back-gate voltage vs. measured paddle deflection for a typical device. Dashed lines represent quadratic fit to data and maximum angle attainable with this device (90°). Image adapted from [8].

To answer this question, one way is to start from the simplest case: using a double-wall carbon nanotube (DWNT), to reduce the interlayer interactions to only two layers. This chapter will detail the fabrication of DWNT torional devices applicable for *in*

situ TEM imaging and electron diffraction. The relative torsional motion is applied to study the interlayer interactions while keeping the contact area unchanged. We report the inner shell's torsional response to the shear stress applied to the outer shell. The interlayer friction is inferred from direct measurements of each shell's deformation, van der Waals interactions between shells, and reliable models of lattice strain.
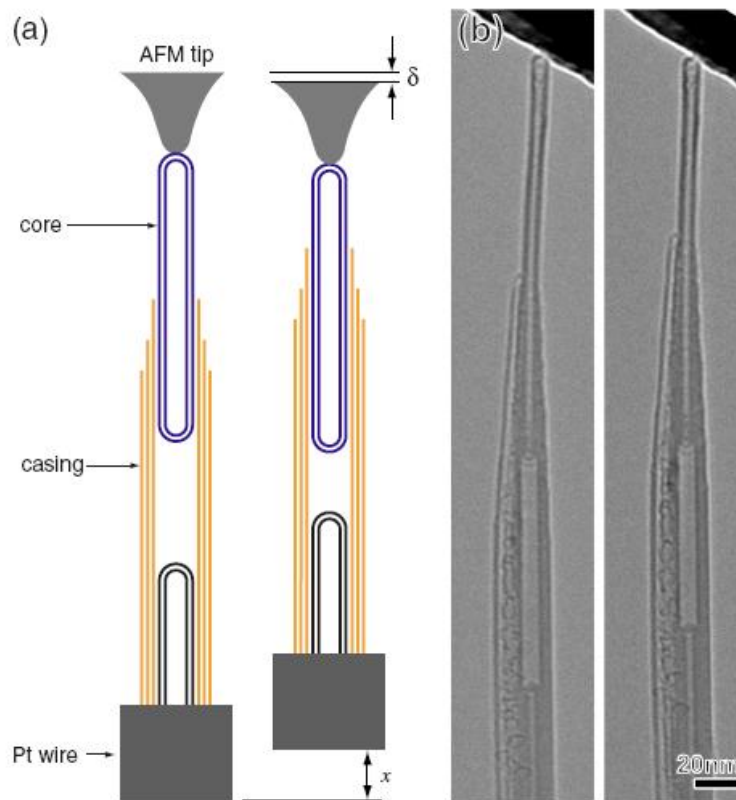
Figure 5.1.3 (a) Schematic drawing of measurement setup. The protruding core of a MWNT is connected to an AFM tip. The outer casing is mechanically connected on the other end to a Pt wire, attached onto a sample manipulator which is used to induce telescoping motion. (b) TEM images of a telescoping MWNT. Figure adapted from [19].

5.2 Experimental Method

Fig. 5.2.1 shows the schematic of the device used in the experiment (fabrication details are discussed in Chapter 3). The paddle actuation is performed *in situ* in a transmission electron microscope (TEM) *via* a voltage between the paddle and the gate. The advantage of the TEM is that we can take nano-beam diffraction patterns of the DWNT before and while it is strained. Analysis of these diffraction patterns permits us to determine the chiral indices and the detailed structure of both shells and the atomic deformation of the shells under strain.
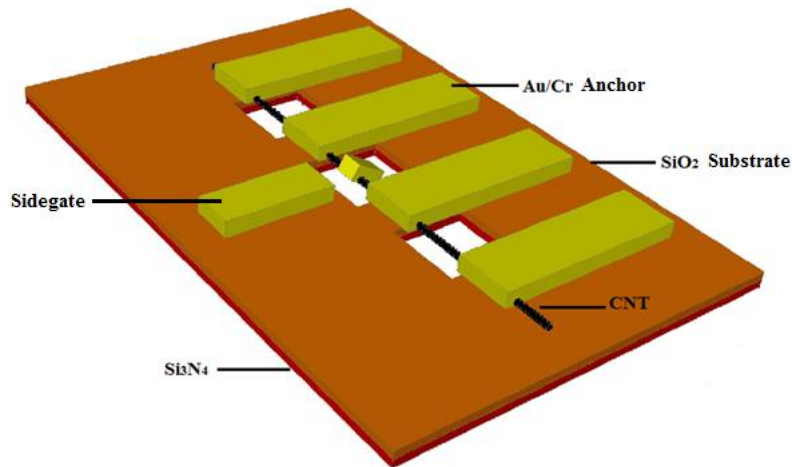
Figure 5.2.1 Schematic of the device which is ready for electrical actuation and *in situ* electron imaging and electron diffraction analysis.

Low-resolution TEM images of the paddle as it is actuated are given in Fig. 5.2.2(B)-(D). They show deflections of 90 °, 117 °, and 147 ° under DC biases 0 V, 40 V and 60 V applied to the gate. The paddle's angular deflection and hence the net strain in the outer shell can be measured directly from changes in the projected length of the

94

paddle. For each of these paddle positions, nano-beam diffraction patterns, Fig. 5.2.2(F)-(H), were recorded from segments on the right or left side of the paddle. Diffraction patterns are also recorded for reference on the untwisted segments between the other anchors (see Fig. 5.2.2(E)). From the diffraction pattern and the diameter measured in direct image mode, the chiral indices (u, v) were identified as (56, 2) (37, 18) from

$\frac{v}{u} = \frac{2D_2 - D_1}{2D_1 - D_2}$ [21], where D_1, D_2 and D_3 are the layer line spacings relative to the

equatorial line for principal layer lines L1, L2 and L3 (which are due to Bragg reflections of graphene (10), $(\bar{1}0)$ and (11), respectively). The three lines mark the vertices of two hexagons which correspond to the hexagonal diffraction geometry due to the top and bottom walls of the nanotube relative to the incident electron beam, respectively. Layer lines L_4, L_5, L_6 are higher order Bragg reflections on graphene and similarly, form larger hexagons. These lines obey the rules that $D_1 = D_2 + D_3$ and

$D_4 = D_1 + D_2$ [22], which can be used to solve the chiral indices when certain lines are not clear in the diffraction patterns. The diffraction patterns of the other parts of the DWNT give the same chiral indices, which imply that the nanotube has the same chiral structure across the entire length. Nano-beam diffraction patterns are recorded for each strain angle. Similar to the previous electron microscope experiments on nanotubes [7, 8, 12], we notice an initial paddle actuation that is apparently due to beam induced charging. Upon removal of the DC bias, the paddle returns to its initial position. This indicates that the strain on the CNT is elastic.

When the nanotube is uniformly twisted about its axis, the pitch separation of the helix will be smaller or larger depending on the handedness of the nanotube relative to

the sense of the twist. From measurements of D_1/D_2 under strain, we are able to calculate the twist angle of each shell by equation [23]

$$\Delta\theta = \frac{\zeta_0 - \zeta}{\zeta - v/u},$$ (5.2.1)

where $\zeta_0 = \frac{2u+v}{u+2v}$ and $\zeta = \frac{D_1}{D_2}$ with D_1 and D_2 being measured from the electron diffraction patterns of the twisted DWNT. The uncertainty of the twist angle is $\pm 0.02\,^\circ/\text{nm}$ along the nanotube, and comes from two parts: the resolution limit of diffraction pattern images (1 pixel out of 1024×1024 pixel image); the thermally excited oscillation of the paddle. Since the thermal oscillation is very small, we can assume that the inner shell had no torsional deformation and the torsional spring constant of the nanotube axis is only determined by the outermost shell, which is estimated to 6.85×10^{-18} N·M [3]. With the device geometry and the tube diameter, 4.45 nm, the amplitude of the oscillation caused by the thermal energy k_BT (where k_B is the Boltzmann constant and $T=300$ K) is no more than 2°, *i.e.* $0.003^o/\text{nm}$ along the tube.
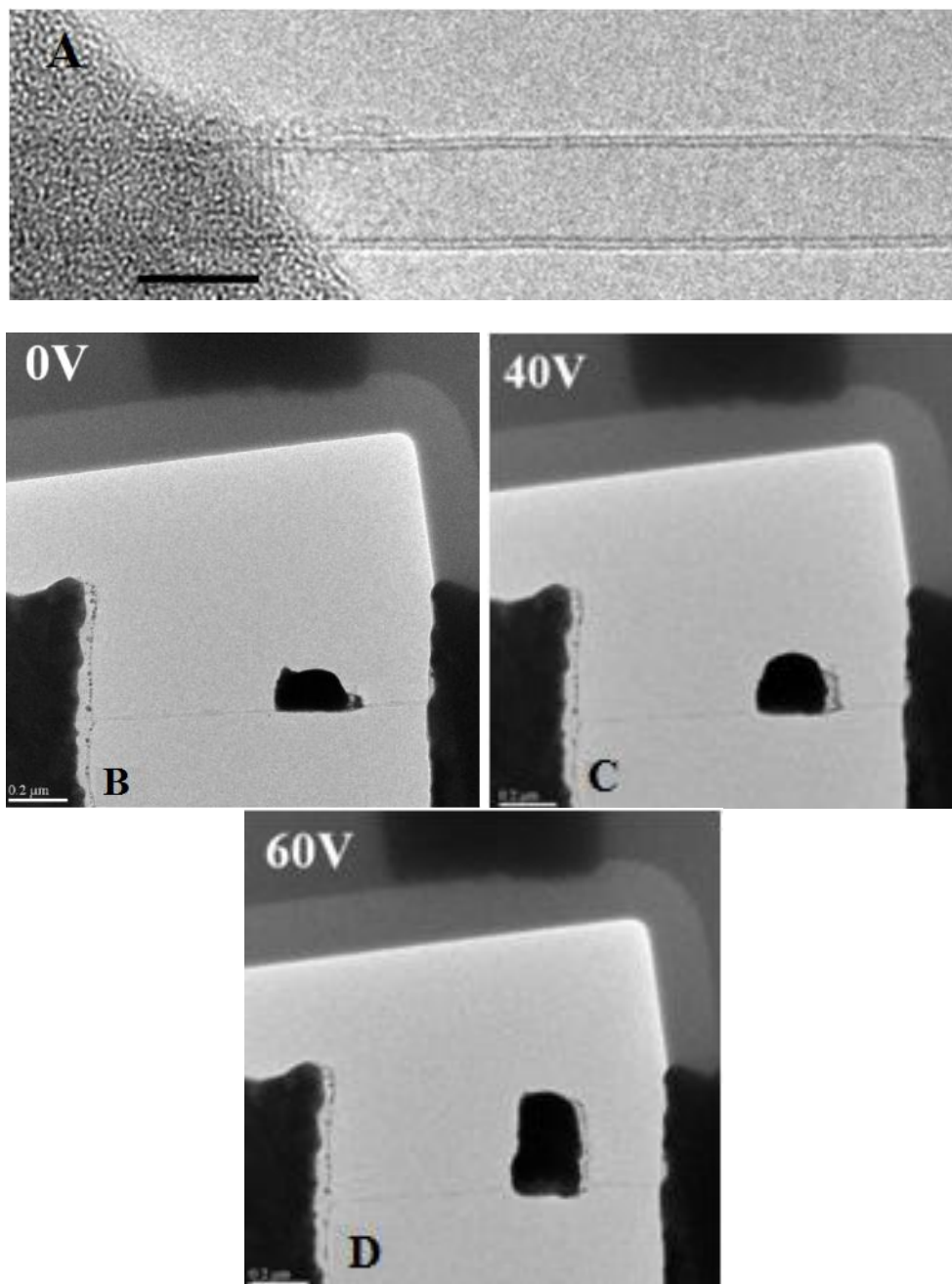
Figure 5.2.2 TEM images and electron diffraction patterns of a suspended DWNT. The diffraction patterns are colored and marked by black arrows for ease of illustration. (A) High resolution TEM image of a typical DWNT employed in our devices. Scale bar, 5 nm. (B)-(D) TEM images of the paddle as it is actuated. They show deflections of $90°$, $117°$ and $147°$ under DC biases 0 V, 40 V and 60 V applied to the gate. Scale bars, 200 nm.
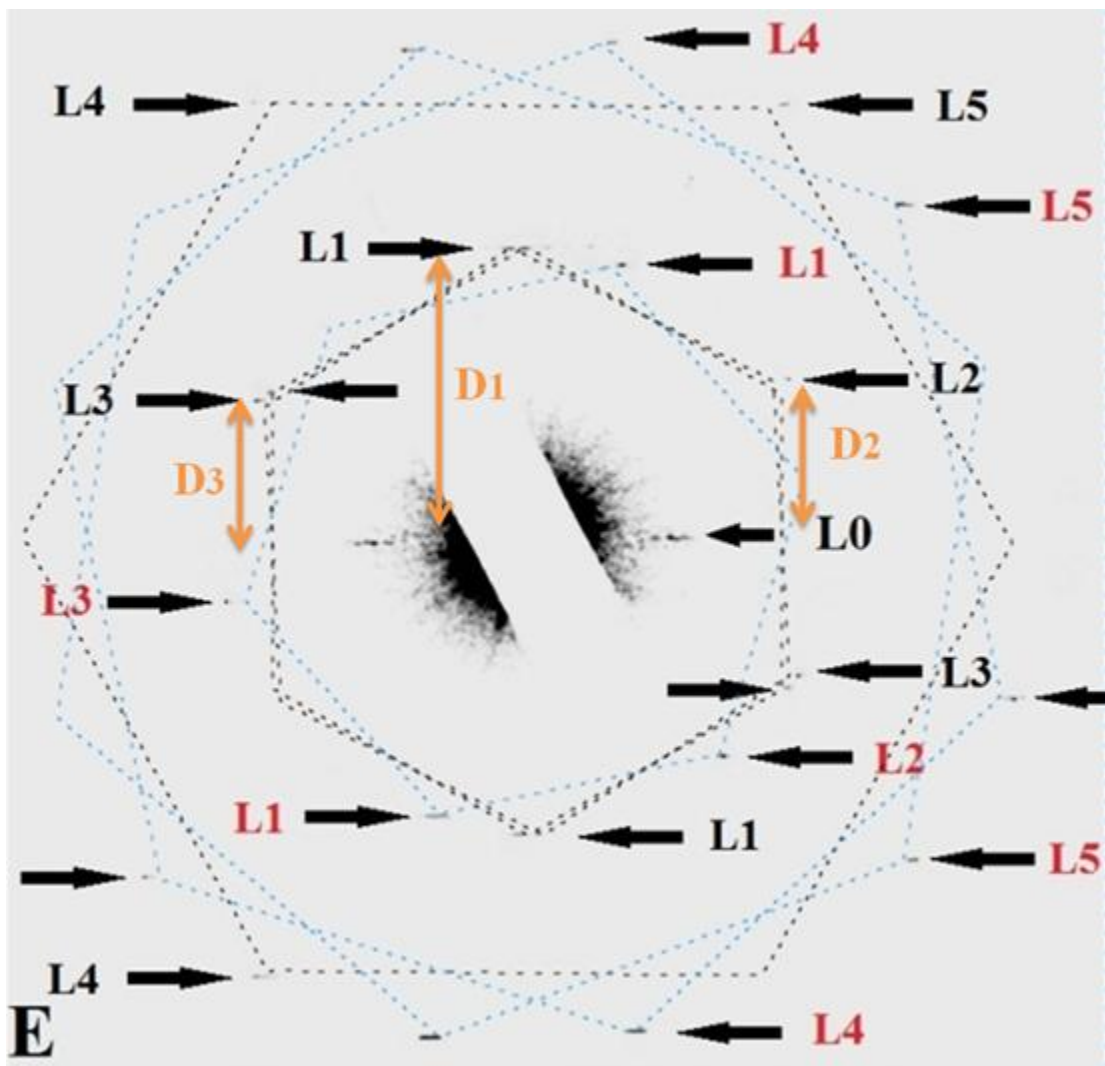
Figure 5.2.2 (continued) (E) Electron diffraction pattern of a non-twisted segment of the DWNT. The black letters and red letters mark the diffraction layer lines of the outer-shell and the inner-shell, respectively. The two hexagons in black represent the primary reflections of graphene (10), $(\bar{1}0)$ and (11) from the outer shell and they form three principal layer lines L1, L2, and L3 above and below the equatorial line, L_0. D_1, D_2 and D_3 are their respective layer line spacings measured from the equatorial line. The larger hexagons in black represent the higher order reflections of graphene on the outer shell. The chiral indices of both shells, (56, 2) (outer shell: diameter 4.467 nm, helicity $\alpha = 1.74°$) and (37, 18) (inner shell: diameter $d = 3.805$ nm, helicity $\alpha = 18.72°$) , are obtained from the diffraction data.

98
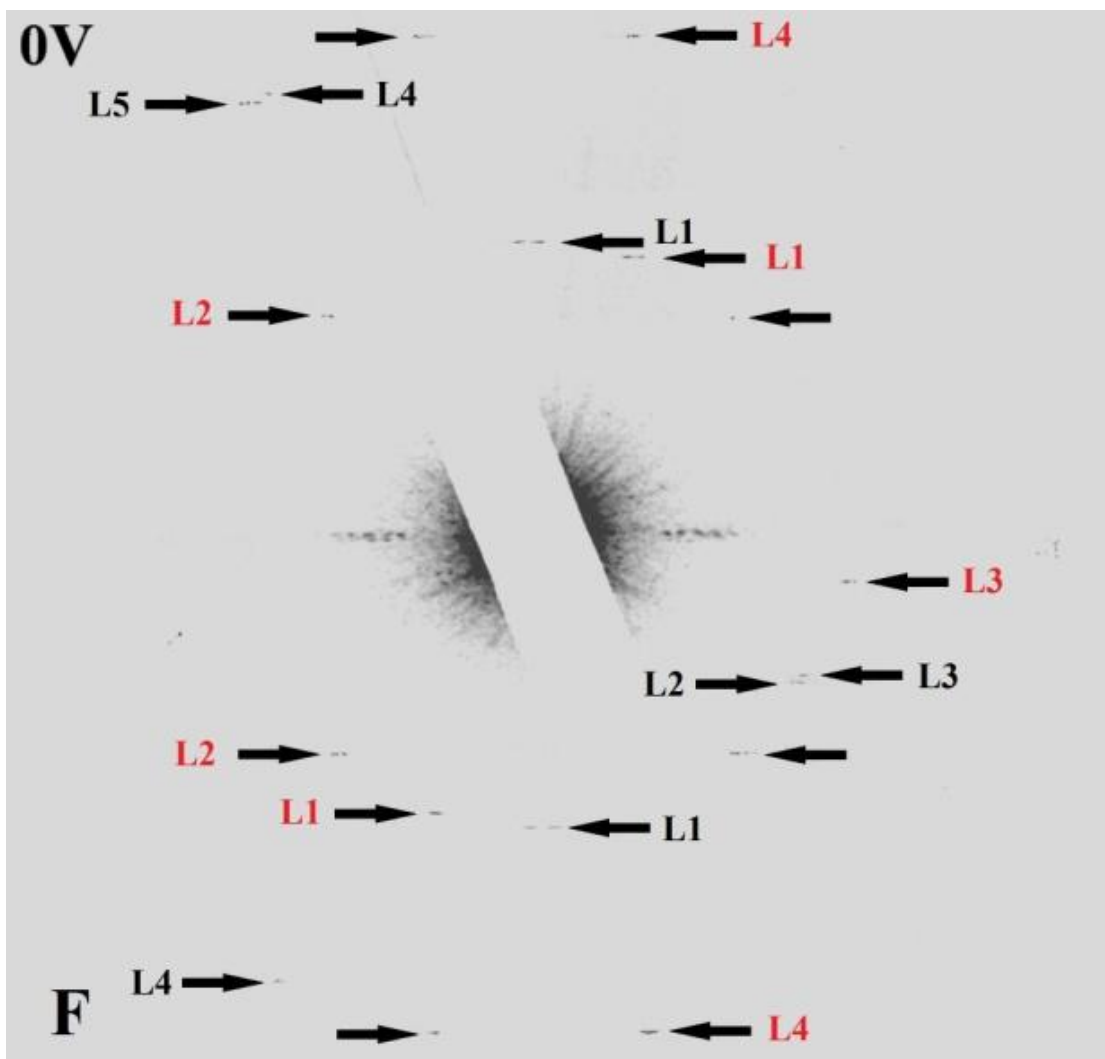
Figure 5.2.2 (continued) (F) Electron diffraction pattern of the DWNT when the paddle is twisted (due to the exposure to the electron beam) under zero bias voltage.
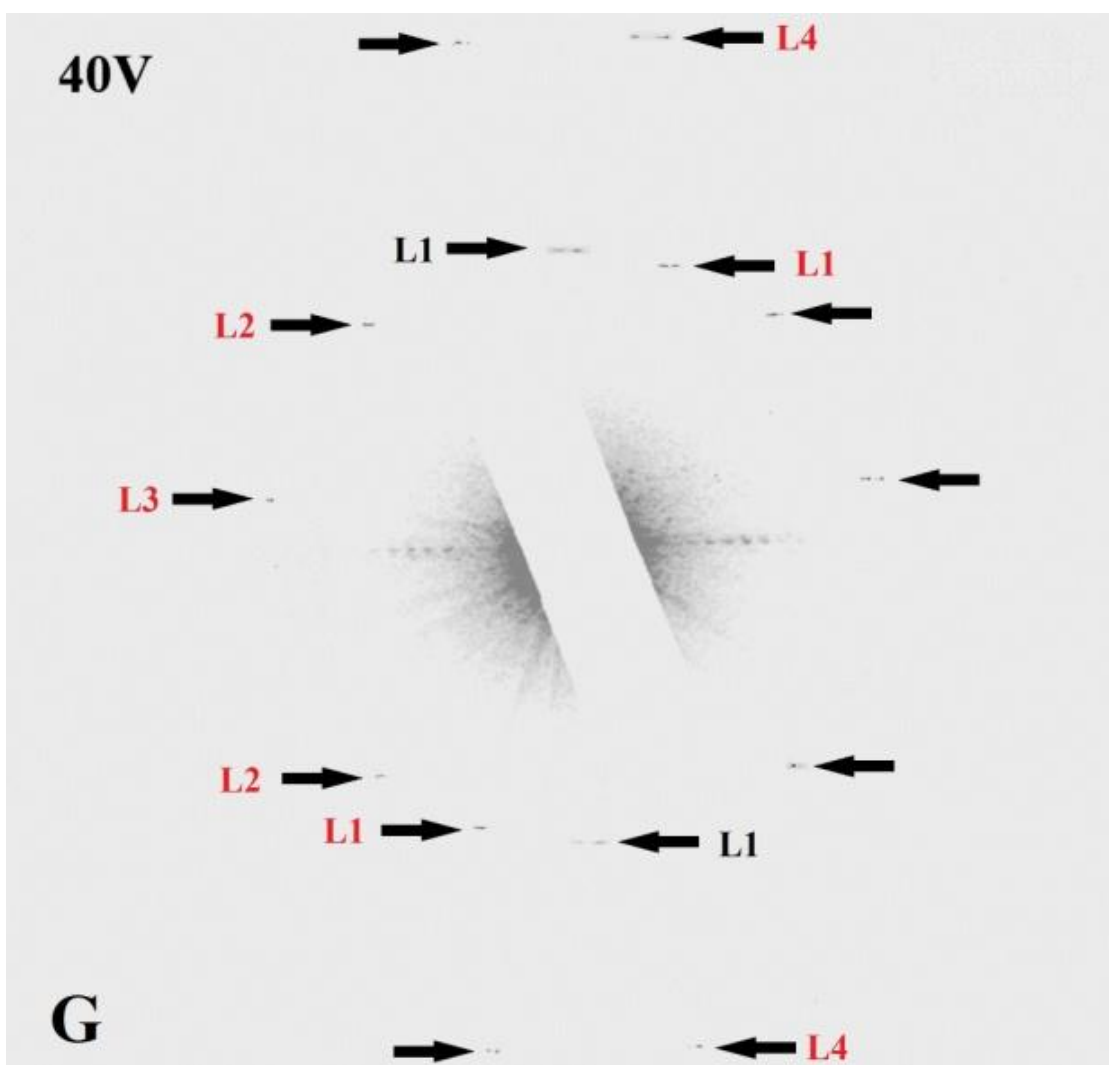
Figure 5.2.2 (continued) (G) Electron diffraction pattern of the DWNT when the paddle is twisted under bias voltage of 40 V.
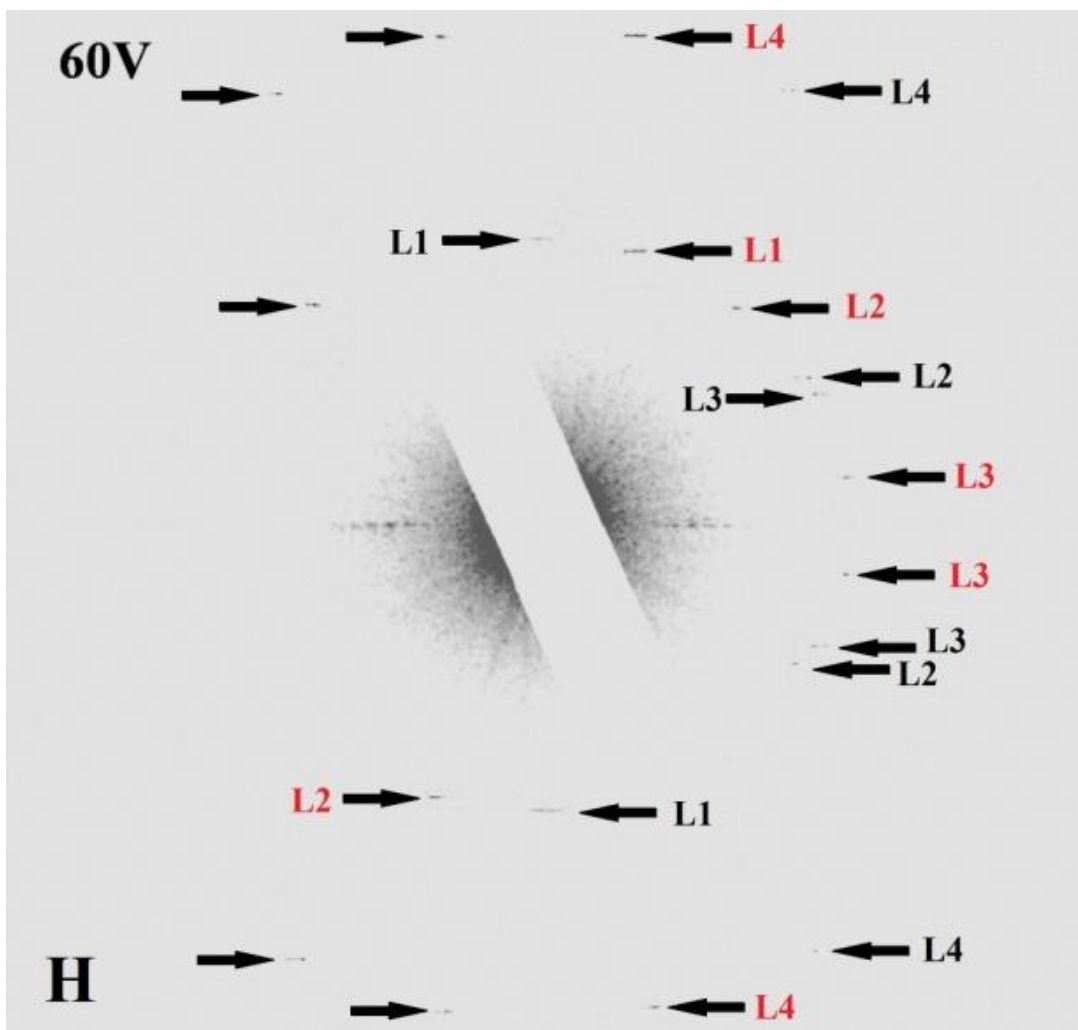
Figure 5.2.2 (continued) (H) Electron diffraction pattern of the DWNT when the paddle is twisted under bias voltage of 60 V.

5.3 Device Modeling and Analysis

Detailed knowledge of the device configuration, paddle geometry, nanotube's twist angles, and DC bias voltages permit us to build an accurate finite element model as reported in an earlier work [8] to calculate the external applied torque on the metal paddle, as illustrated in Fig. 5.3.1. The total electrostatic torque $\vec{\tau}$ on the paddle is given by the surface integral: $\vec{\tau} = \dfrac{1}{\varepsilon_0} \iint\limits_{surface} \sigma_e^{\,2} \vec{R} \times \vec{n} dA$, where ε_0 is the vacuum permittivity, σ_e is the surface charge, $\vec{n}$ is the local unit vector perpendicular to the paddle surface, dA is the infinitesimal surface area on the paddle, and $\vec{R}$ is the positional vector of dA from the DWNT axis as shown in Fig. 5.3.2. For each shell of the DWNT, the shear modulus and torques applied on the nanotube have the relation [18]:

$$G = \sum_i \tau_i \frac{1}{2\pi r^3 \theta t} (\frac{l_1 l_2}{l_1 + l_2}), \tag{5.3.1}$$

where G is the shear modulus, τ_i is the ith torque applied on the shell, r is the nanotube radius, t is the shell thickness (we use 0.34 nm here), θ is the twist angle of the tube, l_1, l_2 are the nanotube lengths to the left and right of the paddle, respectively. The shear moduli of both shells and the interlayer torque can be solved by Eqn. 5.3.1 if θ and the torque applied on the metal paddle are known.

5.4 Results and Discussion

Table 5.1 summarizes the results from experiments on two devices. Within its uncertainty, the twist of the outer shells matches the rotation angles of the paddles. This good match proves that outer-shell's torsion stain is uniformly distributed along the

outer-shell because the diffraction patterns were taken along the different parts of tubule. More importantly, it assures that the measurements on the torsional movement of the inner shell by diffraction patterns are reliable (Therefore, we can use the paddle deflection angle from diffraction patterns, 117° measured from the paddle deflection to replace the undetermined strain in the outer shell at 40 V below). We notice that the calculated outer-shell twisted angles are a bit off the paddle rotation angles. The difference might have been caused by paddle vibrations under electron beam which induced charging during the long exposure in recording the images.

Fig. 5.4.1 compares the strain of the inner shell to the strain of the outer shell. In contrast to the outer-shell MWNT torsional model (where only outer shell twists under an external torque) or the solid MWNT model (where all the shells twists as a solid cylinder), the inner shell strains in proportion to the outer shell but by a smaller amount (20% or less). The intercept indicates that the inner shells twist with the outer shells with no stiction effect.

The fact that DWNT (5, 65) (24, 44) has a larger slope than the DWNT (56, 2) (24, 44) indicates the stronger interlayer coupling in the former DWNT. This is due to (i) the shorter interlayer spacing (0.31 nm in the former DWNT and 0.34 nm in the latter DWNT); (ii) larger contact area along the tube axis between the inner and outer shells, which is equal to the product of the tube perimeter and the length. As a result, the van der Waals interaction is stronger in the former DWNT and its inner shell twists more.
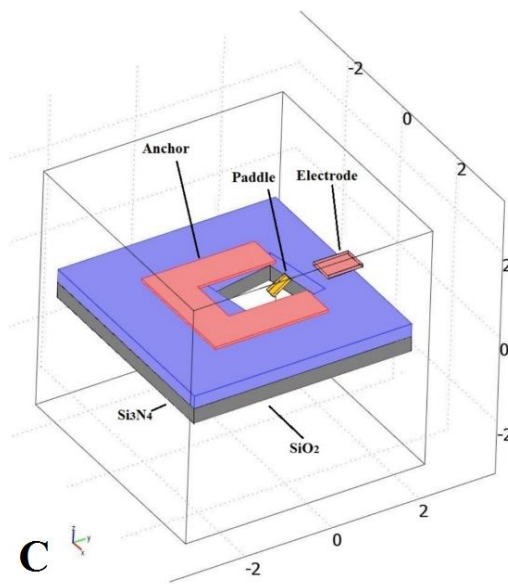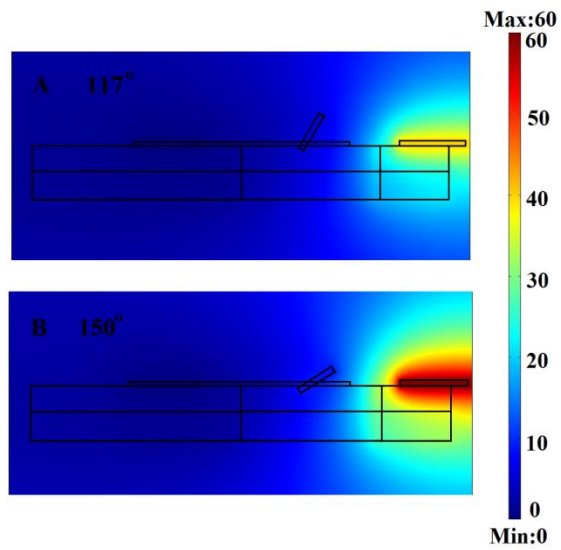
Figure 5.3.1 (A)-(B) Map in side view of electrostatic potential calculated by finite element method when the paddle is twisted at different angles. (C) Schematic of the device geometry in the finite element model. Unit 10^{-6} m.
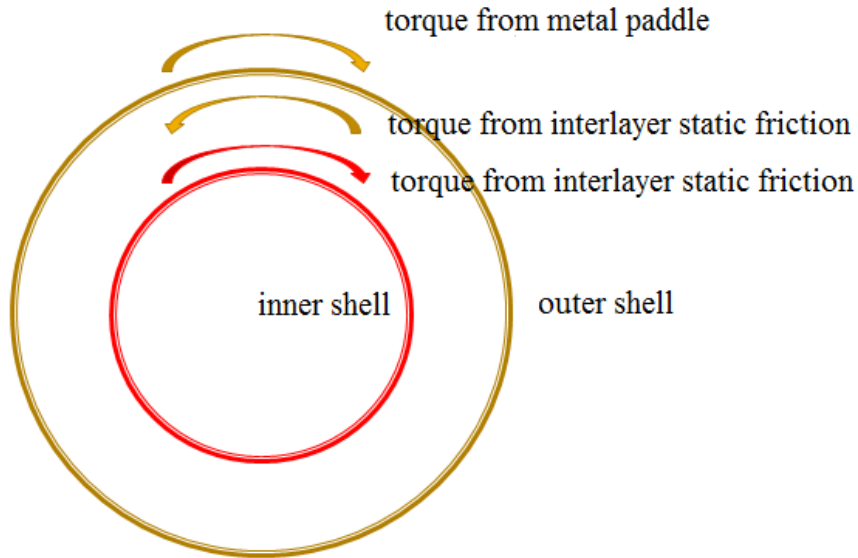
Figure 5.3.2 Schematic of torques applied on the both shells of the DWNT. The yellow curved arrows shows the torques applied on the outer shell, coming from the metal paddle and interlayer van der Waals interaction while the red arrow represents the torque on the inner shell.

Based on these measurements, we can also calculate the shear modulus of the shells, interlayer interaction, *i.e.* van der Waals potential, and friction for the DWNT in device 1, with the help of finite element simulations mentioned above. Plugging the twist angles of both shells and the external torques at 40 V and 60 V calculated from finite element analysis into Eqn. 5.3.1, the outer shell and inner shell moduli are solved to be 0.50 ± 0.01 TPa and 0.41 ± 0.05 TPa, respectively, in agreement with the predictions [3]. Because the twisted angles and diameter of the outer shell can be precisely measured in the TEM, the uncertainty of the outer shell modulus is much smaller compared to the values measured in SEM, ± 0.36 TPa [8]. The uncertainty of the inner shell is 5 times larger due to the larger uncertainty on the measurement of the inner shell twist angles. The interlayer torque between the inner and outer shell at 40 V and 60 V are

$(5.5\pm 4.0)\times 10^{-18}$ N·M and $(8.9\pm 5.0)\times 10^{-18}$ N·M, respectively. If we assume that the interaction is uniform along the tube, interlayer forces F, *i.e.* static friction, between the inner and outer shells at 40 V and 60 V are $(2.9\pm 2.0)\times 10^{-9}$ N $[(3.6\pm 2.4)\times 10^{-15}$ N/atom$]$ and $(4.7\pm 2.6)\times 10^{-9}$ N $[(5.8\pm 3.2)\times 10^{-15}$ N/atom$]$ (calculated from $\vec{\tau}=\vec{r}\times\vec{F}$ where r is the radius of inner-shell and τ is the interlayer torque). The difference between the static friction forces is due to the different van der Waals interactions at the different torsional strains.

We calculate the work done by friction from the relative torsional displacement of the inner-shell and outer-shell from the following equation: $W_f = W_\tau - \Delta E_s - \Delta E_W$, where W_f is the work done by friction, W_τ is the work done by the external torque, ΔE_s is the nanotube strain energy change and ΔE_W is the change of van der Waals energy due to interlayer interactions. The first term the right side of the equation can be calculated by the same finite element analysis method mentioned above and this yields $W_\tau = 258$ eV. The second term is calculated to be 253 ± 4 eV by the equation $\Delta E_s = G\pi \dfrac{(r_o^4 - r_i^4)(\theta_f^2 - \theta_i^2)}{4L}$ [24], where ΔE_s is the strain energy change of one shell in the nanotube, θ_f, θ_i are the final and initial twisted angle, r_o, r_i are the radius of outer shell and inner shell, respectively, and L is the length of the tube. The uncertainty of ΔE_s is estimated by the upper-lower bound method. Standard Lennard-Jones potential is used for the calculation of the total interlayer potential energy $E_p = 4\varepsilon \sum_{i=1}^{N_i} \sum_{j=1}^{N_o} [(\dfrac{\sigma}{r_{ij}})^{12} - (\dfrac{\sigma}{r_{ij}})^{6}]$ [25] as shown in Fig. 5.4.2, where i donates an atom in the inner shell and j an atom in

the outer-shell, N_i and N_o are the total number atoms of the inner and outer shells, r_{ij} is the distance between the ith atom and jth atom. $\varepsilon = 3.622$ meV/atom and $\sigma = 0.385$ nm are used here [25] (The upper cut-off distance of Lennard-Jones potential is taken as 5 times the C-C bond length beyond which the potential is small enough to be considered as zero). The change of van der Waals energy from $117\,^\circ$ to $147\,^\circ$ is 0.37 eV. Thus, the work of friction is 4.63 ± 4 eV. This yields an average kinetic friction force,

$$f_k = 2.1 \pm 0.9 \times 10^{-9} \text{ N } (2.6 \pm 1.0 \times 10^{-15} \text{ N/atom}) \text{ calculated by } W_f = \frac{1}{2} f_k \Delta\theta (r_i + r_o)/2,$$

and $\Delta\theta$ is the relative angular displacement of outer shell to inner shell when the paddle is rotated from 117° to 147°. This is about 50% larger than the upper-limit value of the kinetic friction measured in a telescoping motion in a MWNT [19]. The difference may be due to the following two factors: first, the telescoping motion was measured by a method that prejudicially slides the layers with the least interlayer interaction within a MWNT experiment. Instead, we measure the torsional motion in a DWNT. Second, the interaction area never changes in our experiment but it was constantly shrinking in the telescoping motion, which further biases the result to lower values. Meanwhile, the work of friction (4.63 eV, $i.e.$ 580 μeV/atom) can be considered as the energy barrier which is needed to initiate and maintain the relative torsional motion of about $30°$. The theoretical prediction of the energy barriers for an interlayer rotation of the same angle in a DWNT (5, 5) (10, 10) are 590 μeV/atom based on the tight-binding plus dispersion model and 1040 μeV/atom based on the local density approximation [26]. The relative displacement of carbon atoms in a rotation motional is larger than that in a torsional motion. If the atomic displacement in the latter is considered linear, the total displacement will be half of the displacement in the former. Thus, the energy barriers for an interlayer torsional

motion in a DWNT (5, 5) (10, 10) are estimated to 295 μeV/atom and 520 μeV/atom, respectively. The experimental value is close to (about 12% larger) the theoretical prediction based on the local density approximation model. It should also be noticed that lattice strain caused by tube twisting could change ε and σ in the Lennard-Jones model and affect energy barrier in the above estimates.

In summary, two DWNT-based torsion pendulums were strained reproducibly from 0° to almost 180° elastically. The inner shell strained in proportion to the outer shell but by only a small fraction (of order 10%), and the degree of frictional coupling between the shells was calculated. The DWNT with a short interlayer distance and a larger interlayer contact area exhibits a stronger interlayer coupling. This is the first detailed measurement of friction with complete atomic-scale characterization of the process. These results will be important in the understanding and design of nano-electromechanical systems that require a fine control of friction and dissipation between nanoscale objects.
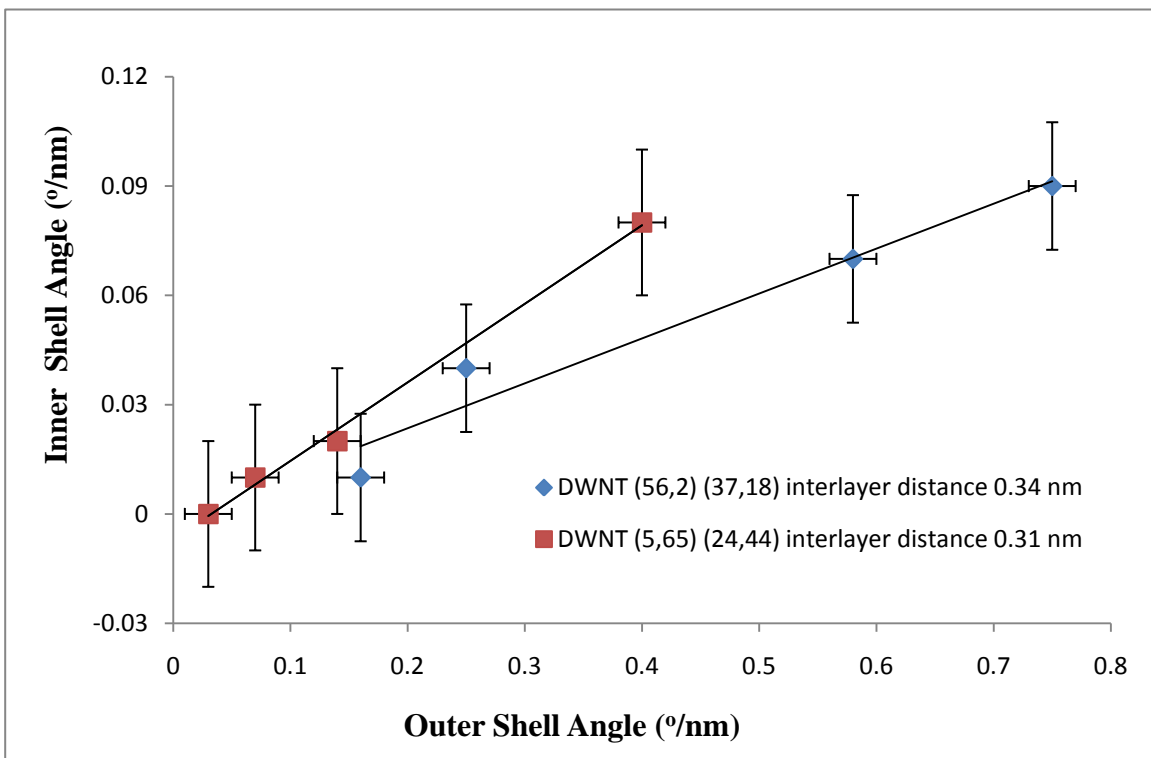
Figure 5.4.1 The inner-shell's torsional response to the torsional deformation of the outer-shell of the two DWNT devices we measured in this work. DWNT1: (diameter $d = 4.467$ nm, helicity $\alpha = 1.74°$), ($d = 3.805$ nm, $\alpha = 18.72°$); DWNT2: ($d = 5.299$ nm, $\alpha = 56.33°$), ($d = 4.679$ nm, $\alpha = 39.64°$). The horizontal axis is the torsional twist angle (°/nm) of out-shell and vertical axis (°/nm) is the torsional twist angle of the inner-shell.
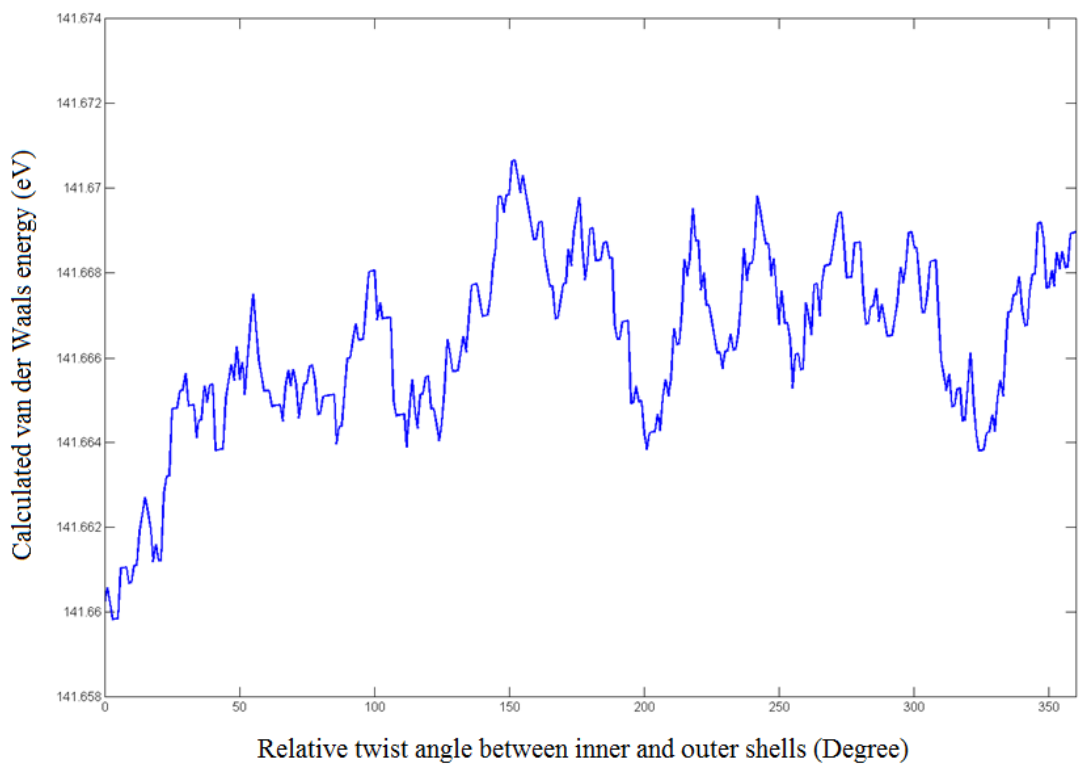
Figure 5.4.2 Calculated van der Waals energy of DWNT in device 1 as the function of the relative twist angle between the inner and the outer shells (the length of the nanotube is reduced to 100 nm to simplify the calculation).

Dev	Voltage(V)	Location	Shell	Handed-ness	D_1/D_2	$\Delta(D_1/D_2)$	L(nm)	Twisting Direction	$\Delta\theta(°)$	$\Delta\theta_{TEM}(°)$	$\Delta\theta/L$ (±0.02°/nm)
1	0	Left	Outer	Right-handed	1.950	-0.050	600	Clockwise	96±12	90	0.16
			Inner		1.263	-0.003	600		6±12		0.01
	40	Right	Outer		n/a	n/a	200	Counter-clockwise	n/a	117	n/a
			Inner		1.241	0.019	200		14±4		0.07
	60	Left	Outer		1.981	-0.081	600	Clockwise	150±12	147	0.25
			Inner		1.272	-0.012	600		24±12		0.04
	60	Right	Outer		1.698	0.202	200	Counter-clockwise	146±4	147	0.73
			Inner		1.236	0.024	200		18±4		0.09
2	0	Left	Outer	Left-handed	1.758	0.042	560	Clockwise	78.5±11.2	66	0.14
			Inner		1.214	0.003	560		11.2±11.2		0.02
	0	Right	Outer		1.926	-0.126	190	Counter-clockwise	76±3.8	66	0.40
			Inner		1.243	-0.026	190		15.2±3.8		0.08
	15	Left	Outer		1.78	0.020	560	Clockwise	39.2±11.2	55	0.07
			Inner		1.215	0.002	560		5.6±11.2		0.01
	35	Left	Outer		1.791	0.009	560	Clockwise	16.8±11.2	n/a	0.03
			Inner		1.221	-0.004	560		0±11.2		0

Table 5.1 Summary of electron diffraction analysis of the DWNT devices measured in this work. The second column is the electrode voltage applied to rotate the metal paddle. The third column indicates whether the nanotube diffraction pattern is taken at the right side or left side of the paddle. D_1/D_2 is the diffraction layer line spacing ratio shown in Fig. 5.2.2 $\Delta(D_1/D_2)$ is the shift of diffraction layer line when the nantobue is twisted. Positive sign indicates the layer lines move toward each other and negative sign indicates the lines move away from each other. L is the length of the nanotube from the paddle to the anchor. $\Delta\theta$ and $\Delta\theta_{TEM}$ are the twisting angle along the tube calculated from the diffraction patterns and the rotation angle of the paddle measured in the TEM images, respectively. Last column $\Delta\theta/L$ is nanotube twisting angle per nanometer. n/a in the table indicates that we are not able to obtain diffraction patterns or TEM images of the device in that condition.

5.5 References

[1]   Anantram, M. P. & Leonard, F., Physics of Carbon Nanotube Electronic Devices. *Rep. Prog. Phys.* **69**, 507-561 (2006).

[2]   Shibutani, Y. & Ogata, S., Mechanical Integrity of Carbon Nanotubes for Bending and Torsion. *Model. Simul. Mater. Sci. Eng.* **12**, 599-610 (2004).

[3]   Lu, J. P., Elastic Properties of Carbon Nanotubes and Nanoropes. *Phys. Rev. Lett.* **79**, 1297-1300 (1997).

[4]   Treacy, M. M. J., Ebbesen, T. W. & Gibson, J. M., Exceptionally High Young's Modulus Observed for Individual Carbon Nanotubes. *Nature* **381**, 678-680 (1996).

[5]   Wong, E. W., Sheehan, P. E. & Lieber, C. M., Nanobeam Mechanics: Elasticity, Strength, and Toughness of Nanorods and Nanotubes. *Science* **277**, 1971-1975 (1997).

[6]   Ishigami, M., Aloni, S. & Zettl, A., Properties of Boron Nitride Nanotubes. *AIP Conference Proceedings* **696**, 94-99 (2003).

[7]   Meyer, J. C., Paillet, M. & Roth, S., Single-Molecule Torsional Pendulum. *Science* **309**, 1539-1541 (2005).

[8]   Hall, A. R., An, L., Liu, J., Vicci, L., Falvo, M. R., Superfine, R. & Washburn, S., Experimental Measurement of Single-Wall Carbon Nanotube Torsional Properties. *Phys. Rev. Lett.* **96** (2006).

[9]   Bourlon, B., Glattli, D. C., Miko, C., Forro, L. & Bachtold, A., Carbon Nanotube Based Bearing for Rotational Motions. *Nano Lett.* **4**, 709-712 (2004).

[10]   Fennimore, A. M., Yuzvinsky, T. D., Han, W. Q., Fuhrer, M. S., Cumings, J. & Zettl, A., Rotational Actuators Based on Carbon Nanotubes. *Nature* **424**, 408-410 (2003).

[11]   Forro, L., Nanotechnology - Beyond Gedanken Experiments. *Science* **289**, 560-561 (2000).

[12]   Papadakis, S. J., Hall, A. R., Williams, P. A., Vicci, L., Falvo, M. R., Superfine, R. & Washburn, S., Resonant Oscillators with Carbon-Nanotube Torsion Springs. *Phys. Rev. Lett.* **93** (2004).

[13]   Cohen-Karni, T., Segev, L., Srur-Lavi, O., Cohen, S. R. & Joselevich, E., Torsional Electromechanical Quantum Oscillations in Carbon Nanotubes. *Nat. Nanotechnol.* **1**, 36-41 (2006).

[14]   Craighead, H. G., Nanoelectromechanical Systems. *Science* **290**, 1532-1535 (2000).

[15]   Williams, P. A., Papadakis, S. J., Patel, A. M., Falvo, M. R., Washburn, S. & Superfine, R., Torsional Response and Stiffening of Individual Multiwalled Carbon Nanotubes. *Phys. Rev. Lett.* **89** (2002).

[16]   Lu, J. P., Elastic Properties of Single and Multilayered Nanotubes. *J. Phys. Chem. Solids* **58**, 1649-1652 (1997).

[17]   Hall, A. R., Falvo, M. R., Superfine, R. & Washburn, S., A Self-Sensing Nanomechanical Resonator Built on a Single-Walled Carbon Nanotube. *Nano Lett.* **8**, 3746-3749 (2008).

[18]   Seed, G. M., *Strength of Materials : An Undergraduate Text* (Saxe-Coburg, [Edinburgh, UK], 2000).

[19]   Kis, A., Jensen, K., Aloni, S., Mickelson, W. & Zettl, A., Interlayer Forces and Ultralow Sliding Friction in Multiwalled Carbon Nanotubes. *Phys. Rev. Lett.* **97** (2006).

[20]   Cumings, J. & Zettl, A., Low-Friction Nanoscale Linear Bearing Realized from Multiwall Carbon Nanotubes. *Science* **289**, 602-604 (2000).

[21]   Qin, L.-C., Electron Diffraction from Carbon Nanotubes. *Rep. Prog. Phys.* **69**, 2761-2821 (2006).

[22]   Deniz, H., Electron Diffraction and Microscopy Study of Nanotubes and Nanowires. PhD Thesis, The University of North Carolina at Chapel Hill, (2007).

[23]   Liu, Z. J. & Qin, L.-C., A Practical Approach to Determine the Handedness of Chiral Carbon Nanotubes by Electron Diffraction. *Chem. Phys. Lett.* **405**, 265-269 (2005).

[24]   Nagapriya, K. S., Goldbart, O., Kaplan-Ashiri, I., Seifert, G., Tenne, R. & Joselevich, E., Torsional Stick-Slip Behavior in WS$_2$ Nanotubes. *Phys. Rev. Lett.* **101** (2008).

[25]   Guo, W. L., Zhong, W. Y., Dai, Y. T. & Li, S. A., Coupled Defect-Size Effects on Interlayer Friction in Multiwalled Carbon Nanotubes. *Phys. Rev. B* **72** (2005).

[26]   Palser, A. H. R., Interlayer Interactions in Graphite and Carbon Nanotubes. *Phys. Chem. Chem. Phys.* **1**, 4459-4464 (1999).

Chapter 6

Revealing the Handedness of Carbon Nanotubes by Electron Diffraction

6.1 Introduction

In order to determine the properties of a carbon nanotube completely, we need, not only the chiral indices, but also the handedness of the nanotube. The nanotube is designated as right-handed using chiral indices $u > v \geq 0$ and left-handed by $v > u \geq 0$. Although the electronic properties of a carbon nanotube have proven to be independent of their handedness [1-3], the knowledge of nanotube handedness is important in the understanding of their spin related properties, such as the interactions with photons [4-8].

As mentioned in Chapter 4, STM has shown their capability of telling the handedness of a SWNT [9, 10], but it also shows its limitations on the MWNTs, especially the inner shell structure. Electron diffraction, which can be used to determine the chiral indices of both SWNTs and MWNTs, cannot tell the handedness due to the 2mm symmetry (one two-fold axis and two mirror planes) of scattering intensities for the right-handed and left-handed nanotube structures, either [11]. However, this symmetry is

broken when the nanotube is twisted about its tubule axis. It is then possible to tell the handedness of the nanotube from the shift of its diffraction pattern under a torsional strain.

Liu and Qin reported a theoretical prediction on the shift of diffraction lines for both left-handed and right-handed CNT under a torsional strain in 2005 [12]. Meyer, et al. reported an experimental observation of the shift of diffraction layer lines of a SWNT bearing a torsional strain in 2005 [13]. Fig. 6.1.1 shows how a SWNT is twisted about the tubule axis: one end is twisted either clockwise or counter-clockwise about the tubule axis while the other end is fixed. If the twisted angle is smaller than the threshold angle beyond which buckling will take place and the deformation becomes plastic, the cross section of the SWNT can be assumed circular and the total surface area is unchanged. Based on these two assumptions, the twisted SWNT (*u, v*) still consists of *u* pairs of properly-arranged helices just like the untwisted CNT and the axial distance between neighboring atoms along a helix keeps the same, *i.e.* $\Delta^* = a_0 tan(60° - \alpha)$, where α is the helical angle and $a_0 = 0.246$ nm is the magnitude of the basis vector in graphene lattice. But the pitch length of the twisted nanotube becomes $C^* = C/(1 + \Delta\theta/2\pi)$, where C is the pitch length of the untwisted CNT and $\Delta\theta$ is the twist angle per nm. From the geometry of the twisted CNT projected in the radial direction, as illustrated in Fig. 6.1.2, the horizontal movements between the neighboring pair of helices can be derived as [12]

$$\frac{\Delta y}{u} = \frac{a_0 sin\alpha}{tan(60^0 - \alpha)} \frac{\Delta x}{A},$$
(6.1.1)

where $\Delta x, \Delta y$ are the displacement of carbon atoms and A is the perimeter of the CNT.

From the CNT diffraction theories described in Chapter 2 and Eqn. 6.1.1, the relation between $\Delta\theta$ and the shift of the diffraction layer lines D_1'/D_2' is derived as [12]

$$\Delta\theta = \frac{D_1 / D_2 - D_1' / D_2'}{D_1' / D_2' + v / u},$$ (6.1.2)

where D_1 and D_2 are the diffraction layer line spacings measured from the diffraction pattern of untwisted CNT, D_1' and D_2' are the corresponding layer line spacings measured from the diffraction pattern of twisted CNT. The numerator of Eqn. 6.1.2 can be either positive or negative depending on whether the diffraction layer lines L1 and L2 move toward or away from each other under torsional strain. The layer line spacings D_1, D_2, and D_3 in the reciprocal space are inversely proportional to the pitch lengths of the 3 equivalent sets of helices in the real space, which are parallel to the lattice vectors $\vec{a}_1$, $\vec{a}_2$ and $\vec{a}_1 - \vec{a}_2$, respectively. As we can see from the equation $C^* = C/(1 + \Delta\theta/2\pi)$, the new pitch length C^* will become either longer or smaller dependent on the sign of twist angle $\Delta\theta$. Fig. 6.1.3 shows an example of a right handed helix under torsion. If one end of the helix is fixed and the other end is twisted clockwise (counter-clockwise), the pitch length will become longer (smaller). The situation is opposite for a left-handed helix. Within a carbon nanotube, the two equivalent helices parallel to the lattice vectors $\vec{a}_1$ and $\vec{a}_1 - \vec{a}_2$ always have the same handedness while the other equivalent helix has the opposite handedness. Therefore, D_1 and D_3 always move in the same direction while D_2 moves in the opposite direction. As the result, the diffraction layer line ratio D_1' / D_2' will decrease (increase) for a right-handed nanotube and the ratio will increase (decrease) for a left-handed one if one end of the nanotube is fixed and the other end is twisted clockwise (counter-clockwise). Fig. 6.1.4 shows simulated diffraction patterns of a right-handed nanotube (22, 2) when it is twisted $1.20°/nm$ counter-clockwise and clockwise about the tubule axis.

This theoretical prediction is verified via the torsional devices fabricated on SWNTs and DWNTs, in which the CNT diffraction patterns are taken before and while the CNTs are twisted. This chapter will detail the experimental results using the torisonal devices.
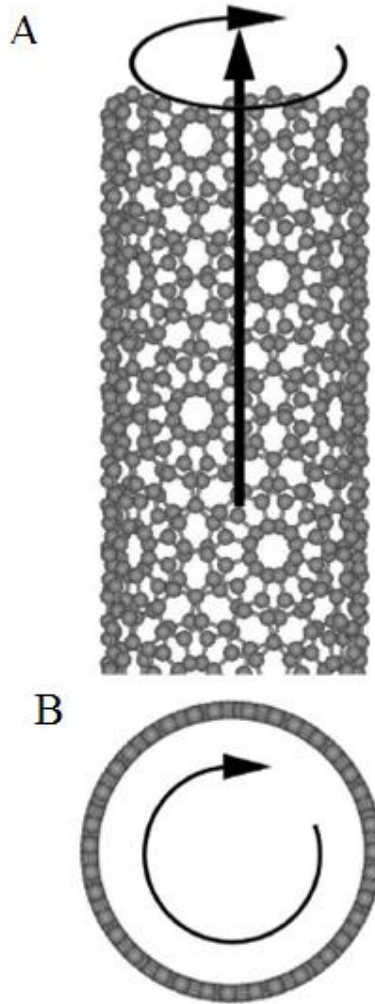
Figure 6.1.1 (a) Schematic showing twisting a carbon nanotube about its tubule axis in side-view. (b) Viewed end-on. The circle with arrow in (a) and (b) indicate the nanotube is twisted clockwise. Images adapted from [12].
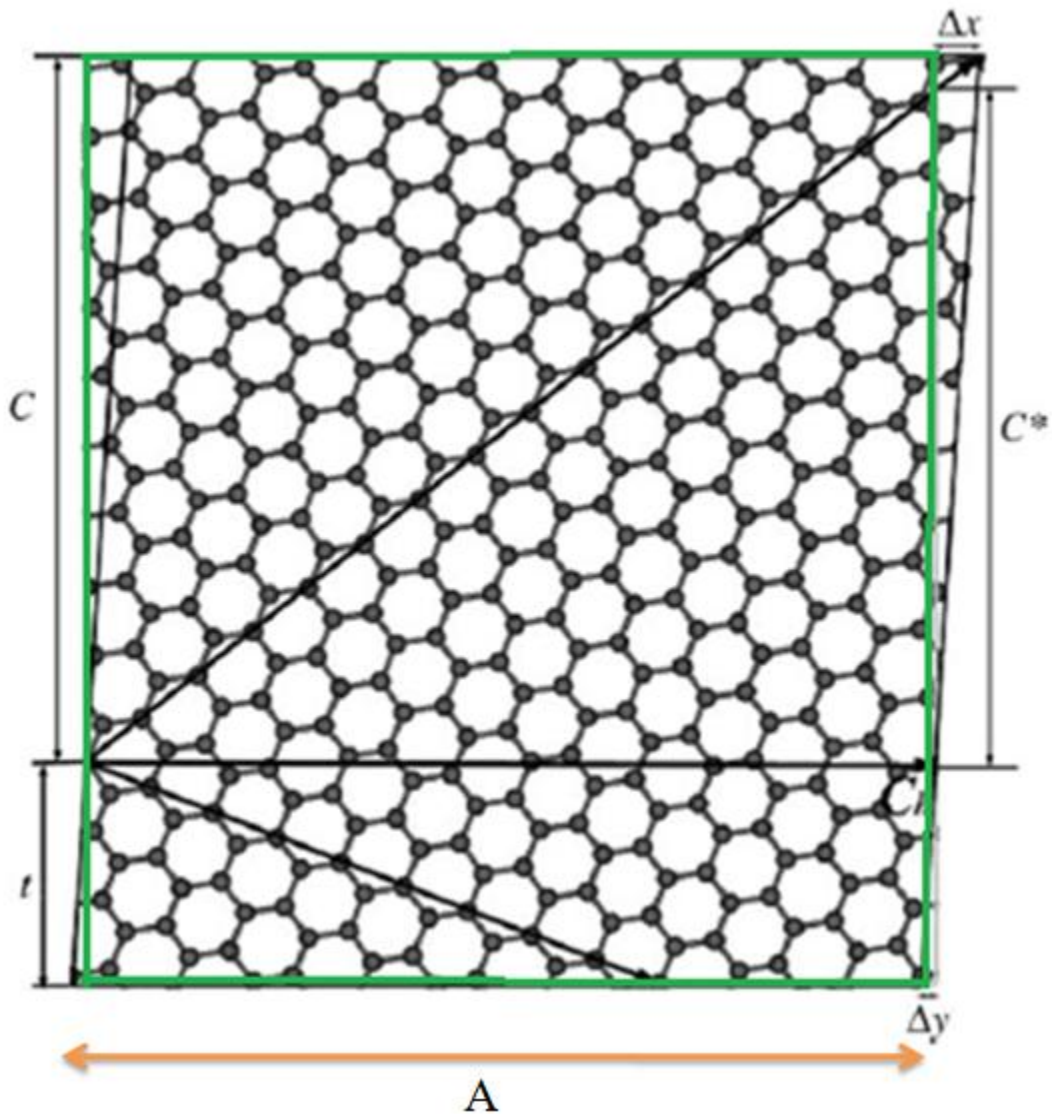
Figure 6.1.2 Radial projection of a SWNT twisted about the tubule axis. The green-lined rectangle and the dark-lined parallelepiped are the graphene cut before and after twisting. The twisting angle is reflected as the displacement of atoms such as Δx and Δy in graphene. A is the magnitude of the perimeter vector of the nanotube which is independent of the twisted angle and $t = ua_0 sin\alpha$. C and C^* are the pitch lengths of the constituting carbon helices before and after the nanotube is twisted. Images adapted from [12].
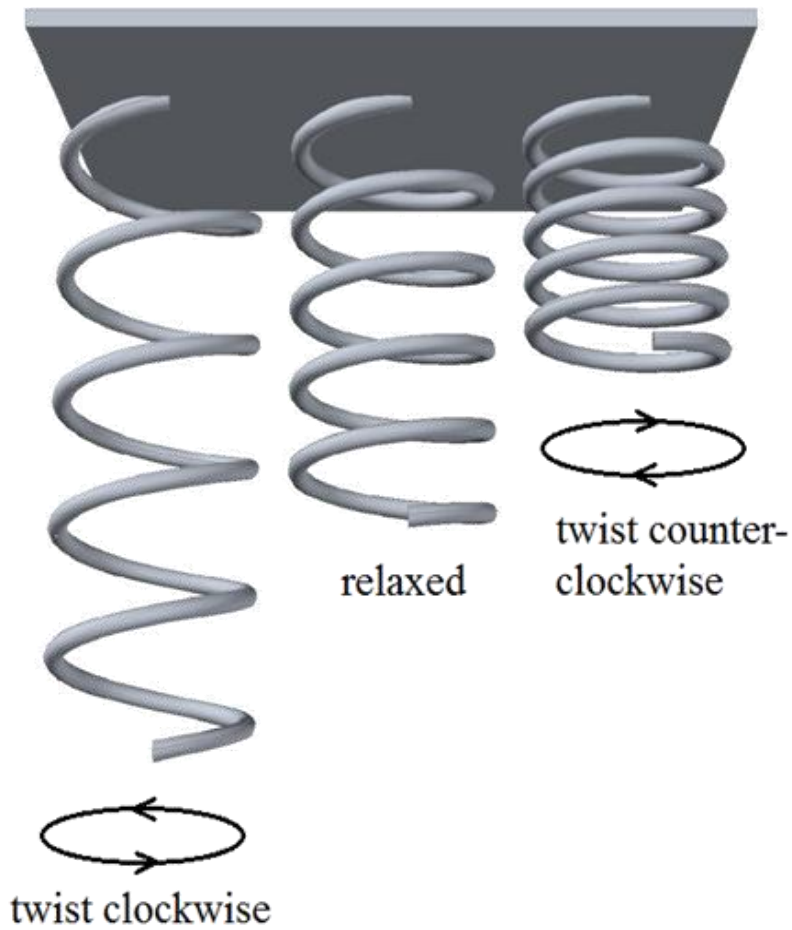
Figure 6.1.3 Schematic of a right handed helix which is relaxed, twisted clockwise and counter-clockwise, respectively.
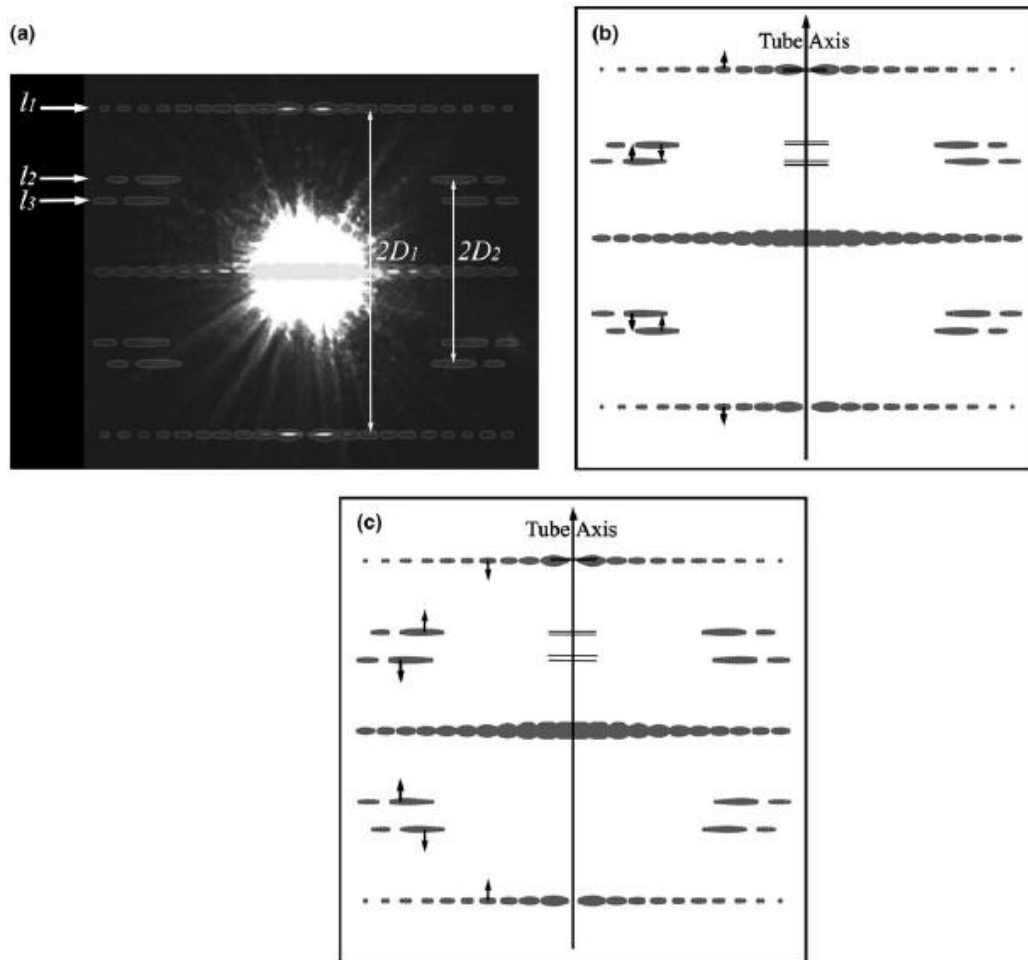
Figure 6.1.4 (a) Electron diffraction pattern of an un-twisted SWNT (22, 2). (b) The simulated electron diffraction of the same nanotube twisted counter-clockwise ($\Delta\theta = -1.20^\circ / nm$). (c) Diffraction pattern of the nanotube twisted clockwise ($\Delta\theta = 1.20^\circ / nm$). The dark lines on the central line mark the positions of the principal lines of the nantoube with or without twisting, respectively. Images adapted from [12].

6.2 Experimental

Same torsional devices, as mentioned in Chapter 5, are fabricated using DWNTs and SWNTs, as illustrated in Fig. 5.2.1. Electron diffraction patterns were first taken from the CNT segments without paddle. The chiral indices and the ratio of layer line spacing D_1 and D_2 are derived from the diffraction patterns for reference. Then a DC voltage is applied onto the side gate to rotate the paddle and diffraction patterns from the twisted CNT are taken simultaneously. The handedness is determined by the sign of the change of the layer line spacings, *i.e.* the ratio of the untwisted layer line spacing less by that of the twisted layer line spacing, corresponding to the tubule twist direction.

A TEM image of the paddle as it is actuated is shown in Fig. 6.2.1(A). It shows a deflection of 147 ° under the DC bias of 60 V applied to the gate. The paddle's angular deflection and hence the net strain in the outer shell is measured directly from the change in the projected length of the paddle. To obtain the net strain in both outer and inner shells, a nano-beam diffraction pattern, Fig. 6.2.1(C), was recorded from the segment on the left side of the paddle. Diffraction patterns were also recorded for reference on the untwisted segments between the other anchors (see Fig. 6.2.1(B)). From the diffraction pattern and the diameter measured in direct image, the chiral indices (u, v) were identified as (56, 2) (37, 18) from $\dfrac{v}{u} = \dfrac{2D_2 - D_1}{2D_1 - D_2}$ [14].

6.3 Results and Discussion

Fig. 6.2.1(C) compares the diffraction pattern of the twisted DWNT to that of the un-twisted DWNT. Clearly, the diffraction layer lines L1 and L2 are moving away from each other for both shells as expected for a right-handed nanotube when it is twisted

counter-clockwise. Fig. 6.3.1 shows the intensity profiles of the diffraction layer lines L1 of the outer-shell before and while the DWNT is twisted. The red curves are the simulated best-fit Bessel function of order 2, which indicates the chiral index for v is 2 (details discussed in Chapter 2). The overlap between the left side and the right side of the Bessel function in Fig. 6.3.1(B) indicates that the vertices of the top and the bottom graphene hexagon move away from each other in the plane perpendicular to the incident beam. Given that the DWNT is twisted counter-clockwise at the open end (the other end is fixed by the metal anchor deposited on the nanotube) looking from the open end, we determined that both shells of the DWNT (56, 2) (37, 18) are right-handed.
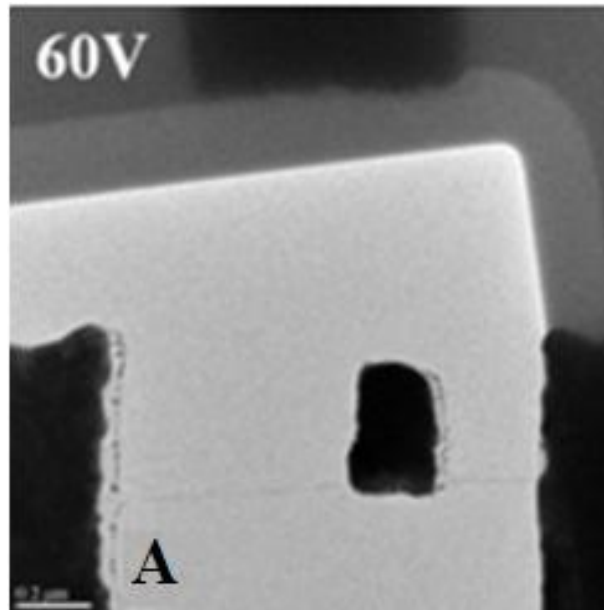
Figure 6.2.1 TEM image and electron diffraction patterns of a suspended DWNT. The diffraction patterns are colored and marked by black arrows for ease of illustration. (A) TEM image of the paddle as it is actuated. It shows a deflection of 147° under DC bias of 60 V applied to the gate. Scale bar, 200 nm.
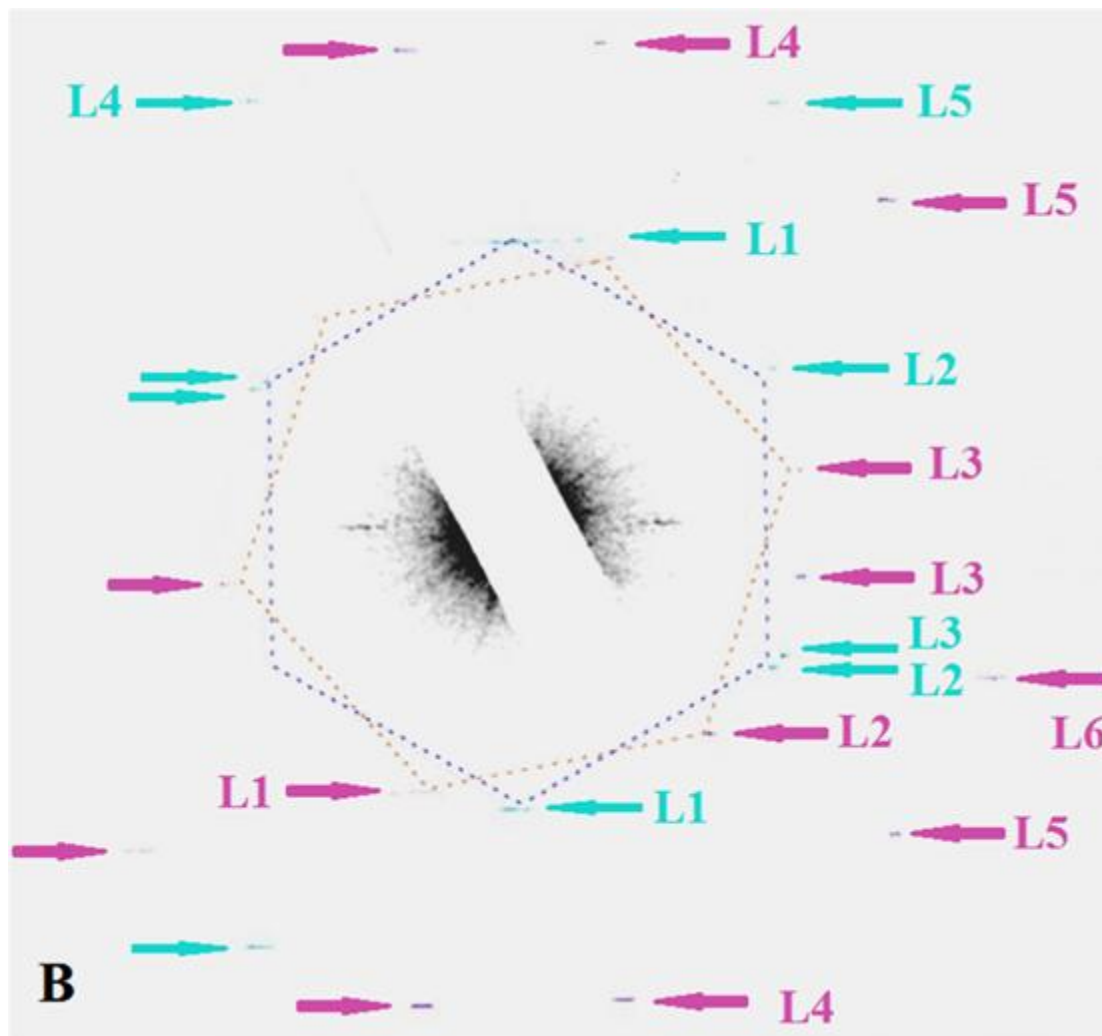
Figure 6.2.1 (continued) (B) Diffraction pattern of an un-twisted segment of the DWNT. The green and pink arrows mark the diffraction layer lines of the outer-shell and the inner-shell, respectively. The two hexagons in yellow and blue represent the primary reflections of graphene (10), $(\bar{1}0)$ and $(1\bar{1})$ from the outer-shell and inner-shell, respectively. Each of them forms three principal layer lines L1, L2, and L3 above and below the equatorial line, L0. D_1, D_2 and D_3 are their respective layer line spacings measured from the equatorial line. Layer lines L4, L5 and L6 are due to the higher order reflections of graphene from the two shells. The chiral indices of both shells, (56, 2) (outer shell: diameter 4.467 nm, helicity $\alpha = 1.74°$) and (37, 18) (inner shell: diameter $d = 3.805$ nm, helicity $\alpha = 18.72°$), are obtained from the diffraction data.

123
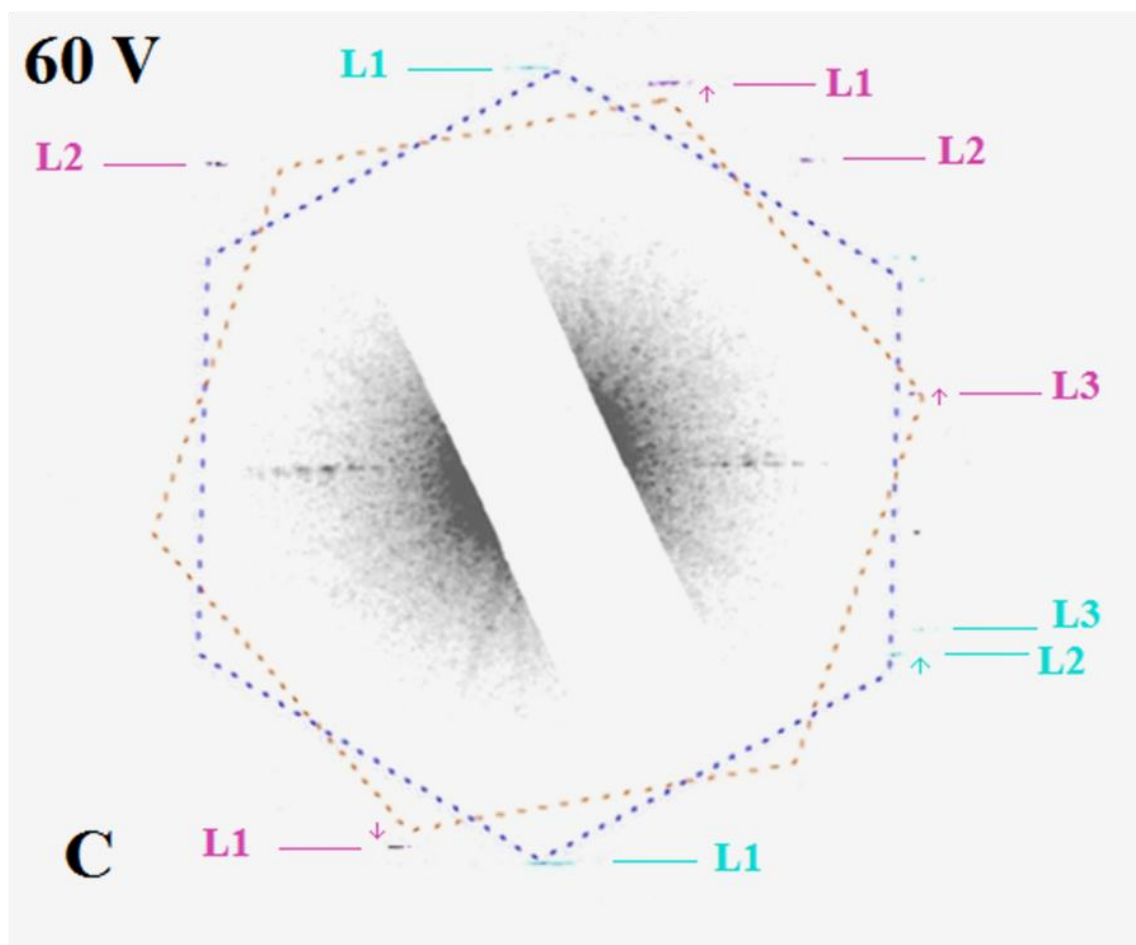
Figure 6.2.1 (continued) (C) Electron diffraction pattern of the DWNT when the paddle is twisted under bias voltage of 60 V. The positions of the diffraction layer lines of the DWNT bearing no torsional strain are represented by the vertices of yellow and blue hexagons while the diffraction layer lines from the twisted DWNT are marked by the pink and green lines. The pink and green arrows clearly show a shift of diffraction layer lines under torisonal strain, which is used to determine the twist angle and handedness of the nanotube.

Fig. 6.3.2(A) and (C) show the paddle actuation of a SWNT torsional device at the deflection of 41 ° via a gate voltage 65 V and the corresponding diffraction pattern, respectively. The diffraction pattern of the un-twisted SWNT is taken in the same way as mentioned above, from which the chiral indices are determined to be (46, 8), Fig. 6.3.2(B). From the shift of the diffraction layer lines, the handedness is determined to be right-handed.

Table 6.1 summarizes the results from experiments on all five torisonal devices. Within its uncertainty, the twist of the outer shells matches the rotation angles of the paddles in devices 1, 3 and 4. For device 2 and 5, they are a bit off each other probably due to the paddle oscillation during the long time exposure. From the results of our experiment, there is no obvious preference observed on the choice of handedness of SWNT and DWNT. DWNTs can be both right-handed, left-handed or mixed. However, the number of our samples is quite small. Further experiments need to be done to prove this argument.
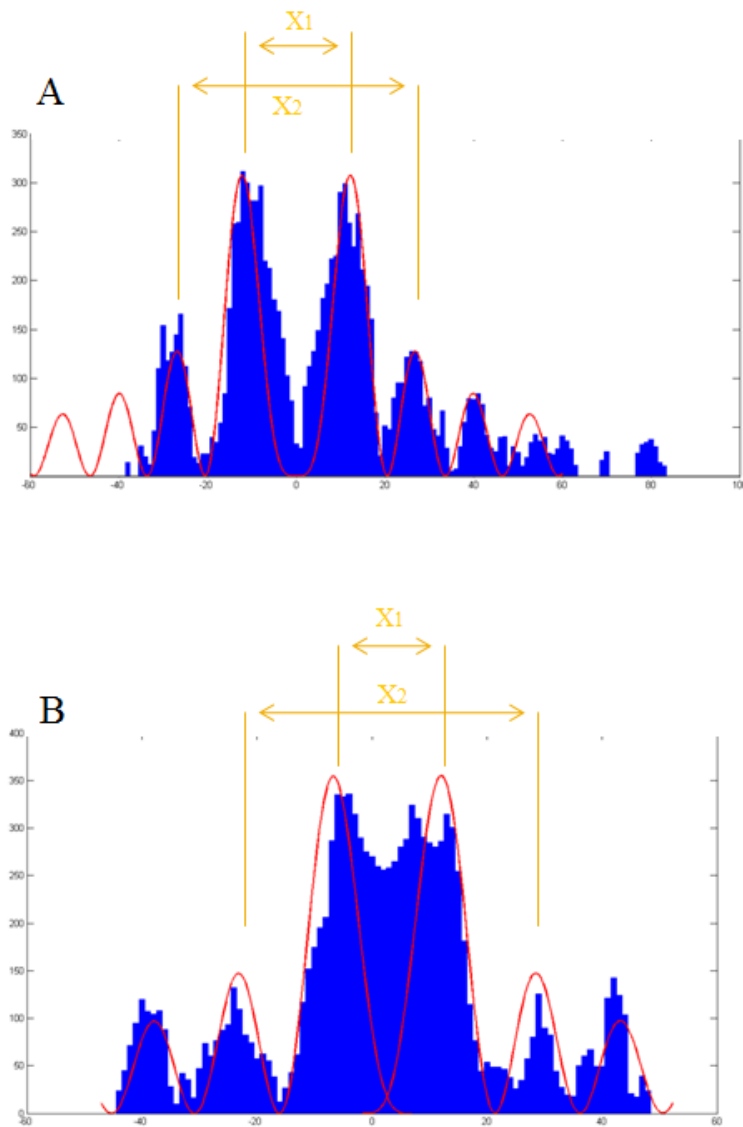
Figure 6.3.1 Intensity profiles of the diffraction layer line L1 from the outer shell of the DWNT shown in Fig. 6.2.1. The red curve is the simulated best-fit Bessel function with order 2 in which X_1 and X_2 are the distances of the first and second order peaks of Bessel function. The index v is derived to be 2 from the ratio of X_1 and X_2 in (A) (details discussed in Chapter 2). (A) Non-twisted DWNT and (B) Twisted DWNT.
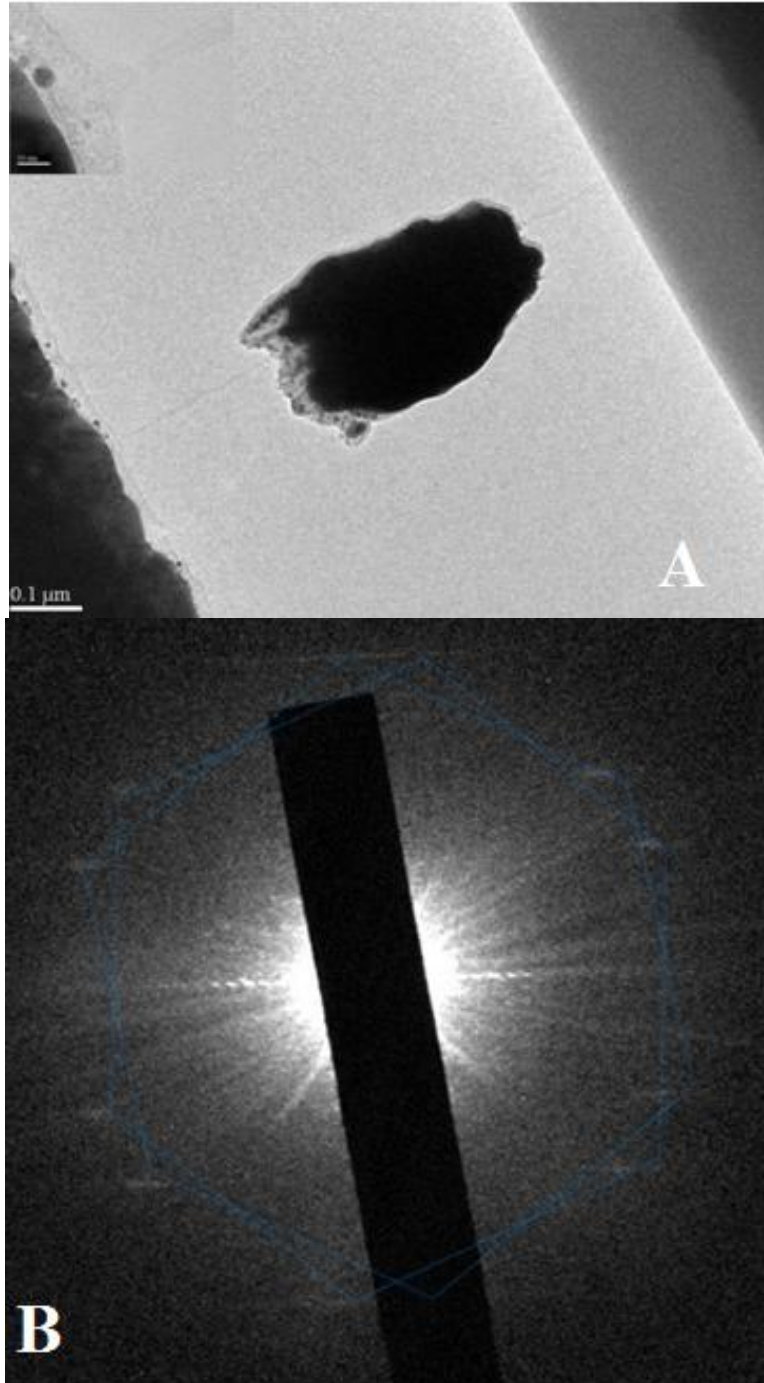
Figure 6.3.2 TEM image and electron diffraction pattern of the suspended SWNT. (A) Low-resolution TEM image of the paddle as it is actuated. It shows deflection of 43° under DC bias 65 V applied to the gate. Scale bar, 100 nm. (B) Diffraction pattern of the SWNT of the non-twisted segments The two hexagons in blue represent the primary reflections of graphene (10), $(\bar{1}0)$ and (11) from the top and bottom part of the nanotube, respectively.
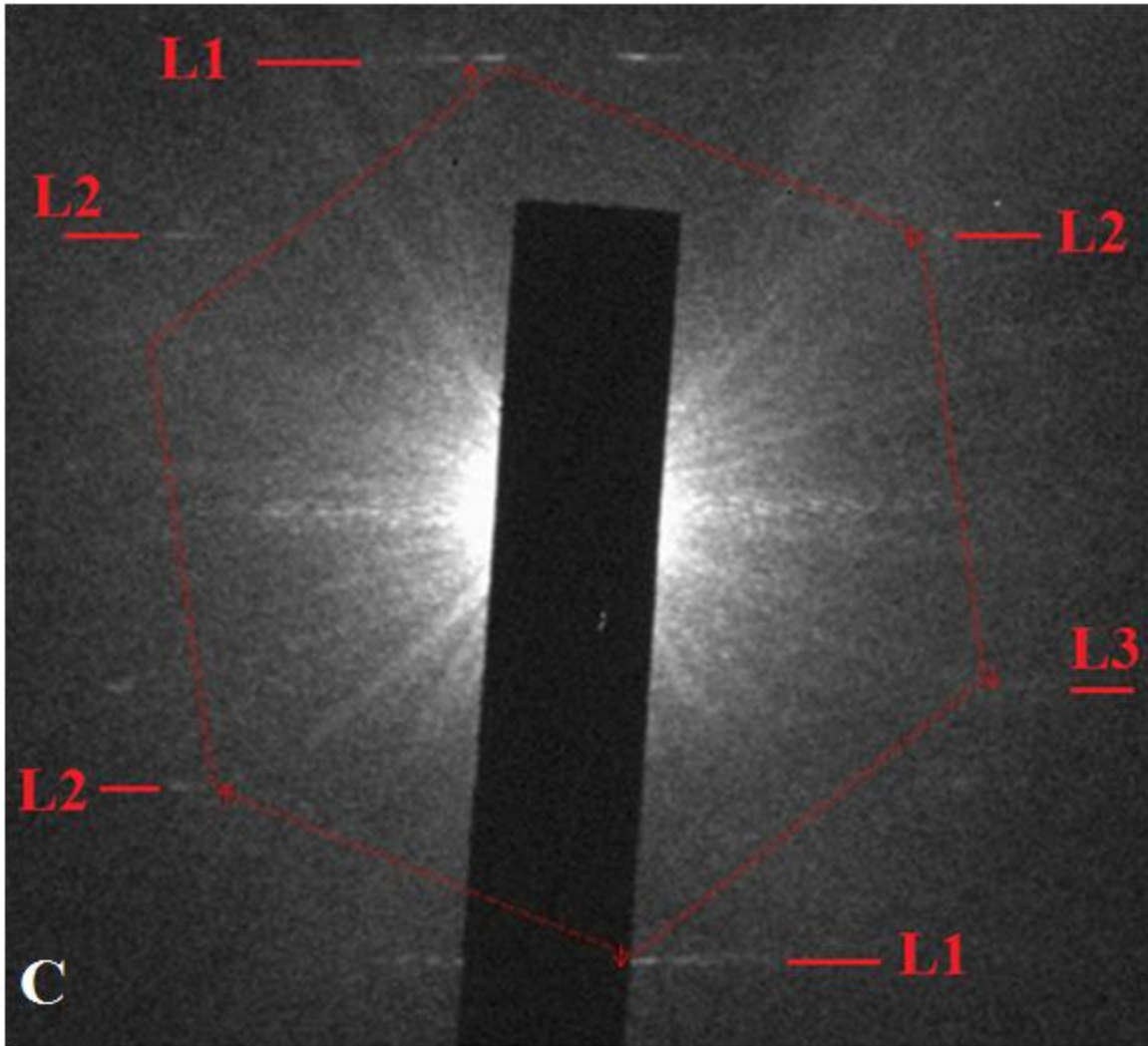
Figure 6.3.2 (continued) (C) Electron diffraction pattern of the SWNT when the paddle is twisted under bias voltage of 65 V. The positions of the diffraction layer lines of the SWNT bearing no torsional strain are represented by the vertices of the red hexagon while the diffraction layer lines from the twisted SWNT are marked by the red lines. The red arrows clearly show the shift of diffraction layer lines under torisonal strain, which is used to determined the handedness of the nanotube.

Dev	Type	shell	Chiral Indices	Voltage (V)	D_1/D_2	$\Delta(D_1/D_2)$	Twisting direction	$\Delta\theta(°)$	$\Delta\theta_{TEM}(°)$	Handed-ness
Dev 1	DWNT	Outer	(56,2)	60	1.981	-0.081	Counter-clockwise	150±12	147	Right-handed
		Inner	(37,18)		1.272	-0.012		24±12		
Dev 2	DWNT	Outter	(5,65)	0	1.926	-0.126	clockwise	76±3.8	66	Left-handed
		Inner	(24,44)		1.243	-0.026		15.2±3.8		
Dev 3	DWNT	Outer	(32,16)	10	1.283	-0.033	Counter-clockwise	39.4±6.8	37	Right-handed
		Inner	(8,29)		1.458	0.008		10.2±6.8		Left-handed
Dev 4	SWNT	N/A	(46,8)	65	1.653	-0.04	Counter-clockwise	41.6±5.2	47	Right-handed
Dev 5	SWNT	N/A	(5,55)	0	1.889	-0.136	Clockwise	60.9±3.2	67	Left-handed

Table 6.1 Summary of electron diffraction analysis on the CNT devices measured in this work. D_1/D_2 is the diffraction layer line spacing ratio. $\Delta(D_1/D_2)$ is the shift of diffraction layer line when the nantobue is twisted. Positive sign indicates the layer lines move toward each other and negative sign indicates the lines move away from each other. L is the length of the nanotube from the paddle to the anchor. Twisting direction refers to the direction looking from the free end of the nanotube. $\Delta\theta/L$ is nanotube twist angle per nanometer. $\Delta\theta$ and $\Delta\theta_{TEM}$ are the twisting angle along the tube calculated from the diffraction patterns and the rotation angle of the paddle measured in the TEM images. Last column is the handedness determined from the shift of the diffraction layer lines. N/A in the table indicates that it is not applicable.

6.4 References

[1]   Hamada, N., Sawada, S. & Oshiyama, A., New One-Dimensional Conductors - Graphitic Microtubules. *Phys. Rev. Lett.* **68**, 1579-1581 (1992).

[2]   Mintmire, J. W., Dunlap, B. I. & White, C. T., Are Fullerene Tubules Metallic. *Phys. Rev. Lett.* **68**, 631-634 (1992).

[3]   Saito, R., Fujita, M., Dresselhaus, G. & Dresselhaus, M. S., Electronic-Structure of Chiral Graphene Tubules. *Appl. Phys. Lett.* **60**, 2204-2206 (1992).

[4]   Krstic, V., Roth, S., Burghard, M., Kern, K. & Rikken, G., Magneto-Chiral Anisotropy in Charge Transport through Single-Walled Carbon Nanotubes. *J. Chem. Phys.* **117**, 11315-11319 (2002).

[5]   Miyamoto, Y., Louie, S. G. & Cohen, M. L., Chiral Conductivities of Nanotubes. *Phys. Rev. Lett.* **76**, 2121-2124 (1996).

[6]   Kibis, O. V., Features of Electron-Phonon Interaction in Nanotubes with Chiral Symmetry Placed in a Magnetic Field. *Phys. Solid State* **43**, 2336-2343 (2001).

[7]   Ivchenko, E. L. & Spivak, B., Chirality Effects in Carbon Nanotubes. *Phys. Rev. B* **66** (2002).

[8]   Jorio, A., Saito, R., Hafner, J. H., Lieber, C. M., Hunter, M., McClure, T., Dresselhaus, G. & Dresselhaus, M. S., Structural (N, M) Determination of Isolated Single-Wall Carbon Nanotubes by Resonant Raman Scattering. *Phys. Rev. Lett.* **86**, 1118-1121 (2001).

[9]   Odom, T. W., Huang, J. L., Kim, P. & Lieber, C. M., Atomic Structure and Electronic Properties of Single-Walled Carbon Nanotubes. *Nature* **391**, 62-64 (1998).

[10]   Wildoer, J. W. G., Venema, L. C., Rinzler, A. G., Smalley, R. E. & Dekker, C., Electronic Structure of Atomically Resolved Carbon Nanotubes. *Nature* **391**, 59-62 (1998).

[11]   Liu, Z., Atomic Structure Determination of Carbon Nanotubes by Electron Diffraction. PhD Thesis, The University of North Carolina at Chapel Hill, (2005).

[12]   Liu, Z. J. & Qin, L.-C., A Practical Approach to Determine the Handedness of Chiral Carbon Nanotubes by Electron Diffraction. *Chem. Phys. Lett.* **405**, 265-269 (2005).

[13]   Meyer, J. C., Paillet, M. & Roth, S., Single-Molecule Torsional Pendulum. *Science* **309**, 1539-1541 (2005).

[14]   Qin, L.-C., Electron Diffraction from Carbon Nanotubes. *Rep. Prog. Phys.* **69**, 2761-2821 (2006).

Chapter 7

Summary and Future Research Direction

7.1 Summary and Implication

The research work in this dissertation presents (i) a foundational study on the atomic structure and inter-shell friction of carbon nanotubes which work as the source to transport NEMS actuation and (ii) a fabrication technique for two nano-electromechanical systems (CNT electrical transport system and CNT torsional system) which provide two versatile platforms for studies of one-dimensional nano-materials such as nanowires or types of nanotubes. The geometry of having a freely suspended carbon nanotube makes the device capable of *in situ* electromechanical manipulation and electrical resistance measurement on a single nanotube in a transmission electron microscope.

The electrical resistance at room temperature and the chiral indices of SWNTs and DWNTs are measured using the CNT electrical transport device. The measured

electrical resistivity shows a general agreement with theoretical estimates based on the nanotube band gap and thermal excitation of electrons at room temperature. The measurements on DWNTs show that the electrical transport only occurs on the outer shell of a DWNT even though the entire nanotube is buried beneath the metal probe. This suggests that the inner shell is insulated to the outer shell probably due to the weak van der Waals interaction. These results will be of importance to the future applications of CNTs as the current carriers in nano-circuit devices and may be expanded to the study on the electrical properties of MWNTs. Since the nanotube is suspended in air between two metal probes for *in situ* TEM imaging, this experiment is free of the error resulted from the structure deformation of a CNT caused by the van der Waals force between the nanotube and the substrate. In contrast, the error becomes severe as the tube diameter increases in the STM measurement where the interaction force is present.

Lattice strain, shear modulus and interlayer friction of a DWNT are measured using the second type of device in which an individual DWNT is employed as a torsional bearing attached with a metal paddle. This is the first direct measurement on the inter-shell coupling under an external torsional stress applied on the outer shell, attributed to the electron diffraction analysis which allows measurements on the structural deformation of both shells. We observed that the inner shell strains in proportion to the outer shell but by a smaller amount (20% or less) with no stiction. The interlayer friction is also inferred from direct measurements of each shell's deformation, van der Waals interactions between shells, and reliable models of lattice strain. Due to the direct measurement on torsional response of inner shell, the shear modulus of inner shell is also precisely derived. These results will be important in the understanding and design of

nano-electromechanical systems that require a fine control of friction and dissipation between nanoscale objects.

Finally, the handedness of both SWNTs and DWNTs are measured experimentally using the CNT torsional device. The shift of the electron diffraction layer lines of a nanotube under a torsional strain reveals the handedness of a nanotube. The knowledge of nanotube handedness will be very important in the understanding of their spin related properties, such as the interactions with photons.

7.2 Future Applications and Directions

Besides the electrical properties, torsional properties and interlayer frictions of CNTs, there is still a large amount of knowledge to be explored from the present CNT devices. Simultaneous measurements on CNT band gaps and chiral indices can be realized in the CNT electrical transport device if a low temperature TEM is employed to cool the device to 17 K in its liquid helium holder. The electrical transport response of a semiconducting CNT to its torsional strain and the CNT chiral structure can be simultaneously measured with the CNT torsional device by a modification on the design of the device circuit. The transition from elastic to plastic deformation of a CNT may also be investigated based on the second type of device by reducing the tube length, *i.e.* resulting in a larger twist angle per nanometer at the same actuation of the metal paddle.

More importantly, the device fabrication technique presented in this thesis provides a versatile platform to achieve simultaneous measurement on structure and property of other one-dimensional or two-dimensional nano-materials such as nanowires or nanosheets. As long as the nano-material can be individually dispersed on the silicon

based substrate, it can be made into both types of devices using the fabrication technique. This will be very useful for revealing the causality between material structure and its properties. The applications of nano-materials for nano-scale devices can also be benefited from these device geometries.

Last but not least, the suspended CNT device provides a possible way to fabricate three-dimensional nano-devices. With the device part fully suspended in air, it is possible to fabricate other devices on top or beneath it. While huge challenges exist, this technique can be a starting point for trials.

The work presented in this thesis on the CNT nano-electromechanical devices capable of TEM imaging can be viewed as a starting point to the future investigation techniques for nano-materials.

Appendix I

Chemical Vapor Deposition for CNT Synthesis

The following section includes step-by-step instructions for synthesizing SWNTs and DWNTs on silicon wafer coated with a 200 nm silicon dioxide layer for device fabrication. All the parameters have been shown highly sensitive to the specific apparatuses being used; different systems will result in significant variations in the parameters presented here. This recipe is based on the recipe provided by Dr. Jie Liu's group of Duke University.

DWNT Synthesis

1) Solvent clean and UV/Plasma clean substrates.

2) Use $FeSi_2$ solution in hexane (0.12mg $FeSi_2$ powders dissolved in 40 ml ethanol and diluted to 1/10000), disperse solution over the entire surface and let it evaporate very slowly.

3) Place samples into the tube furnace.

4) With air (no gas), anneal the sample at 900 ^{o}C for 10 min (not including heating time).

5) Hook up gas inlet and exhaust.

6) Purge the system with Argon at the flow rate of 500 sccm for 15 min at 900 ^{o}C

7) Raise the temperature to 922 ^{o}C.

8) Turn off Argon, turn on Hydrogen (500 sccm), Methane (1500 sccm) and Ethylene (30 sccm) for 10 min growth.

9) Turn off the Methane and Ethylene.

10) Turn off the furnace and leave Hydrogen on for purge purpose.

11) Let the system cool down to 200 ^{o}C.

12) Turn off Hydrogen and take out the sample.

SWNT Synthesis

1) Solvent clean and UV/Plasma clean substrates.

2) Use $Fe(NO_3)_3$ as the catalyst (5 mg $Fe(NO_3)_3$ dissolved in 50 ml IPA and diluted to 1/10000) and disperse solution over the entire surface.

3) Place samples into the tube furnace.

4) Hook up gas inlet and exhaust.

5) Purge the system with Argon at the flow rate of 500 sccm for 15 min.

6) Raise the temperature to 922 ^{o}C.

7) Turn off Argon, turn on Hydrogen (500 sccm), Methane (1500 sccm) and Ethylene (30 sccm) for 10 min growth.

8) Turn off the Methane and Ethylene.

9) Turn off the furnace and leave Hydrogen on for purge purpose.

10) Let the system to cool down to 200 ^{o}C

11) Turn off Hydrogen and take out the sample.

Appendix II

Instructions of Carbon Nanotube Based Torsional Device Fabrication

The following steps include a complete fabrication procedure from a bare wafer to a suspended structure which is ready for *in situ* TEM imaging and electron diffraction analysis. The instruction of electron beam lithography, BHF etching and supercritical point drying are mostly based on Dr. Adam Hall's device instruction in his PhD dissertation. They are rewritten here for the continuity of the instruction. The instruction is written for the following instruments:

- Kasper UV mask aligner

- Keithley 2400 sourcemeter

- Advanced Vacuum Vision 310 Plasma Enhanced Chemical Vapor Deposition System

- Nano Pattern Generation System (NPGS) Software (J. C. Nabity)

- DesignCAD

- Balzers Union CPD 020 critical point drying apparatus

- Samco RIE System, Model RIE-1C

- FEI Helios 600 nanolab Dual Beam Focus Ion Beam System

I.   Photolithography for Wafer Back-Etching

   1) Clean wafer and cut wafer.

       1. Dip the wafer into piranha solution for 10 min, rinse with solvents and

       nitrogen dry.

       2. Cut the wafer into 33 mm × 9 mm slices.

   2) Clean room preparation

       1. Turn on and the vacuum pump of the photo mask aligner.

       2. Turn on the Lamp Start on the lamp power box and turn on the mask

       aligner.

       3. Turn on the hot plate and set temperature to 115 ^{o}C .

   3) Apply resist

       1. Set spin coater to 3000 rpm, 60 seconds and acceleration 15.

       2. Place one wafer slice (polished side down) onto the spin coater chuck

         (with vacuum function on) and cover the whole surface with photoresist

         S1813.

       3. Start spin-coat and move the wafer to hot plate once finished for 1

         minute soft bake.

       4. Repeat for all the samples.

   4) Exposure

       1. Press MASK LOAD.

       2. Unload the mask holder and turn off the vacuum by clicking ENTER.

       3. Place the mask onto the mask holder and turn on the vacuum by clicking

ENTER.

4. Press LOAD and load the wafer.

5. Align the wafer to the photo mask by the x and y position knobs located

on the left and right sides of the sample stage. Make sure the six 0.8 mm

$\times$ 0.8 mm squares are right on the center of the wafer.

6. Set hard contact mode, gap=50 μm and exposure time=10 seconds.

7. Expose the sample by clicking EXPOSURE.

5) Develop

1. After exposure, take off the sample and dip it into MF 319 Photoresist

Developer for 40 seconds developing.

2. Rinse the sample with water and nitrogen dry.

3. Check the photolithography patterns in the optical microscope in case

the sample is over or under developed.

II. Remove Backside Nitride Film by Reactive Ion Etching (RIE) System

1) RIE preparation

1. Turn on the Nitrogen and cooling water.

2. Turn on O_2 and C_3F_8.

3. Turn on the RIE system and click RESET to vent the chamber.

4. Turn off the valves of O_2 and C_3F_8 on the front panel of RIE.

2) Sample etching

1. Lift the chamber lid and put a test wafer onto the center of the

sample stage.

2. Click START and turn on GV1 and GV2.

3. Set the flow rate reading of C_3F_8 to 4.8 by turning the valve counter-

   clockwise once the chamber pressure reaches 12 mtorr.

4. Slowly turn the O_2 valve counter-clockwise until the champer pressure

   increased by 10 %.

5. Set the RF power to 400 watts and turn on the plasma.

6. Use the phase and load dial to adjust the reflected power as

   close to 0 or 1 watt as possible.

7. Set the etching to be 7 minutes.

8. Click RESET to vent the chamber once the etching is done.

9. Take out the test sample and check it in the optical microscope (silicon

   nitride film is removed if the grey bare silicon can be seen).

10. Repeat all the steps for formal samples.

3) Remove the photoresist on the samples by sonication in acetone for 10

   minutes.

III.   Backside Silicon Etching by KOH

1) Preparation before etching

   1. Pour 150 ml 45 % potassium hydroxide solution into a 500 ml beaker.

   2. Pour 300 ml DI water into the beaker and mix the solution thoroughly.

   3. Place the beaker on the hot plate, insert the thermal sensor into the

      solution and set the temperature of hot plate to 70 ^{o}C. (15 % KOH etches

      (100) silicon at a rate of 1 μm per min at 70 ^{o}C.

2) Etching process

   1. Place all the samples into the beaker with unpolished side facing up.

2. Monitor the etching reaction (hydrogen bulbs will coming out on the bare silicon surface). If there are not bulbs, it means the nitride film is not etched through.

3. Check the etch depth under the optical microscope every 20 minutes after 4 Hours etch. The etch depth is the height of the sample stage when the sample top surface is in focus subtracted by that of the stage when the etched surface is in focus.

5. Stopping etching when the etch depth reaches 400 μm .

6. Rinse the sample with water followed by solvent clean.

IV.   Plasma Enhanced Vapor Deposition

1) Pre-deposition preparation

1. Select "Start Batch".

2. Choose "RF etchback" recipe from the pull-down menu.

3. Click "Start".

4. After 45 minutes etchback, Select "Start Batch".

5. Choose "Silicon Nitride" recipe from the pull-down menu.

6. Set process time to 5 minutes.

7. Click "Start".

2) Film Deposition

1. Click "Vent".

2. Click "Open" when the "Open" option is shown on the screen.

3. Load the sample onto the center of the sample stage with polished side facing up.

4. Click "Close".

5. Click "Pump".

6. Click "Start Batch" when the pressure less than 3.0×10^{-3} Pa.

7. Select "Silicon Nitride" recipe from the pull-down menu and set time to 3 minutes (deposition rate 7 nm/min).

8. Once the deposition is done, repeat step 1 to 5 to take out the sample.

9. Repeat the step 1-4 of pre-deposition preparation for the etchback.

10. Click "Start Batch", select "Oxide" recipe from the pull-down menu and set time to 5 minutes.

11. Repeat step 1-5 to load the samples with polished side facing up.

12. Select "Start Batch", choose "Oxide" recipe from the pull-down menu and set time to be 8 minutes (deposition rate 27 nm/min).

13. Repeat step 1-5 to take out the samples.

V.   CNT Synthesis on the Polished Sides of the Wafers Followed by the steps in Appendix I.

VI.   Photolithography on Polished Side

   1) Clean room preparation

      1. Turn on the vacuum pump of the photo mask aligner.

      2. Turn on the Lamp Start on the lamp power box and turn on the mask aligner.

      3. Turn on the hot plate and set temperature to 115 $^{\mathrm{o}}$C .

   3) Apply resist

      1. Set spin coater to 3000 rpm, 60 seconds and acceleration 15.

2. Place one wafer slice (unpolished side down) onto the spin coater chuck

(with vacuum function on) and cover the whole surface with photoresist

S1813.

3. Start spin-coat and move the wafer to hot plate once finished for 1

minute soft bake.

4. Repeat for all the samples.

4) Exposure

1. Press MASK LOAD.

2. Unload the mask holder and turn off the vacuum by clicking ENTER.

3. Place the mask onto the mask holder and turn on the vacuum by clicking

ENTER.

4. Place the double side alignment wafer chunk into the chunk holder.

5. Turn on the backside microscope by clicking BSA.

6. Align the microscope position until the desired patterns on the mask can

be seen from the right and left microscope and are located in the center of

the screen.

7. Click GRAB to record pattern position image.

8. Press LOAD and load the wafer.

9. Align the wafer to the photo mask by the x and y position knobs located

on the left and right sides of the sample stage. Make sure the two patterns

on the image right fall on the two 0.4 mm $\times$ 0.4 mm squares etched on

the backside of the wafer, respectively.

10. Set hard contact mode, gap=50 μm and exposure time=10 seconds.

11. Expose the sample by clicking EXPOSURE.

5) Develop

   1. After exposure, take off the sample and dip it into MF 319 Photoresist
Developer for 40 seconds developing.

   2. Rinse the sample with water and nitrogen dry.

   3. Check the photolithography patterns in the optical microscope in case the
sample is over or under developed.

6) Metallization

   1. Deposit 10 nm Cr or Ti and 50 nm Au with thermal or e-beam evaporator.

   2. Thickness is important: thickness of photolithgraphy should be less
than that of future ebeam lithography for superior contact to leads.

   3. Soak in acetone for at least 40 minutes and sonicate for 1 minute.

   4. Solvent clean the samples and check them in the optical microscope.

VII.   Fiducials

1) Cleave wafer into individual playgrounds.

   1. Place wafer, pattern up, on contact paper.

   2. Using a glass slide (separated from wafer by another sheet of contact
paper) as a template, make one small (~0.25") scribe at one edge.

   3. Flip sample and place on padded mat, covered by new contact paper
and roll small metal rod over it (so the rod is parallel with the scribe
and motion is perpendicular), pressing until sample breaks.

   4. Spray with isopropanol (IPA), Nitrogen dry.

2) Tube burning

1. Set Keithley for 10-20V and test the connection between each adjacent

   lead (1-2, 2-3….7-8,8-1).

2. When there is current greater than a few tens of pA, increase the voltage

   until the current drop to couple pAs.

3. Stop the current once connection fails.

4. Also check connection between all leads and backgate to ensure no

   leakage current- if so, repeat for those connections.

5. Rinse with IPA and Nitrogen dry.

3) Initial Imaging

1. Image samples (capture):

   - 1 kV, 20uA

   - upper detector (column adjust)

   - Cond. Lens 1= 1

   - 1.3kX magnification

2. Transfer images to NPGS-equipped computer.

4) CAD

1. Choose File -> Image ->Load image file and select high resolution image.

2. Open zif_coarsealign file.

On high resolution image:

3. Zoom on scale bar, hit "u", set crosshairs at ends and input length scale.

4. Hit "v", draw vectors to symmetrical areas of sample (fine alignment marks),

   zoom on intersection, go to Point->Origin and click on intersection point,

   and delete vector.

5. Copy appropriate fiducials and place them appropriately.

6. Copy coarse align windows onto image and align.

7. Delete SEM background image.

8. Delete devices and fids and NPGS-> Save what remains as *_aln.DC2.

9. Hit Edit -> Undo.

10. Delete alignment windows and NPGS-> Save what remains as *_dev.DC2.

5) Run file

1. In NPGS menu, go to Project -> Create New Project, add folder name where files were stored.

2. In "run file editor", set entities to 2, change first to alignment and input *-aln.DC2, input *_dev.DC2 for second.

FOR ALIGNMENT:

3. magnification = 800

4. measured beam current = 12

5 ls=2000

FOR PATTERN:

6. magnification = 800

7. ls=300

8. measured beam current = 12

9. dose= 1.2

6) Bylayer PMMA

1. Set spin coater to 5000 rpm and 40 seconds, set hotplate with internal readout to 180 ^{o}C and set a timer to 2 min.

2. Using dropper, deposit 4% PMMA (mwt = 350k) onto the sample until

entire surface is covered but not dripping off edges, start spinning and (once

finished) move to hotplate.

3. Remove after 2 min.

4. Set spin coat to 4000 rpm and 40 seconds, set tube furnace to 180 $^{\circ}$C.

5. Stick sample, backgate down, to spin coater chuck with two sided tape or

carbon tape.

6. Using dropper, deposit 4% PMMA (mwt = 996k) onto sample until entire

surface is covered but not dripping off edges, start spinning.

7. Bake in tube furnace for 1.5-2 hrs.

7) Exposure

1. Put sample on Faraday cup stage and set SEM for 30 kV and 5 µA and go to

faraday cup.

2. Set focus and stigma on edge of cup.

3. Set current in high mag mode (above 20k x) to appropriate current

(check run file "measured current").

4. Move to playground and refocus on debris or metal edge.

5. Set magnification (check run file "magnification"), switch control over to

NPGS and process run file.

6. Switch control back to SEM; repeat for all samples.

8) Develop

1. Put small amount of PMMA developer (Methyl Isobutyl Ketone (MIBK):

IPA, 1:3) in 10 mL beaker and set timer for 1:10 (make sure it's enough to

submerge the sample area).

2. Develop each sample, rinse with DI water and Nitrogen dry.

3. Check with optical microscope.

9) Metallize

1. Deposit ~10 nm Cr or Ti and ~80nm Au with thermal or e-beam evaporator.

2. THICKNESS SHOULD BE GREATER THAN THICKNESS OF

PHOTOLITHOGRAPHY.

10) Liftoff

1. Soak in acetone for at least 15 min.

2. Use syringe/sonicator to remove off excess metal.

3. Rinse with IPA, Nitrogen dry.

4. Check with optical microscope.

VIII. Paddles and Anchors

1) Image samples.

1. Image samples (capture):

- 1 kV, 20uA

- upper detector (column adjust)

- 1.3kX magnification

- transfer images to NPGS-equipped computer

- store samples in acetone for cleanliness (rinse with IPA and Nitrogen dry

before further use)

2) CAD (for each)

1. Choose File -> Image ->Load image file and select high resolution image.

2. Open zif_finealign file and paddle farm file.

On high resolution image:

3. Zoom on scale bar, hit "u", set crosshairs at ends and input length scale.

4. Hit "v", draw vectors to symmetrical areas of sample (fine alignment marks), zoom on intersection, go to Point->Origin and click on intersection point, and delete vector.

5. Copy appropriate anchors and paddles (for CNT, generally no longer than 600nm) and place them appropriately.

6. Make electrical leads (make no less than 2μm thick), starting from anchor and going to lead.

7. Copy fine align windows onto image and align.

8. Delete SEM background image.

9. Delete devices and NPGS-> Save what remains as *_aln.DC2.

10. Hit Edit -> Undo.

11. Delete alignment windows and NPGS-> Save what remains as *_dev.DC2.

3) Run file

1. In NPGS menu, go to Project -> Create New Project, add folder name where files were stored.

2. In "run file editor", set entities to 2, change first to alignment and input *-aln.DC2, input *_dev.DC2 for second.

FOR ALIGNMENT:

3. magnification = 900

4. measured beam current = 12

5. layers 11 and 15 = Start New Set

6. ls(7-10)=2000

7. ls(11-14)=456

8. ls(15-18)=192

FOR PATTERN:

9. magnification = 900

10. ls=300

11. measured beam current = 12

12. dose= 0.9 (for very small separation distances, values as low as 0.6 can be
   used)

4) Bylayer PMMA

   1. Set spin coater to 5000 rpm and 40 seconds, set hotplate with internal
      readout to 180 ^{o}C and set a timer to 2 min.

   2. Using dropper, deposit 4% PMMA (mwt = 350k) onto sample until entire
      surface is covered but not dripping off edges, start spinning and (once
      finished) move to hotplate.

   3. Remove after 2 min.

   4. Set spin coater to 4000 rpm and 40 seconds, set tube furnace to 180 C.

   5. Stick sample, backgate down, to spin coater chuck with two sided tape or
      carbon tape.

   6. Using dropper, deposit 4% PMMA (mwt = 996k) onto sample until entire
      surface is covered but not dripping off edges, start spinning.

   7. Bake in tube furnace for 1.5-2 hrs.

5) Exposure

   1. Put sample on Faraday cup stage and set SEM for 30 kV and 5 μA and go to
      faraday cup.

2. Set focus and stigma on edge of cup.

3. Set current in high mag mode (above 20k x) to appropriate current

(check run file "measured current").

4. Move to playground and refocus on debris or metal edge.

5. Set magnification (check run file "magnification"), switch control over to

NPGS and process run file.

6. Switch control back to SEM; repeat for all samples.

6) Develop

1. Put small amount of PMMA developer (Methyl Isobutyl Ketone(MIBK):IPA,

1:3) in 10 mL beaker and set timer for 1:10 (make sure it's enough to

submerge the sample area).

2. Develop each sample, rinse with DI water and Nitrogen dry.

3. Check with optical microscope.

7) Metallize

1. Deposit ~10 nm Cr or Ti and ~80nm Au with thermal or e-beam evaporator.

2. THICKNESS SHOULD BE GREATER THAN THICKNESS OF

PHOTOLITH.

8) Liftoff

1. Soak in acetone for at least 15 min.

2. Use syringe/sonicator to remove off excess metal.

3. Rinse with IPA, Nitrogen dry.

4. Check with optical microscope.

IX HNA Backside Etching

1. Turn on hot plate and set temperature to 60 ^{o}C.

2. Place a large and clean wafer on the hot plate.

3. Cut a 5 mm×5 mm copper tape and attach it to the sample on the position .
about 0.5 mm higher than the playground. It works as a stop of HNA.
Otherwise HNA will etch the playground along the sample edges during the
backside etching.

4. Place samples on the large wafer with unpolished side facing up.

5. Place the a drop of HNA into the etched windows on the backside of the
sample to etch the silicon.

6. Let the HNA evaporate and repeat step 5 until all the left silicon is etched
away.

7. Rinse samples with water and followed by solvent clean.

X. FIB Fontside and Backside Etching

1) Frontside etching

1. Click Vent.

2. Stick the sample onto the FIB sample stage with double side copper tape.

3. Click Pump.

4. Turn on electron and ion beam by clicking Beam On on electron and ion beam
windows.

5. In the SEM mode, move the sample so that the left upper corner of the
playground is in the center of the screen at 4k magnification.

6. Tilt the sample to 7 ^{o} and move the sample feature back to the center of the
screen if it moves away during the tilting.

7. Tilt the sample back to 0 ^{o} and bring the feature back to the screen center if it

moves away.

8. Repeat step 7-8 until the shift is less than 10 μm from 0 ^{o} to 7 ^{o}.

9. Tilt the sample to 52 ^{o} and move the sample feature back to the center of the
   screen if it moves away during the tilting.

10. Tilt the sample back to 0° and bring the feature back to the screen center if it
    moves away.

11. Repeat step 9-10 until the shift is less than 1 μm from 0 ^{o} to 52 ^{o}.

12. Switch to ion beam mode and align the beam until the same feature is at the
    center of the screen.

13. Select Rectangle from the Pattern menu and draw a 13 μm × 13 μm rectangle in
    the blank area (no metal leads) and set the etch depth to 550 nm. (the etched
    window will be used for the TEM alignment)

14. Click Etching button.

15. Tilt the sample to 0 ^{o} and switch to SEM mode.

16. Move the playground center to the screen center. Repeat step 6-12.

17. Select Rectangle from the Pattern menu and draw a cross mark (3 μm × 0.7 nm)
    in the blank area (no metal leads) and set the etch depth to 550 nm. The cross
    mark will be used as alignment mark in the backside FIB etching.

18. Click Etching button.

19. Tilt the sample to 0 ^{o}, switch to SEM mode and scan the playground at the
    magnification of 1.3 k.

20. Record all the coordinates of the devices relative to the cross mark.

21. Click Vent and take out the sample.

2) Backside FIB etching

1. Flip the sample over and attach the sample to the sample stage. (Make sure the playground window cannot touch anything otherwise it will break.

2. Click Pump.

3. Turn on electron and ion beam by clicking Beam On on electron and ion beam windows.

4. In the SEM mode, move the sample so that the cross mark is in the center of the screen at 4k magnification.

5. Tilt the sample to 7 ^{o} and move the cross mark back to the center of the screen if it moves away during the tilting.

6. Tilt the sample back to 0 ^{o} and bring the cross mark back to the screen center if it moves away.

7. Repeat step 5-6 until the shift is less than 10 μm from 0 ^{o} to 7 ^{o}.

8. Tilt the sample to 52 ^{o} and move the cross mark back to the center of the screen if it moves away during the tilting.

9. Tilt the sample back to 0° and bring the cross back to the screen center if it moves away.

10. Repeat step 8-9 until the shift is less than 1 μm from 0 ^{o} to 52 ^{o}.

11. Switch to ion beam mode and tilt the beam until the same feature is in the center of the screen.

12. Locate the device positions with respect to the cross mark, draw a 1.4 μm × 1.9 μm rectangle at the position of every device and set the etch depth to 350 nm. This will leave a 150 nm silicon dioxide film to support the device.

13. Click Etching button.

14. Tilt the sample to 0 ^{o} and switch to SEM mode.

15. Click Vent and take out the samples.

16. Check the sample in the optical microscope if the etched windows are right

below the devices.

XI. BHF Etching

1) Image samples

1. image samples (capture):

- 1 kV, 20uA

- upper detector (column adjust)

- 1.3kX magnification

2. Transfer images to NPGS-equipped computer.

3. Store samples in acetone for cleanliness (rinse with IPA and Nitrogen dry before

further use).

2) CAD (for each)

1. Choose File -> Image ->Load image file and select high resolution image.

2. Open zif_finealign file and paddle farm file.

On high resolution image:

3. Zoom on scale bar, hit "u", set crosshairs at ends and input length scale.

4. Hit "v", draw vectors to symmetrical areas of sample (fine alignment marks),

zoom on intersection, go to Point->Origin and click on intersection point, and

delete vector.

5. Draw line DIRECTLY over paddle (line width = 0.2).

6. Copy fine align windows onto image and align.

7. Delete SEM background image.

8. Delete devices and NPGS-> Save what remains as *_aln.DC2.

9. Hit Edit -> Undo.

10. Delete alignment windows and NPGS-> Save what remains as *_dev.DC2

3) Run file

1. In NPGS menu, go to Project -> Create New Project, add folder name where
   files were stored.

2. In "run file editor", set entities to 2, change first to alignment and input *-
   aln.DC2, input *_dev.DC2 for second.

FOR ALIGNMENT:

3. magnification = 900

4. measured beam current = 12

5. layers 11 and 15 = Start New Set

6. ls(7-10)=2000

7. ls(11-14)=456

8. ls(15-18)=192

FOR PATTERN:

9. magnification = 900

10. ls=300

11. measured beam current = 12

12. dose= 0.9

4) PMMA coating

1. Set spin coater to 4000 rpm and 40 seconds, set tube furnace to 180 ^{o}C.

2. Stick sample, backgate down, to spin coater chuck with two sided tape or carbon tape.

3. Using dropper, deposit 4% PMMA (mwt = 996k) onto sample until entire surface is covered but not dripping off edges, start spinning.

4. Bake in tube furnace for 1.5-2 hrs.

5) Exposure (for each)

1. Put sample on Faraday cup stage and set SEM for 30 kV and 5 µA and go to faraday cup.

2. Set focus and stigma on edge of cup.

3. Set current in high mag mode (above 20k x) to appropriate current. (check run file "measured current")

4. Move to playground and refocus on debris or metal edge.

5. Set magnification (check run file "magnification"), switch control over to NPGS and process run file.

6. Switch control back to SEM; repeat for all samples.

6) Develop

1. Put small amount of PMMA developer (MIBK:IPA, 1:3) in 10 mL beaker and set timer for 1:10 (make sure it's enough to submerge the sample area).

2. Develop each sample, rinse with DI water and Nitrogen dry.

3. Check with optical microscope (may not be able to see).

7) Sample etching

1. Pour a small amount of BHF solution into a small Teflon beaker and prepare a

timer.

   2. Use a plastic syringe, place drops of BHF onto the sample (DO NOT spill over

    edge- will eat away backgate).

8) Etch stop

   1. Prepare a large beaker of DI water and a storage jar of ethanol.

   2. Remove working sample at desired etch depth.

   3. Keep in mind that etch rate may be varied by the presence of materials (cnt, etc)

    or by contamination from previous imaging- judge accordingly.

   4. Dip sample directly into DI water (do *not* let the liquid leave the surface of the

    sample; keep wet).

   *IF USING ETCH WINDOWS: soak in acetone for AT LEAST 40 min. to remove

    PMMA.

   5. Remove and place in the jar of ethanol for storage until critical point drying .

XIII. Critical Point Drying

   1. Make sure all three valves on critical point dryer are firmly closed.

   2. Remove lid and pour ethanol in drying chamber until port hole is high enough to

    cover samples (judge by eye).

   3. Place small glass ring (flow protector) into chamber (and off to right), and inside

    ring put one of the curved-bottom ceramic pieces (broken tube furnace boat).

   4. Remove sample from jar and put directly into chamber ethanol (again, do not

    break Surface tension on sample) and place FACE DOWN in curved piece. If all

    samples don't fit, ceramic pieces are stackable; close lid.

   5. Open both tanks of CO2, push "MAINS"

   6. Push "TEMPERATURE" and set goal temperature to 15, let chamber cool.

7. Once cooled, open GAS IN knob (on left of machine) slightly and let port hole fill entirely.

8. If it is filled to quickly, the turbulence may damage your samples.

9. Close GAS IN, open GAS OUT (right side front) several turns and then slowly open METERING VALVE (right side rear) to let liquid drain (do *not* let liquid level drop to the sample).

10. Close both METERING VALVE and GAS OUT and repeat filling process (from "open GAS IN", above) 4 or 5 times, until liquid is completely clear and all ethanol is replaced.

11. Make sure all valves are closed and close CO2tanks.

12. Set goal temperature to 45; transition will occur as pressure and temperature rise- watch port hole for it.

13. After transition, open METERING VALVE several turns and open GAS OUT very slightly (should only have started to hear the gas coming out).

14. Let pressure reduce; DO NOT let condensation occur (caused by letting out gas too fast).